

Gas fractionation and CO₂-dynamics
in natural high-CO₂-systems

Dissertation

zur

Erlangung des akademischen Grades

doctor rerum naturalium (Dr. rer. nat.)

der Mathematisch-Naturwissenschaftlichen Fakultät

der Universität Rostock

vorgelegt von

Stine Beilfuhs, geb. Thomas, am 03.01.1987 in Rostock

Rostock, 10.06.2021

Gutacher:

Prof. Dr. Gregor Rehder, Universität Rostock, Leibniz-
Institut für Ostseeforschung Warnemünde

Prof. Dr. Arne Körtzinger, Universität Kiel, GEOMAR
Helmholtz-Zentrum für Ozeanforschung Kiel

Jahr der Einreichung: 2021

Jahr der Verteidigung: 2021

Summary

The Okinawa Trough in the western Pacific Ocean hosts several active hydrothermal fields, which emit carbon dioxide-rich hot fluids as well as low-temperature gas bubbles and droplets (in the following referred to as ‘condensed phase’). The present study contributes to our understanding of these fluids and condensed phases through investigations at two of these natural gas release areas (Yonaguni Knoll IV and Hatoma Knoll). The impact of the hydrothermal input on the water column was inferred from several geochemical parameters (pH, redox potential Eh, total carbon dioxide C_T , helium concentration ^3He and ^4He). Additionally, the gas composition and isotopy (^3He , $\delta^{13}\text{C}$) of four condensed phases from Hatoma Knoll were determined.

The water columns of both research areas show vent-induced characteristic, but similar geochemical signatures. The data suggest that the observed pH reduction of the water column is mainly caused by the addition of carbon dioxide. The flux of CO_2 into the water column is dominated by hot hydrothermal CO_2 -rich vents, whereas the influence of the significantly lower release quantities of the condensed phases is very likely restricted to the lowermost 10 m of the water column.

The condensed phases differ considerably regarding their $\text{CO}_2/^3\text{He}$ ratio. The gas composition of the condensed phases varies widely, although the vents are located close together within an area of about 0.01 km^2 . Not all of them show the expected CO_2 dominance based on earlier scientific campaigns, but partly high concentration of methane. However, homogenous isotope data of the samples indicate a common origin of the gases. Prevailing pressure and temperature conditions induce diverse phase transformation and thus fractionation below and above the seafloor, hence the condensed phases are emitted as liquid or gas and partly form a gas hydrate skin due to contact with cold (pore) water. A physicochemical treatment of phase transformations and resulting fractionation processes is performed here, using a commercially available thermodynamics software including a hydrate-formation module. Changes in phase behavior are mainly traced back to the CO_2/CH_4 ratio, as well as the influence of nitrogen and hydrogen sulfide.

Zusammenfassung

Im Okinawa Trog, westlicher Pazifischer Ozean, befinden sich mehrere aktive Hydrothermalfelder, die kohlendioxidreiche heiße Fluide sowie kalte Gasblasen und Tropfen („kondensierte Phasen“) freisetzen. Diese Arbeit trägt zu unserem Verständnis dieser Fluide und der kondensierten Phasen bei durch die Untersuchung an zwei dieser natürlichen Gasaustrittsgebiete (Yonaguni Knoll IV und Hatoma Knoll). Der Einfluss von hydrothermalen Einträgen auf die Wassersäule wurde anhand verschiedener geochemischer Parameter (pH, Redoxpotential Eh, Gesamt-CO₂- C_T und Heliumgehalt ³He, ⁴He) untersucht. Zusätzlich wurde die Gaszusammensetzung und Isotopie (³He, δ¹³C) von vier kondensierten Phasen vom Hatoma Knoll bestimmt.

Die Wassersäulen der beiden Untersuchungsgebiete zeigen eine charakteristische, aber ähnliche geochemische Signatur. Die Daten lassen vermuten, dass die beobachtete pH-Abnahme der Wassersäule eine Folge der CO₂-Freisetzung ist. Der CO₂-Fluss in die Wassersäule wird durch die heißen hydrothermalen CO₂-reichen Quellen dominiert, wohingegen sich der Einfluss der freigesetzten kondensierten Phasen mit ihren wesentlich geringeren Freisetzungsmengen sehr wahrscheinlich hauptsächlich auf den unteren Teil der Wassersäule beschränkt.

Die kondensierten Phasen unterscheiden sich wesentlich in Bezug auf ihr CO₂/³He-Verhältnis. Die Gaszusammensetzung der einzelnen kondensierten Phasen variiert stark, obwohl die einzelnen Quellen innerhalb einer kleinen Fläche von etwa 0,01 km² liegen. Nicht alle Proben zeigen die erwartete CO₂-Dominanz früherer Untersuchungen, sondern auch hohe Konzentration an Methan. Die homogenen Isotopendaten der verschiedenen Proben lassen einen gemeinsamen Ursprung der Gase vermuten. Bei den vorherrschenden Temperatur- und Druckbedingungen finden unter- und oberhalb des Meeresbodens verschiedene Phasenänderungen und damit Fraktionierungen statt, sodass die kondensierten Phasen flüssig oder gasförmig freigesetzt werden und beim Kontakt mit kaltem (Poren-)Wasser Gashydratschichten ausbilden können. Eine physikochemische Betrachtung der Phasenänderungs- und dabei auftretenden Fraktionierungsprozesse wird in dieser Arbeit durchgeführt unter Nutzung einer Thermodynamik-Software mit enthaltenem Hydratbildungsmodul. Dabei ist die Phasenverschiebung vor allem auf das CO₂/CH₄-Verhältnis sowie auf den Einfluss von Stickstoff und Schwefelwasserstoff zurück zu führen.

Table of Contents

1. Carbon dioxide in deep seawater	1
2. Hydrothermal fluids	3
2.1. Formation of hydrothermal fluids.....	3
2.2. Geochemical variability of hydrothermal fluids.....	5
2.2.1. Phase separation and segregation	6
2.2.2. Gas fractionation.....	7
2.3. Distribution of hydrothermal fluids in the water column	8
3. Study areas	10
3.1. Hatoma Knoll (HK).....	11
3.2. Yonaguni Knoll IV (YK).....	13
4. Methods and materials	15
4.1. Investigation of the water column	15
4.1.1. In situ measurements (CTD, pH, Eh, LADCP)	16
4.1.2. Helium sampling and measurement.....	19
4.1.3. Total CO ₂ and alkalinity sampling and measurement	20
4.2. Investigation of the rising condensed phases	21
4.2.1. Sampling of the condensed phase	21
4.2.2. First processing onboard.....	23
4.2.3. Measurements in the laboratory.....	24
4.2.3.1. Helium measurement	25
4.2.3.2. Determination of stable carbon isotope ratio	25
4.2.3.3. Determination of gas composition.....	26
4.2.4. Further experiments during the dives	29
4.3. Phase Calculations	30
5. Geochemical observations within the water column at HK and YK	33
5.1. Reference stations.....	33
5.2. Distribution of vent-induced anomalies	34
5.3. ³ He ^{excess} , ΔC _T and their relationship	38
5.4. Correlation between ΔC _T and pH	43
5.5. Characteristics of stations 57 and 59	46
5.6. Expected geochemical signature of the lowermost water column	48
6. Geochemical variability of the condensed phases at HK.....	49

6.1.	Differences between individual emission sites	49
6.1.1.	Dive 199	50
6.1.2.	Dive 200	50
6.1.3.	Dive 202	51
6.2.	Variability of the gas composition	53
6.2.1.	CO ₂ -dominated condensed phases	54
6.2.2.	Non-CO ₂ -dominated condensed phase.....	55
6.3.	Potential origin of the gas components	55
6.3.1.	Carbon dioxide	57
6.3.2.	Methane	58
6.3.3.	Hydrogen and Hydrogen sulfide	60
6.3.4.	Residual gases (Nitrogen, Argon, Helium)	61
7.	Phase condition and behavior of the condensed phases	62
7.1.	Theoretical considerations.....	63
7.1.1.	Phase transformation between liquid and gaseous phase	63
7.1.2.	Formation of gas hydrates	66
7.1.3.	Phase behavior calculated for sample composition.....	70
7.1.4.	Possible phase change and fractionation processes.....	76
7.2.	Conclusions on phase behavior under in situ conditions	77
7.2.1.	Dive 200, GS 3	78
7.2.2.	Dive 202, GS 2	80
7.2.3.	Dive 202, GS 3	80
7.2.4.	Dive 202, GS 4	81
7.2.5.	Aggregate states of condensed phases.....	83
7.3.	Potential processes inducing geochemical variability.....	84
8.	Summary.....	90

List of figures

Fig. 1: Phase diagram and density of carbon dioxide in seawater.....	2
Fig. 2: Formation of hydrothermal fluids.....	3
Fig. 3: Formation of hydrothermal active sites.....	4
Fig. 4: Variability of gas composition and gas content in hydrothermal fluids.....	7
Fig. 5: Bathymetric map of the OT, YK and HK.....	12
Fig. 6: Water sampling stations of YK and HK.....	15
Fig. 7: Adjustment of pH profiles to the reference profile.....	18
Fig. 8: Sampling sites of condensed phases.....	22
Fig. 9: Gas chromatographic measurement system.....	26
Fig. 10: Bubble box.....	29
Fig. 11: Vertical profiles of geochemical parameters at the reference stations.....	34
Fig. 12: Vertical profiles of geochemical parameters at selected stations from both research areas.....	35
Fig. 13: Plot of $^3\text{He}^{\text{excess}} / ^4\text{He}^{\text{tot}}$ against $\delta^3\text{He}$	38
Fig. 14: Plot of ΔC_T against $^3\text{He}^{\text{excess}}$	39
Fig. 15: T/S- diagram of selected stations from both research areas.....	42
Fig. 16: Plot of ΔC_T against ΔpH	45
Fig. 17: Vertical profiles of geochemical parameters at stations 57 and 59.....	47
Fig. 18: Formation of gas hydrate pipes and accumulation.....	49
Fig. 19: Shape and behavior of rising condensed phase.....	50
Fig. 20: Proximity of low-temperature and warm vents.....	53
Fig. 21: Assumed sources of gases at the HK.....	57
Fig. 22: Bernard diagram.....	59
Fig. 23: Scheme of calculated phase change processes.....	62
Fig. 24: Dew and bubble point curves depending on CO_2/CH_4 -ratio.....	64
Fig. 25: Dew and bubble point curves depending on N_2 and H_2S content.....	65
Fig. 26: Gas hydrate phase boundary depending on gas composition.....	66
Fig. 27: Mole fraction of compounds in gas hydrate.....	69
Fig. 28: Dew, bubble point, and GH phase boundary curves of GS 3, dive 202.....	70
Fig. 29: Dew, bubble point, and GH phase boundary curves of GS 4, dive 202.....	72

Fig. 30: Dew, bubble point, and gas hydrate phase boundary curves of GS.....	73
Fig. 31: Mole fraction of compounds in gas hydrate of GS.....	75
Fig. 32: Plot of density against temperature.....	78
Fig. 33: Pressure-dependent gas composition in the GS.....	79
Fig. 34: p/T-expansion experiment.....	80
Fig. 35: Phase diagram of dive 202, GS 3.....	82
Fig. 36: Phase diagram of GS.....	84
Fig. 37: Possible subseafloor processes.....	86

List of Tables

Table 1: Sampled condensed phases at the HK.....	22
Table 2: Measurement range of the gas chromatography system	25
Table 3: Maximum geochemical values.....	37
Table 4: Gas composition of the GS fractions.....	52
Table 5: Mole fractions of condensed phases and corresponding gas hydrates	68

Abbreviations

BAB	back-arc basin
C ₁ – C ₆	hydrocarbons with 1 up to 6 C atoms
CCS	carbon capture and storage
CTD	Conductivity-temperature-depth-instrument
DIC	dissolved inorganic carbon (described as C _T in this thesis)
GC	gas chromatograph, equipped with PDD: pulse discharge detector TCD: thermal conductivity detector V ₁ -V ₃ : valves 1 to 3 VACDOS: manometric vacuum dosing system
GH	gas hydrate
GHSZ	gas hydrate stability zone
GS	gassampler
HK	Hatoma Knoll
LADCP	lowered acoustic Doppler current profiler
LOD	limit of detection
LOQ	limit of quantification
MOR	mid-ocean ridge
MORB	MOR basalts
n.d.	not detected
OT	Okinawa Trough
R/V	research vessel
ROV	remotely operated vehicle
SEPR	Southern East Pacific Rise
YK	Yonaguni Knoll IV

Formula symbols

a	$[K^{1/2} \cdot m^5 \cdot s^{-2} \cdot mol^{-2}]$	cohesion pressure (constant that corrects for attractive potential of molecules in real gases)
α	$[m^5 \cdot s^{-2} \cdot mol^{-2}]$	constant that corrects for non-ideal shape of molecules in real gases
A_T	$[\mu mol \cdot kg^{-1}]$	total alkalinity in water
b	$[m^3 \cdot mole^{-1}]$	co-volume (constant that corrects for volume in real gases)
C_T	$[\mu mol \cdot kg^{-1}]$	total carbon dioxide content in water, in this work also difference to reference station (ΔC_T) is used
$\delta^{13}C$	[‰]	carbon isotopic signature of the stable isotopes ^{13}C and ^{12}C in methane ($\delta^{13}C(CH_4)$) or carbon dioxide ($\delta^{13}C(CO_2)$)
Eh	[mV]	redox potential, in this work first derivate with respect to time (dEh/dt [$mV \cdot s^{-1}$]) is used
He		helium concentration and isotope ratio are described as <ul style="list-style-type: none"> • 3He [ppt], 4He [ppm]: volume fraction of 3He and 4He, respectively, in the sampled condensed phases • $^3He^{excess}$ [$\mu mol \cdot kg^{-1}$]: enrichment of 3He in the water compared to concentration at equilibrium with atmosphere • $^4He^{tot}$ [$\mu mol \cdot kg^{-1}$]: total measured 4He in the water sample • R: helium isotope ratio ($^3He/^4He$) as a multiple of the atmospheric ratio (R_{atm}) • δ^3He [%]: percentage deviation of the helium isotope ratio (R) from the ration in air (R_{atm})
pH	[]	measure of the acidity or basicity of an aqueous solution (negative common logarithm of the activity of hydronium ions), also the difference to reference station (ΔpH) is used
p	[bar, MPa] [dbar]	pressure water depth
R	$[J \cdot K^{-1} \cdot mole^{-1}]$	universal gas constant ($8,314 J \cdot K^{-1} \cdot mole^{-1}$)
ρ	$[g \cdot cm^{-3}]$	density
$\sigma_{1.5}$	$[\mu mol \cdot kg^{-1}]$	potential density, referenced to 1500 dbar

S	[pss-78]	salinity
T	[°C]	temperature
V_m	[m ³ · mole ⁻¹]	molar volume
x	[ppm, mole-%]	mole fraction

Definitions

In the submarine hydrothermal scientific field a lot of specific terms are used, which partly will not explained within the text of this thesis. Hence, a short overview about most of these used words will be given in the following.

Due to circulation and interaction of hot water with rocks and the earth's crust at hydrothermal active sites within the oceans, **hydrothermal fluids** are generated and mostly emitted into the aquatic environment as **plumes**. Openings or fissures in the oceanic floors (**vents**) allow the release of the hydrothermal fluids into the water column. A significant amount of heavy metals and minerals are dissolved in the hydrothermal fluids and cause different coloration. The presence of iron, manganese, zinc and sulfur, and barium, calcium and silicon lead to the emission of the fluids by **black and white smokers**, respectively. The emitted fluids are very hot, black smokers emit fluids with temperatures up to 400°C. Fluid temperatures at white smokers are in the range of 100 to 330°C. Contact with cold ambient water causes precipitation of the minerals, which on the one hand explains the intensive color of the fluids, but on the other hand forms cylindrical stacks of minerals, also known as **chimneys**. At white smokers with fluid temperatures at the lower end of the range or in the absence of coloring minerals, **clear fluids or diffuse flow** are emitted.

Chemical and geophysical conditions at hydrothermal active sites can promote the formation and emission of gas bubbles and droplets, hereafter called **condensed phases**. This term summarizes the gaseous and liquid phases in case of unknown phase condition.

Preface

This thesis investigates CO₂-rich fluids and condensed phases at two natural emission sites in the southern Okinawa Trough (Yonaguni Knoll IV and Hatoma Knoll) where emission of liquid carbon dioxide has been previously reported [Konno *et al.*, 2006; Shitashima *et al.*, 2008]. During a cruise with the German R/V *Sonne* (SO 196-2, SUMSUN: Studies of marine CO₂-sequestration associated with a natural hydrothermal CO₂-system of the Northern West Pacific) in March 2008, both research areas were investigated by an interdisciplinary approach, including physical and chemical oceanography, marine geochemistry and microbiology. These research areas serve as natural analogues for sub-sedimentary CO₂ sequestration in the deep-sea to investigate the effect of leaking CO₂ on the ecosystem. The influence of the high CO₂ concentration on biological processes and microbial activity in the sediment and porewater geochemistry was investigated during the cruise [de Beer *et al.*, 2013; Häckel, 2011; Neumann, 2012; Yanagawa *et al.*, 2012]. Also bathymetric mapping with a multibeam and water column imaging with a Parasound system have been conducted [Rehder and Schneider von Deimling, 2008].

Chapter 1 illustrates the potential aggregate phases of carbon dioxide in seawater, **Chapter 2** gives a brief overview about the formation and distribution of hydrothermal fluids in submarine systems and the mechanisms responsible for geochemical variability. In **Chapter 3** the research areas Hatoma Knoll and Yonaguni Knoll IV are characterized. In **Chapter 4** the measurement systems and methods that have been used during cruise SO 196-2 and for subsequent laboratory work are described. In **Chapter 5** the water column of both hydrothermal systems are characterized under usage of the sensor-based pH and Eh measurements. The influence of the CO₂-rich hydrothermal plumes on pH and emission fluxes is estimated.

A total of six condensed phases were sampled in the Hatoma Knoll research area by the ROV. The description of the vents as well as the gas-chemical measurements are reported in **Chapter 6**. Based on the gas composition and further geochemical tracers, potential sources of the individual gases are estimated. The influence of the gas composition on the phase conditions of the condensed phases in the deep water is based on calculations made by the Infochem Multiflash software package and

described in *Chapter 7*. In combination with the results from the gas-chemical measurements, onboard experiments, video material and ROV data, the phase condition of the condensed phases in situ is indicated. The results hint on probable subseafloor phase transformation and fractionation processes which may be responsible for the variability in gas composition of the condensed phases. The thesis is briefly summarized in *Chapter 8*.

Parts of the article “Geochemical observations within the water column at the CO₂-rich hydrothermal systems Hatoma Knoll and Yonaguni Knoll IV, in the southern Okinawa Trough” which is published in *Journal of Geophysical Research: Oceans* on 9 September 2016 with the Co-Authors A. Buss, B. Schneider, J. Schneider von Deimling, J. Sültenfuß, M. Walter, Ch. Mertens, G. Rehder¹ are partially cited verbatim within this thesis. The text passages are marked accordingly. Minor changes like addition or omission of individual words to enhance the comprehensibility are marked with square brackets, e.g. „In [the year] 2000“ or “Sampling of the [...] condensed phases“. I am the first and responsible author of the publication. Hence, I compiled almost all the data, put forward the main hypothesis of the discussion and wrote the draft for publication. My own contribution is specified at each citation.

¹ Kedzior, S., A. Buß, B. Schneider, J. Schneider von Deimling, J. Sültenfuß, M. Walter, C. Mertens, and G. Rehder (2016), Geochemical observations within the water column at the CO₂-rich hydrothermal systems Hatoma Knoll and Yonaguni Knoll IV, in the southern Okinawa Trough, *J. Geophys. Res. Oceans*, 121, 6618–6634, doi:[10.1002/2016JC012003](https://doi.org/10.1002/2016JC012003).

1. Carbon dioxide in deep seawater

Carbon dioxide (CO₂) is known as a greenhouse gas. Its atmospheric concentration is constantly increasing since the beginning of the Industrial Revolution in the 19th century, mainly due to the consumption of fossil fuels. The anthropogenic emission leads to global warming and climate change. Several techniques have been developed, determined, and analyzed to capture CO₂ emitted from power plants and other industrial and energy-related sources and to store it safely to stabilize the atmospheric CO₂ concentration (Carbon Capture and Storage, short CCS). Biological and chemical transforming procedures as well as storage of CO₂ in various geological formations onshore and offshore have been investigated (e.g. *Bushuyev et al.* [2018], *Herzog and Golomb* [2004], *Rackley* [2017]). A further development of these ideas is the injection of carbon dioxide in deep ocean water and sediments [*Adams and Caldeira*, 2008; *House et al.*, 2006]. The enormous storing capacity as well as the physical- and geochemical processes occurring under the prevailing temperature and pressure conditions initiates further interest in this form of CO₂ sequestration.

Below about 4 to 5 MPa, pending on temperature, carbon dioxide is in the liquid aggregate state (CO₂ (l), Fig. 1a). Liquid CO₂ is highly compressible, so it becomes denser than seawater at high pressure and low temperature. However, this state is only reached at pressures of at least about 27 MPa [*Honda et al.*, 1995]. Even though, injection of CO₂ in deep oceans or deep ocean sediments in water depths of at least 3,000 m allows the liquid carbon dioxide to descend due to its density and to form a CO₂ (l) lake [*Nealson*, 2006]. Above this water depth the density of liquid CO₂ is too small compared to the ambient seawater or pore fluids, hence an injection in deep water or sediment, respectively, is ineffective due to fast ascent (Fig. 1b). The difference of the densities between seawater and CO₂ is proportional to the buoyancy. At water depths of less than about 3,000 m liquid carbon dioxide droplets rise up. The density of CO₂ (l) decreases during the ascent while the density of the seawater remains almost unchanged (Fig. 1b). Hence, the difference of the densities increases and thus the buoyancy and rising velocity (on the assumption of droplet size constancy).

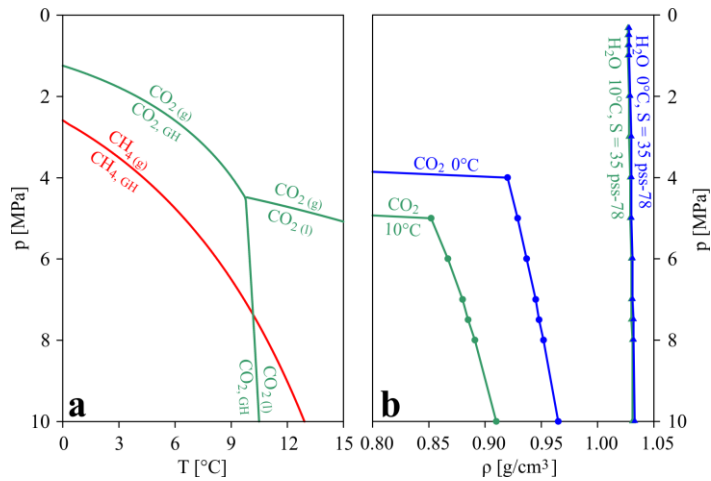


Fig. 1: (a) Phase diagram of the phase boundaries between pure gaseous, liquid, and carbon dioxide as gas hydrates (CO_2 (g), CO_2 (l), CO_2 (GH)) in dependency of pressure (reverse scale to illustrate water depth) and temperature, calculated with CSMGem. The gas hydrate phase boundary of methane illustrates the transition to gaseous methane (CH_4 (g) to CH_4 (GH)). (b) Vertical profiles of the densities of carbon dioxide (●, *Span and Wagner* [1996]) and seawater (▲) at 0°C (blue) and 10°C (green). The pressure dependency of the density decreases abruptly at pressures higher than about 4 or 5 MPa at 0°C or 10°C, respectively due to less compressibility of liquid CO_2 compared to the gaseous bubbles.

The ascent of CO_2 through the sediment and water column is also affected by another phase changing process: the formation of gas hydrates (GH). These ice-like, crystalline structures trap ‘guest’ molecules in hydrogen-bonded cages of water molecules (‘host’). With CO_2 the host molecules form a framework of structure I (sI), the clathrate has an average molecule ratio of $5.75 \text{ H}_2\text{O} \cdot \text{CO}_2$ [*Circone et al.*, 2003]. The GH phase boundary of carbon dioxide is reached at relatively low water depths and temperatures in comparison to methane (Fig. 1a). Below about 10°C CO_2 -GH can be formed within a wide p-T-range (GHSZ: **g**as **h**ydrate **s**tability **z**one), both from gaseous and liquid CO_2 .

2. Hydrothermal fluids

The following chapter includes content of the article “Geochemical observations within the water column at the CO₂-rich hydrothermal systems Hatoma Knoll and Yonaguni Knoll IV, in the southern Okinawa Trough”. The quoted section is marked and the contribution footnoted.

2.1. Formation of hydrothermal fluids

The release of hydrothermal fluids from the seafloor into the water column can be observed worldwide along tectonic plate boundaries. Movement of the tectonic plates cause the generation of a spreading center. Hydrothermal fluids originate from seawater, which penetrates through cracks and faults of the newly formed crust of these spreading centers (recharge zone; Fig. 2), where magma chambers occur due to mantle melting. High pressure and temperature within the earth’s crust lead to fluid-rock or fluid-magma interactions, which alter the chemical composition of the seawater (reaction zone; Fig. 2).

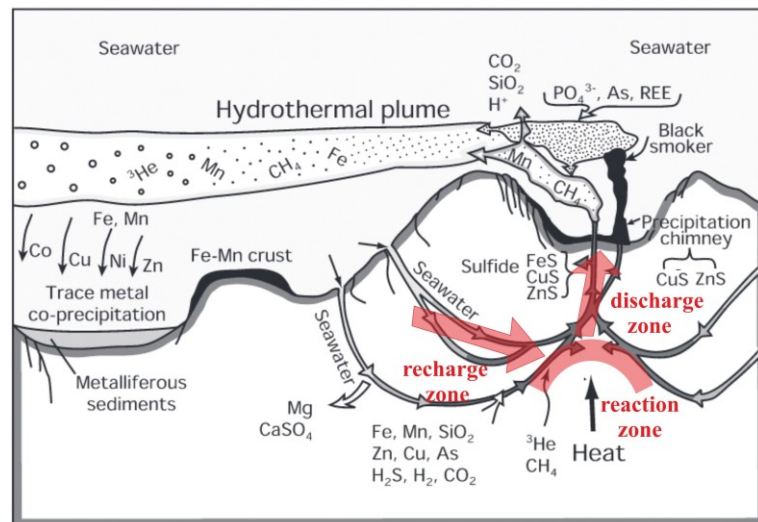


Fig. 2: Formation of hydrothermal fluids (after Gamo *et al.* [2006]).

The reaction of saltwater with the rocks and host basalt at high temperatures or exchange processes with the molten material enriches the fluids with metals, volatiles, and energy [Shitashima, 1997]. Because of their lower density, these fluids rise buoyantly towards the seafloor [Baross and Hoffman, 1985; Massoth *et al.*, 1989] (discharge zone; Fig. 2). Depending on chemical and especially mineral composition

they are emitted by hot black or hot white smokers or by vents and seeps as clear fluids (hot or cold) (e.g. *Ishibashi et al.* [2006]; *Massoth et al.* [1989]).

The majority of hydrothermal vent sites is found at mid-ocean ridges (MORs). Divergent tectonic plates cause the generation of a spreading center (left side of Fig. 3), where new oceanic crust is created and hydrothermal fluids are emitted.

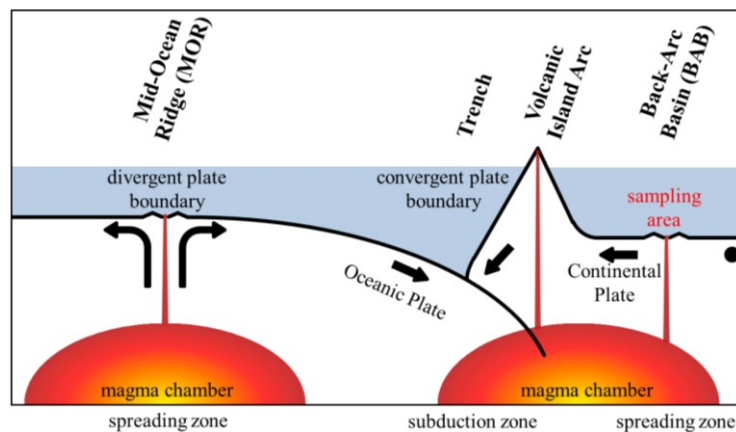


Fig. 3: Formation of hydrothermal active sites at Mid-Ocean Ridge (MOR; left) and Back-arc basin (BAB; right).

The formation of spreading zones at back-arc basins (BABs) are much more complex (right side of Fig. 3). They arise as a result of extension related to convergent plate movement. There are two different hypothesis of BAB formation, which differ in the moving direction of the overriding plate after subduction [*Sdrolias and Müller, 2006*]. The most commonly proposed mechanism is ‘trench roll back’ [*Hawkins et al., 1984; Saunders and Tarney, 1984*]. The subducted plate (oceanic plate) slides under a trailing plate (continental plate) and sinks into the mantle. Subduction leads to the formation of an oceanic trench and an arc-forming elevation (Volcanic Island Arc) behind it. Convergent motion of the trench in the seafloor direction in conjunction with partial fixation of the trailing plate (• in Fig. 3) builds up tensional forces at the continental plate. The overriding plate behind the Island Arc undergoes crustal thinning due to the extensional forces. It results in the opening of back-arc spreading centers, while the magma of the melting subducted plate rises to fill the created space [*Martinez et al., 2007*].

Most BABs are located at the western boundary of the Pacific Ocean [Martinez *et al.*, 2007], e.g. Okinawa Trough, Mariana Trough, Lau Basin. The majority of them show hydrothermal activity [Craig *et al.*, 1987; Glasby *et al.*, 2006; Ishibashi and Urabe, 1995] with methane-, carbon dioxide-, and sulfur dioxide-enriched fluids [Gamo, 1995; Horibe *et al.*, 1986; Monecke *et al.*, 2014; Sakai *et al.*, 1990a; 1990b]. CO₂-dominated hydrothermal fluids are limited to BABs due to the plate tectonic constellation of a subducting oceanic plate with large sedimentary deposit rich in carbonate (Chapter 2.2).

2.2. Geochemical variability of hydrothermal fluids

Depending on the amount of the seafloor fluid-rock interactions, temperature, depth of reaction zone, and age of hydrothermal system, components within the fluids can vary [Gamo, 1995]. Even the rock type influences the geochemical composition. In case of BABs, the subducted plate has considerable imprint on the fluid composition. Carbon-rich materials like limestone, carbonates, and organic matter undergo thermal alteration (decarbonation or thermal cracking) in the magma generation zone, leading to the emission of fluids which are rich in carbon dioxide. Interactions between magma or rising hot fluids with organic matter, calcium carbonate, and trapped volatiles in the overlying crust and sediment of the subducted plate furthermore increase the CO₂ content [IEA Report, 2008; Marty *et al.*, 1989; Shitashima, 1997]. The residual chemical composition of the fluids is influenced by supplementary deposited material [Ishibashi *et al.*, 1995].

The release of CO₂-rich fluids “leads to the reduction of the pH in the surrounding water column, and in some cases governs the pH change almost entirely (e.g., NW Eifuku, Resing *et al.*, [2009]). However, hydrothermal fluids at BABs are often also characterized by high acidic sulfur compound contents, emitted mainly as sulfur dioxide or sulfurous acid, leading to a considerable reduction of the pH of the fluids to

values as low as 2.39 [Takai *et al.*, 2008], and therefore also might contribute to acidification in and near the hydrothermal plume”² [Tunnicliffe *et al.*, 2009].

Furthermore, other processes seem to affect fluid composition heavily at several hydrothermal vent sites. These ‘secondary modification processes’ [Gamo, 1995] take place in the sedimentary layer before fluids are released into the water column and might influence whether fluids are emitted as black, white, or clear smoke or as diffuse flow. These processes include interaction with sedimentary layers, downward penetration or leakage of cold bottom water, and cooling due to conductive heat loss [Butterfield *et al.*, 1990; Gamo, 1995]. One of the most important and common secondary processes is phase separation and segregation (Chapter 2.2.1). Additionally, gas fractionation due to subseafloor GH formation has been observed at some BABs, that further influences the variability of hydrothermal fluids regarding gas composition (Chapter 2.2.2).

2.2.1. Phase separation and segregation

At several hydrothermal vent sites, fluids show strong differences in salinity with both spatial and temporal variation (e.g. Butterfield *et al.* [1990]; Von Damm *et al.* [1997]). Although ambient seawater is the initial source of all these fluids, salinity differs considerably either with extreme depletion or enhancement [Massoth *et al.*, 1989; Von Damm and Bischoff, 1987; Von Damm *et al.*, 1985]. Gas content and composition varies between these low- and high-saline fluids as well.

During their rise through the rock, hot hydrothermal fluids tend to get separated into a brine and a gas-rich vapor phase. Depending on pressure conditions during this phase separation process, either a low-salinity vapor and a high-salinity brine phase is formed due to boiling seawater (subcritical phase separation), or only a small quantity of dense brine is generated with large amounts of a high-saline vapor phase because of decompression and condensation (supercritical phase separation) [Coumou *et al.*, 2009]. Different buoyancies and mobilities of both brine and vapor phases lead to

² My contribution of the cited part included all writing, which was proof-read by the co-authors.

subsequent segregation [Butterfield *et al.*, 1990]. As a consequence of these combined phase separation and segregation processes the emission of fluids differing in their salinities, as well as in their gas contents were observed.

2.2.2. Gas fractionation

For three arc-related hydrothermal systems (Mariana Arc, Manus Basin, Okinawa Trough), the emission of droplets from the seafloor mainly composed of liquid CO₂ has been previously reported [Bach, 2011; Lupton *et al.*, 2006; Sakai *et al.*, 1990a]. For one more system it is likely to occur due to visual observation (Samoan Hotspot; Staudigel *et al.* [2006]), however the droplets have not been sampled or further considered up to now (latest revision: February 2021). The first report of the emanation of liquid CO₂ droplets in a water depth of 1550 m has been made by Sakai *et al.* [1990a] in the JADE Field, Izena Hole (Okinawa Trough). According to their conceptual model, a CO₂-rich vapor phase, that is produced by subseafloor boiling, is subsequently cooled down during the ascent through the rock and sediment. In the upper sediment at temperatures below 10°C the rising fluids pass the GHSZ. The clathrates form a hydrate cap and CO₂ accumulates below the sediment surface. When the hydrate cap is ruptured, pressure and temperature conditions facilitate the release of liquid CO₂ into the bottom water.

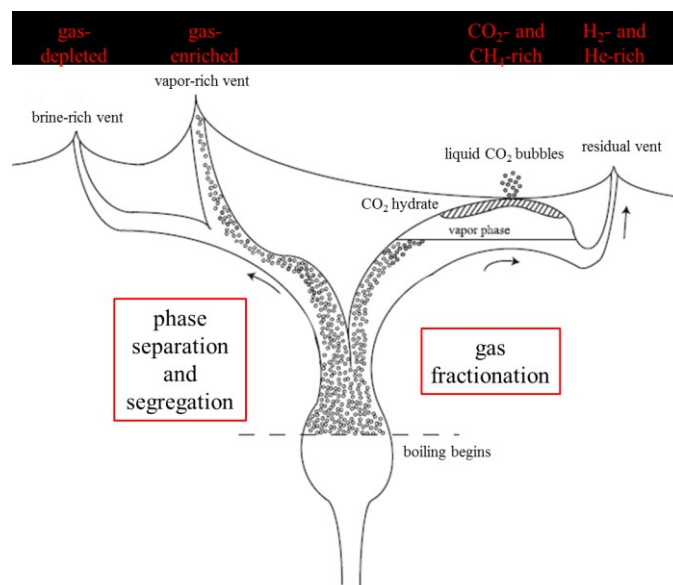


Fig. 4: Mechanism to explain the variability of gas composition and gas content in hydrothermal fluids (after Konno *et al.* [2006]).

Konno et al. [2006] adopted this theory to explain the different gaseous composition of fluids and CO₂ droplets at Yonaguni Knoll IV. They suggested, that liquid CO₂ arises from thermally driven decomposition of seafloor CO₂ hydrates, which were formed by cooling of fluid vapor that has been produced by phase separation (Fig. 4). Due to their different tendency to stabilize a GH cage, the formation of GH leads to seafloor gas fractionation, especially between hydrate-forming gases like CO₂ and CH₄, and light gases like H₂, that are not incorporated into the GH lattice.

2.3. Distribution of hydrothermal fluids in the water column

Emitted fluids from hot vents usually have a lower density than the ambient bottom seawater. Hence, the occurring buoyancy forces lead to continuous and rapid rising of the plume through the water column up to water depths with similar density. During the rise of these buoyant plumes, Eddie turbulences arise at the lateral boundary, causing mixing with seawater. This, on the one hand leads to continuous dilution of the fluids out of the plume, and on the other hand to salt flux from ambient water into the plume resulting in fast decrease of temperature and particle concentration within the plume. In the Pacific Ocean this process leads to an increase of salinity and therefore also in density of the fluids, because of the relatively saline bottom water. The buoyancy of the plume decreases and the plume reaches its density equilibrium in relatively low heights. On the contrary, in the Atlantic Ocean unstable salinity conditions of the background (low salinity in the bottom waters) induce flux of salt-poor water into the plume, which leads to a decrease in density and an increase in buoyancy. Therefore hot fluids in the Atlantic tend to rise higher than in the Pacific Ocean. *Speer and Rona* [1989] developed a model to determine the influence of the background salinity stratification on the maximum rising height. An exemplary calculation of a plume with a source heat flux of about 49 MW yield considerably different rising heights of 180 m for the Pacific Ocean and 330 m for the Atlantic Ocean [*Speer and Rona*, 1989]. Additionally, prevailing bottom water currents can promote the horizontal dispersion of the plume within the water column.

The influence of vent fluids containing CO₂-dominated condensed phases is expected to be limited to the lower part of the water column due to their high solubility in water, and the moderate density difference between seawater and liquid CO₂ in deep oceans (Fig. 1b). Model calculations confirmed that liquid CO₂ droplets, released in water depths between 500 and 2000 m are completely dissolved within less than 200 m [Herzog *et al.*, 1991]. However, field experiments yielded a rising height of individual CO₂ droplets of more than 400 m, but droplets lost 90 % of their mass within the first 200 m [Brewer *et al.*, 2002].

Depending on the release depth, as well as on temperature of the ambient seawater, CO₂ tends to form a GH skin around the condensed phases. It reduces the CO₂ dissolution flux across the boundary layer into the seawater and therefore enhances the lifetime of the droplet or bubble. The decrease of the maximum rising height or even sinking of a GH coated condensed phase back to the seafloor due to an increased density, as reported by Holder *et al.* [1995], is very unlikely.

Bigalke *et al.* [2010] notified, that high background concentrations of gases are required to initiate the formation of GH around the bubbles. Since the surrounding water is undersaturated, a diffusion-controlled dissolution of the GH occurs [Rehder *et al.*, 2004]. Furthermore, experiments indicate that CO₂ droplets were not entirely coated with a GH skin, because of “lower thermodynamic forces and longer induction times for hydrate crystallization” [Bigalke *et al.*, 2010]. Shear forces caused by the ascent results in partially mobile parts at the surface of the condensed phase. Especially the top side of the condensed phase remains clear because the hydrate particles are pushed to the downstream side [McGinnis *et al.*, 2006]. The formation of the GH skin decreases the mass transfer rate [Rehder *et al.*, 2002] and the rising velocity. Uncoated liquid CO₂ droplets rise up through the water column up to 50% faster than droplets coated with a GH skin [Bigalke *et al.*, 2010]. However, sinking of GH coated condensed phases in natural environments have not been reported yet, as the hydrate skin layer at the surface remains too thin to substantially increase the bulk density of the condensed phase.

3. Study areas

The following chapter includes content of the article “Geochemical observations within the water column at the CO₂-rich hydrothermal systems Hatoma Knoll and Yonaguni Knoll IV, in the southern Okinawa Trough”. The quoted sections and sentences are marked and contributions footnoted.

“The Okinawa Trough [OT, also known as Nansei-Shoto Trough [Lee *et al.*, 1980]] is located at the western boundary of the Pacific Ocean between Taiwan and the Japanese Island Kyushu”³ (Fig. 5a). The oceanic Philippine Sea Plate subducts under the continental Eurasian Plate, causing the generation of the Ryukyu Trench and the OT back-arc basin. The OT is in a relatively young stage of evolution. The first phase of crustal stretching and subsidence occurred 9 to 6 Ma ago (late Miocene / early Pliocene) in the north and mid-OT [Letouzey and Kimura, 1985], while high heat flow suggests an age of only 2 Ma for the southern OT [Lu *et al.*, 1981].

Sediments in the OT consist primarily of terrigenous material from the Asian continental shelf and island arc [Lee *et al.*, 1980; Letouzey and Kimura, 1986; Sibuet *et al.*, 1987] and differ in thickness between more than 8 km in the northern and on average 1 to 2, maximum 4 km in the southern OT [Letouzey and Kimura, 1986].

“Halbach *et al.* [1989] were [...] the first to report about back-arc related volcanism in the OT, and discovered the JADE hydrothermal field, showing sites which were interpreted as modern analogues for massive ore formation. The JADE field also hosts the first known location of marine liquid CO₂ formation [Sakai *et al.*, 1990b]. Since then, several additional hydrothermal vent [areas] have been discovered in the OT (Minami-Ensei, Iheya North, CLAM, Yoron Hole, JADE, Irabu Knoll, HAKUREI, Hatoma Knoll, and Yonaguni Knoll IV; Kawagucci *et al.* [2010], Watanabe *et al.* [2006])”⁴. They are located in the southern and mid-OT because crustal separation and active spreading seems to be restricted to that area [Kimura, 1985; Letouzey and Kimura, 1986]. Subseafloor fluid advection at several of these hydrothermal systems has been investigated within the TAIGA project [Ishibashi *et al.*, 2015].

^{3, 4} My contribution of the cited part included all writing, which was proof-read by the co-authors.

The discovery of hydrothermal CO₂-rich fluids in the mid-OT showed that CO₂ fluxes of arc- and back arc-systems are much more important than assumed before [*Sakai et al.*, 1990b]. A lot of different hydrothermal vent types have been observed at the OT, ranging from hot, smoky black fluids with temperatures up to 364.1°C, over high-temperature clear fluids to colder transparent fluids, sometimes containing CO₂ droplets [*Inagaki et al.*, 2006; *Miyazaki et al.*, 2017; *Suzuki et al.*, 2008].

Surface water circulation is dominated by the Kuroshio current. It is the most important water current at the western boundary of the North Pacific Ocean and has its origin in the North Equatorial Current and the current east of Taiwan and the Luzon Island [*Chen and Wang*, 1998]. The Kuroshio “enters the East China Sea through the passage east of Taiwan and flows northeastwards along the western boundary of the OT [...]. In the southernmost part of the OT, the Kuroshio current influences the surface water down to a depth of about 500 m with average velocities of up to about 70 cm · s⁻¹ [*Nakamura et al.*, 2008].”⁵ Subsurface countercurrents influence the water at intermediate depths (~500 m) as well [*Nakamura et al.*, 2008]. During cruise SO 196-2 maximum velocities of 120 cm · s⁻¹ have been measured in the upper 500 m of the water column and up to 30 cm · s⁻¹ close to the seafloor (~1300 m) [*Buß*, 2011].

3.1. *Hatoma Knoll (HK)*

Hatoma Knoll “is a submarine volcano located at the southwestern end of the OT (24° 51.3' N, 123° 50.5' E; Fig. 5a). The hydrothermal active area is located within a caldera hosting a dacitic dome, occurring in an average depth of about 1530 m (Fig. 5c), and was discovered in 1999 by the submersible ‘SHINKAI 2000’ [*Watanabe*, 2001]. The up to 140 m high and 500 m wide caldera is almost completely closed except for a small breach at the southern rim, probably resulting from a former flank collapse and slumping [*Rehder and Schneider von Deimling*, 2008; *Shitashima et al.*, 2008].”⁶

^{5,6} My contribution of the cited part included all writing, which was proof-read by the co-authors.

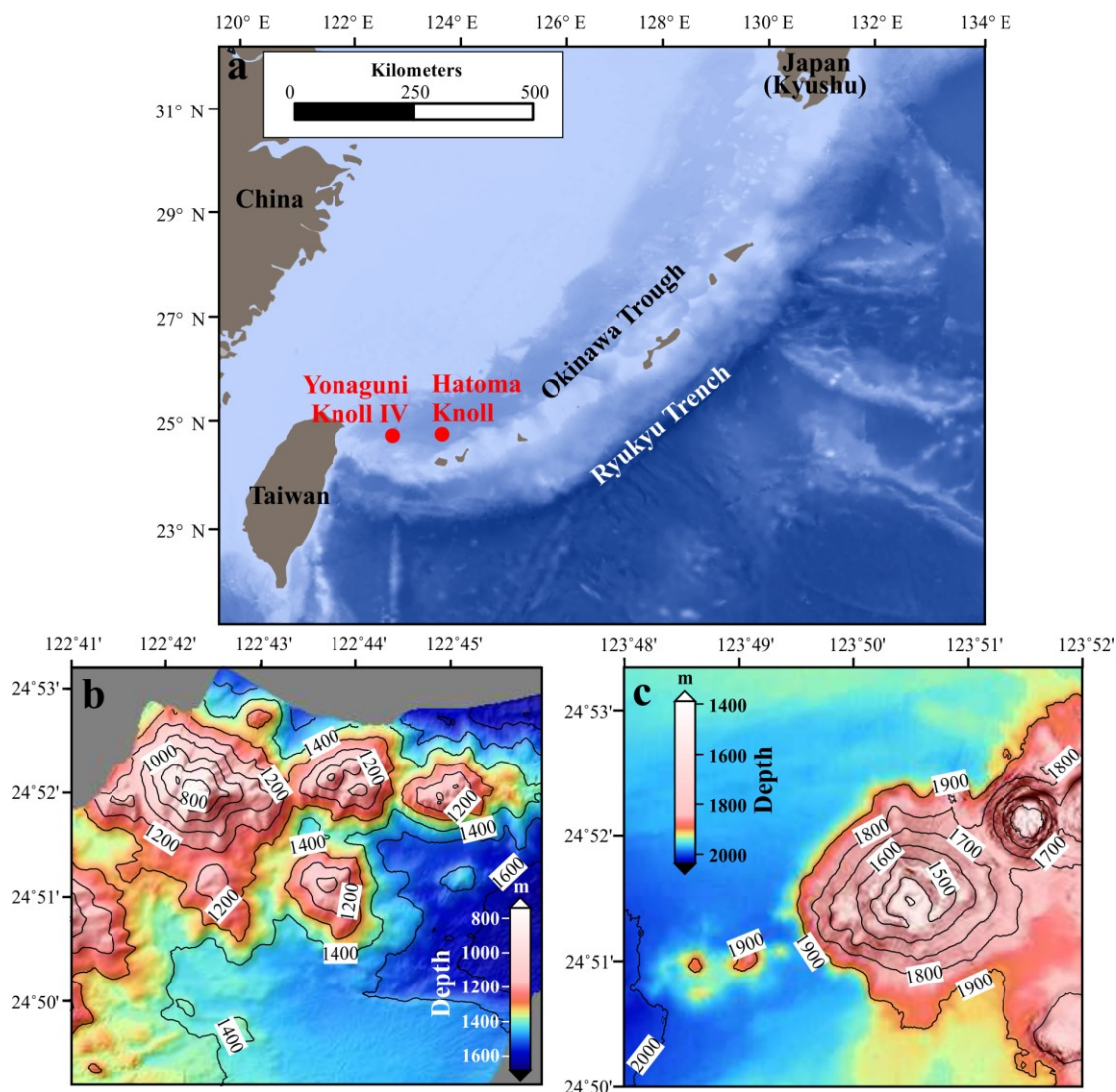


Fig. 5: “Bathymetric maps of the OT, based on (a) GEBCO_08 Grid and the research areas (b) YK and (c) HK, based on data from cruise SO 196-2.”⁷

Compared to the several km thick sediments at the residual OT, the seafloor within the caldera at HK is sediment-starved. During several cruises and dives of ROVs ‘SHINKAI 200’ and ‘Hyper-Dolphin’ a large number of active and inactive vent sites and chimneys have been located in water depths between 1460 and 1515 m “in the middle of the caldera close to a round-shaped 30 m high mound, and at the northwestern inner-side rim of the caldera”⁸ [Furushima and Yamamoto, 2015; Watanabe, 2001] (Fig. 6b). The highest hydrothermal activity at HK is located in the center of the caldera. “In [the year] 2000 a large chimney with a height of more than

⁷ These figures and caption are used in the article mentioned above. Processing of raw data provided by M. Glockzin (Fig. 5a) and J. Schneider von Deimling (Figs. 5b and 5c), respectively. Construction and compilation of the figures was done by myself.

⁸ My contribution of the cited part included all writing, which was proof-read by the co-authors.

10 m was discovered, emitting clear hydrothermal fluids with temperatures of up to 301°C [Watanabe, 2001]. In contrast to this hot vent, the less intense and cooler outlets located at the northwestern inner-side of the caldera wall emit liquid CO₂. The small droplets (8 - 10 mm in diameter, volume of ~ 0.5 ml) were reported to contain 95 - 98 % CO₂ and to rise from the seafloor to a height of up to 745 m [Shitashima and Maeda, 2005; Shitashima et al., 2008].”⁹

3.2. Yonaguni Knoll IV (YK)

Yonaguni Knoll IV “(24° 50.9’ N, 122° 42.0’ E) is an elongated valley with a length of about 1000 m, [a] width of 500 m and a maximum water depth of about 1400 m [Suzuki et al., 2008]. It is located about 60 nautical miles west of HK (Fig. 5a). The valley is surrounded by several seamounts with heights reaching 745 m water depth, and was discovered in 2000 by submersible ‘SKINKAI 6500’ [Matsumoto et al., 2001] (Fig. 5b).

Seven active venting sites have been identified at the YK field, named Lion, Crystal, Tiger, and Swallow chimney, Abyss vent, Carp, and Mosquito chimney (from north to south; Fig. 6a) [Gena et al., 2005], some of which emit hot fluids with temperatures [of] up to 330°C from black and clear smoker vents [Inagaki et al., 2006; Nunoura and Takai, 2009; Suzuki et al., 2008].”¹⁰ During cruise SO 196-2 high temperature clear fluids up to 248°C have been detected (24°50.616’ N, 122°42.166’ E). “Emissions of cold liquid CO₂ were observed south of Tiger and northeast of Swallow chimney [Konno et al., 2006]. The cold and hot venting sites differ in their chemical composition with regard to CO₂, H₂, and CH₄ concentrations.”¹¹ This has been attributed to subseafloor phase separation, segregation and fractionation [Konno et al., 2006; Suzuki et al., 2008].

“The seafloor at YK is mainly covered with muddy sediments of terrigenous origin [Suzuki et al., 2008], and is strongly affected by carbonate and silicate weathering at the vent sites”¹² [Häckel, 2011]. Sulphide deposits have been observed in the vicinity

⁹ - ¹² My contribution of the cited part included all writing, which was proof-read by the co-authors.

of active chimneys, which promote the accumulation of chemosynthetic fauna, including the mussel *Bathymodiolus platifrons*, the shrimp *Alvinocaris longirostris*, the crab *Shinkaia crosnieri* [de Beer et al., 2013], and microbial communities at the seafloor [Matsumoto et al., 2001; Nunoura and Takai, 2009; Nunoura et al., 2009]. However, microbial investigations in the CO₂-rich sediments indicate that increasing pore-water CO₂ concentrations cause a decrease in microbial abundance and diversity [Yanagawa et al., 2012].

Several studies regarding the chemical composition of fluids and biodiversity have been carried out at YK since its discovery [Konno et al., 2006; Neumann, 2012]. These were partially motivated by the potential of this site to be used as natural analogue for the disposal of anthropogenic CO₂ in deep-sea ocean sediments, and as a test field to investigate the effects of high pCO₂ / low pH on biological communities [Neumann, 2012; Nunoura and Takai, 2009; Nunoura et al., 2009].

4. Methods and materials

The following chapter includes content of the article “Geochemical observations within the water column at the CO₂-rich hydrothermal systems Hatoma Knoll and Yonaguni Knoll IV, in the southern Okinawa Trough”. The quoted sections and sentences are marked and contributions footnoted.

4.1. Investigation of the water column

The water column was investigated at both research sites at 27 stations between 7th and 22nd March 2008.

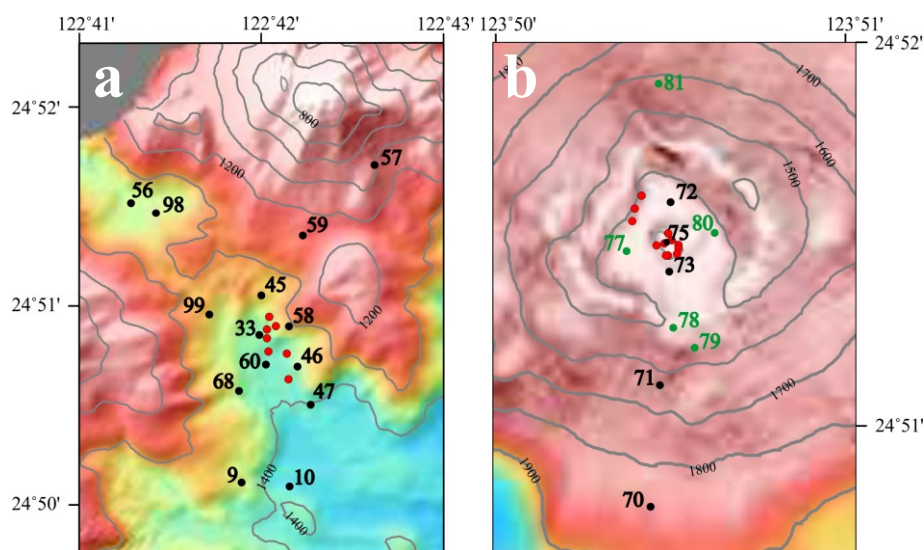


Fig. 6: Sampling stations in both research areas (a) YK and (b) HK. “Samples for He and C_T, and for C_T only, were taken at the black and green marked stations, respectively.” Red circles indicate the known hydrothermal vent sites.¹³

Fig. 6a shows the map of the YK research area, consisting of 14 water column stations. Most of them were located close to the known vent sites. In addition, stations in the northwestern and southern part of the valley and two stations at the slope of a northeastern seamount were surveyed.

“Seven sampling stations [at HK] were located inside the caldera or at its rim and four stations on a section extending outward from the outcrop of the caldera towards the south over a distance of approximately 0.5 nautical miles”¹⁴ (Fig. 6b).

¹³ Figures and caption are used in the article mentioned above. Processing of raw data provided by J. Schneider von Deimling. Construction and compilation of the figures was done by myself.

¹⁴ My contribution of the cited part included all writing, which was proof-read by the co-authors.

“For the determination of background values, representing the water column unaffected by local vent activity, two reference stations outside of the research areas were selected, both located in great distance to the respective research areas and in regions of relatively smooth bathymetry. Both reference sites were not in downstream direction of the prevailing currents. Station 69 (24° 50.597’ N, 122° 46.419’ E) is located about four nautical miles east of YK and station 76 (24° 53.998’ N, 123° 45.988’ E) almost five nautical miles northwest of the HK research area.”¹⁵

4.1.1. In situ measurements (CTD, pH, Eh, LADCP)

The implementation of measurements and on board data analysis described in this subchapter was made by a consortium of oceanographers and geochemists, mainly consisting of the co-authors and myself.

“Water samples were collected with a Sea-Bird Electronics SBE 32 water sampling rosette consisting of 22 Niskin bottles (10 L) and equipped with sensors for conductivity, temperature, and pressure (depth) (SBE 911plus underwater unit). The accuracy of the temperature and conductivity measurements was $\pm 0.001^{\circ}\text{C}$ and $\pm 0.0003 \text{ S} \cdot \text{m}^{-1}$, respectively. The pressure (depth) was recorded with an uncertainty of $\pm 0.01 \%$. Furthermore, the system hosted probes for oxygen (SBE 43), pH (SBE 18), and redox potential, Eh, (developed by Dr. K. Nakamura from the National Institute of Advanced Industrial Science and Technology (AIST), Japan; *Stranne et al.* [2010]), and a TRDI 300 kHz Workhorse lowered acoustic Doppler current profiler (LADCP) system”¹⁶ for direct current velocity measurements.

“LADCP raw data have been processed with an inverse method [*Visbeck, 2002*]. To distinguish between background flow and tidal variations in the measurements of the bottom currents, the TPXO global tidal model [*Egbert and Erofeeva, 2002*] has been employed. TPXO predicts the barotropic tidal currents and sea surface elevations at a given time and position by fitting the Laplace Tidal Equations to satellite measured

^{15, 16} My contribution of the cited part included all writing, which was proof-read by the co-authors.

sea surface height. [...] The model version TPXO7.2 (<http://volkov.oce.orst.edu/tides/>) with a $\frac{1}{4}$ degree spatial resolution [was used].”¹⁷

“Due to displacement by the strong currents of the Kuroshio and the tides [in the upper part of the water column of up to $1 \text{ m} \cdot \text{s}^{-1}$,] subpositioning of the water sampling rosette was used on most casts using the Posidonia 6000 USBL (ultra-short baseline) subpositioning system (IXSEA OCEANO SAS). The transponder was mounted on the wire about 10 m above the water sampling rosette and pinged its relative subsea position with a range accuracy of $\pm 0.5 \%$, resulting in an accuracy [of] $< 10 \text{ m}$ related to the DGPS ship position.”¹⁸ The subpositioning was also used to support the navigation of the research vessel to allow sampling at a precise position. The distance between the vessel and the CTD position during the cruise could occasionally account for almost half a nautical mile. Hence, it was essential to measure the exact position of the water sampling rosette. “CTD casts stopped about 10 m above the seafloor to avoid contact with elevated hydrothermal structures”¹⁹ and rocky faults.

The pH sensor is a pressure-compensated glass-electrode combined with a silver / silver chloride (Ag / AgCl) reference electrode which allows in-situ pH measurements. An electronic drift of the pH measurements was observed during the cruise. Hence, “an ex situ calibration with calculated pH determined by C_T and A_T of discrete samples was planned, but became impossible due to inconsistencies of the alkalinity results (see Chapter 4.1.3). Therefore, an offset correction was performed (similar to *Resing et al.* [2004], who applied this to discrete samples) by adjusting the pH profiles to a reference profile (averaged pH profile of both reference station pH water profiles, Fig. 11b) at the potential density level [referenced to 1500 dbar] of $\sigma_{1.5} = 33 \text{ kg} \cdot \text{m}^{-3}$ (Fig. 7). [...] This density [level] was chosen because [the] water in this depth (density) range is not influenced by CO_2 -rich plumes and also not affected by upper ocean variability.”²⁰ Thus the pH agrees with the pH at the reference

¹⁷ Writing of the cited part was done mainly by M. Walter, proof-read by me and the co-authors.

^{18 - 20} My contribution of the cited part included all writing, which was proof-read by the co-authors.

stations. It was “found at depths of 430 - 490 m at YK and 540 - 600 m at HK, respectively.”²¹ “Deviations in pH between offset-corrected profiles from the vent sites and the reference profile at densities greater than $\sigma_{1.5} = 33 \text{ kg} \cdot \text{m}^{-3}$ are interpreted as plume-induced pH deviations (ΔpH)”²² (Fig. 7).

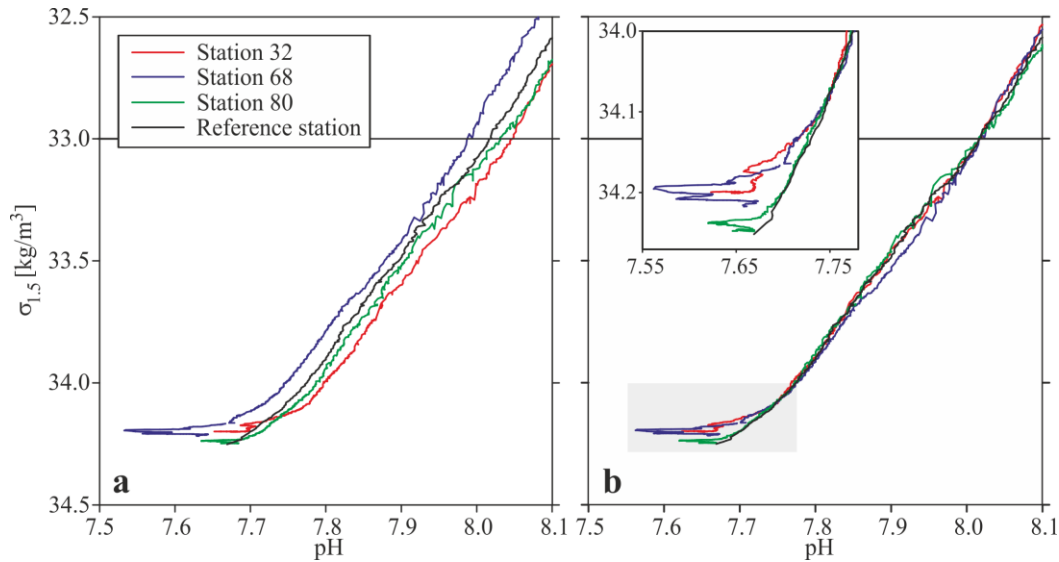


Fig. 7: “Adjustment of pH profiles to the reference profile (black) at the potential density ($\sigma_{1.5}$) of $33 \text{ kg} \cdot \text{m}^{-3}$ to correct for electronic drift during cruise: (a) measured and (b) adjusted pH profiles at different potential densities. The inset shows the adjusted pH values close to the bottom water. Note that the pH-profiles were not calibrated in a way which allows interpretation of the absolute pH-values.”²³

“In combination with pH measurements, anomalies of the redox potential (Eh) may indicate hydrothermal activity, if reduced constituents such as Fe^{2+} are emitted [Nakamura *et al.*, 2000]. Eh sensors measure the potential between a platinum (Pt) electrode and a silver / silver chloride (Ag / AgCl) reference electrode which arises from oxidation of reduced chemicals at the Pt electrode.”²⁴ Eh signals indicate on the age and degree of dilution of plumes [Baker *et al.*, 2005; 2006]. “Because of the relatively long response time and non-equilibration of the measuring system, the first derivative with respect to time, $d\text{Eh}/dt [\text{mV} \cdot \text{s}^{-1}]$, was used to identify plumes.”²⁵

Plume-associated temperature anomalies were derived from local deviations from the relationship between potential temperature and potential density which is undisturbed

^{21, 22, 24, 25} My contribution of the cited part included all writing, which was proof-read by the co-authors.

²³ These figures and caption are used in the article mentioned above. Data analysis, construction and compilation of data in the figures was done by myself.

by plume signals. Following interpretation “relies exclusively on sensor data from the upcast. Although the upcast is known to produce somewhat larger retarding and mixing artefacts than the downcast, this results in a better consistency [...] of sensor data and discrete water sample data, the latter being always gathered during the upcast. The water sampling rosette was heaved with a constant velocity of [about] $0.5 \text{ m} \cdot \text{s}^{-1}$ in the lower[most] (relevant) water column. Closing of the Niskin bottles was triggered during the continuous rise of the water sampling rosette without stopping to achieve best results of the sensor package although this procedure bears the risk of mixing processes with deeper water. [...] Closing of Niskin bottles ‘on the fly’, as well as the use of baseline-corrected, yet non-equilibrated pH-values from the pH-sensor likely lead to a smoothing of - and deviation from - the real in situ values. However [...] consideration of the results (Figs. 7, 16) suggests that [the] approach led to very consistent and interpretable use of pH-deviations (ΔpH) and $\Delta\text{pH-C}_T$ relation [Chapter 5.4], while not allowing interpretation of ‘absolute’ pH-values.”²⁶

4.1.2. Helium sampling and measurement

Sampling and measurements described in this subchapter were made by Ch. Mertens, and student assistants from the Institute for Environmental Physics at the University of Bremen and J. Sültenfuß, respectively.

“Helium sampling from Niskin bottles was carried out using copper tubes immediately filled and closed airtight with special stainless steel clamps after the water sampling unit was back on deck.”²⁷ 20 stations were sampled at both research areas, solely stations 77 to 81 at HK were omitted. “A total of 269 samples were collected and analyzed at the University of Bremen (Germany) using a measuring system consisting of a [multistage cryogenic] separation, fractionation and calibration unit, and quadrupole [for ^4He (among others)] and sector field mass spectrometers [for ^3He and ^4He measurement] [*Sültenfuß et al.*, 2009].

^{26,27} My contribution of the cited part included all writing, which was proof-read by the co-authors.

Helium isotope ratios of the samples ($R = {}^3\text{He}/{}^4\text{He}$) can be expressed as a multiple of the atmospheric ratio ($R_{\text{atm}} = (1.39 \pm 0.01) \cdot 10^{-6}$, *Lupton* [1983]) or as $\delta^3\text{He}$ following the equation: $\delta^3\text{He} = (R/R_{\text{atm}} - 1) \cdot 100$ according to *Craig et al.* [1975]. The enrichment of oceanic water with hydrothermal helium ($\text{He}^{\text{excess}}$ [$\mu\text{mol} \cdot \text{kg}^{-1}$]) is specified as the difference between the helium concentration (${}^3\text{He}$ or ${}^4\text{He}$) measured in the water sample and the concentration at equilibrium with atmospheric helium. Precision achieved by the measurement system is up to $\pm 0.4\%$ for the helium isotope ratio R and $\pm 0.8\%$ for helium concentrations.”²⁸

4.1.3. Total CO₂ and alkalinity sampling and measurement

Sampling and measurements described in this subchapter were made mainly by myself, S. Lage, and H. Kubsch (both from the Leibniz Institute for Baltic Sea Research Warnemünde).

Immediately after sampling for helium, 250 ml “glass ground flasks were filled with water for analysis of total CO₂ (C_T [$\mu\text{mol} \cdot \text{kg}^{-1}$], [or] dissolved inorganic carbon, DIC). After poisoning with 100 μl saturated mercury chloride solution (HgCl_2) the samples were stored cold and in the dark until analysis at the home laboratory. The measurements were carried out with the coulometric titration system SOMMA [*Johnson et al.*, 1985; 1987]. The measurement system was calibrated with carbon dioxide reference material provided by A. Dickson (University of California, San Diego) and yielded a precision / accuracy of $\pm 1.5 \mu\text{mol} \cdot \text{kg}^{-1}$ [*Dickson et al.*, 2007].

Total alkalinity, A_T , was measured by potentiometric titration with 0.1 M HCl using the VINDTA 3C analysis system (Marianda, Kiel, Germany). However, some of the vertical A_T profiles showed strong discontinuities which were not consistent with the pH and C_T distribution. [It was suspected] that this was caused by some unidentified technical problems during [laboratory] measurement[s]. [Hence], the A_T data were inappropriate for the detection of anomalies caused by emissions of hydrothermal

²⁸ My contribution of the cited part included all writing, which was proof-read by the co-authors.

vents or calibration of pH sensor data and were only used for calculations that are less sensitive to uncertainties in A_T (see Chapter 5.4).²⁹

4.2. Investigation of the rising condensed phases

Sampling, experiments, and measurements described in this chapter were made by myself and G. Rehder. Measurements of helium were made by J. Sültenfuß (Chapter 4.2.3.1) and stable carbon isotope ratio were made by M. Schmidt (Chapter 4.2.3.2).

At many former expeditions rising fluids have been sampled to determine gas content and composition of fluids from hydrothermal vents. Concentration of dissolved gases and volatiles were measured by vacuum degassing, headspace extraction or stripping of the sampled fluids [Ishibashi *et al.*, 1995; Merlivat *et al.*, 1987; Seewald *et al.*, 2002]. These methods were mainly used to investigate hot sources, but involved the risk of mixing with ambient seawater during sampling. “Sampling of the hot, gas-rich fluids from the center of HK and of hydrothermal fluids from YK was planned, but could not be executed [due to high water currents in the YK research area and] due to malfunction of the ROV 7-function manipulator arm during the second half of the expedition.”³⁰ Hence, only condensed phase at the low-temperature vents in the HK was collected (comparable with Konno *et al.* [2006] and Saegusa *et al.* [2006]).

4.2.1. Sampling of the condensed phase

Six samples of the condensed phases were collected at the HK during three dives of ROV ‘Quest 4000m’ from MARUM Center for Marine Environmental Sciences at the University of Bremen, Germany. Table 1 gives an overview of the locations and water depths. Three sampling stations were located at or close to the central mound, the residual at the northwestern rim of the caldera, close to the known low-temperature vents (Fig. 8). The Posidonia system allowed exact positioning of the ROV at the vents that was previously observed during earlier Japanese expeditions [Furushima and Yamamoto, 2015; Toki *et al.*, 2016; Watanabe, 2001].

^{29,30} My contribution of the cited part included all writing, which was proof-read by the co-authors.

Table 1: Overview of the sampled condensed phases, sampling depth, and measured inner pressure of the gassampler onboard.

Dive	GS	Number of stainless-steel subsampler	Location	depth [m]	pressure onboard [bar]
199	4	2	24°51.581' N 123°50.443' E	1524	~ 50
200	1	2	24°51.515' N 123°50.561' E	1492	80
	3	2	24°51.516' N 123°50.561' E	1492	164
202	4	4*	24°51.575' N 123°50.450' E	1526	115
	3	3	24°51.585' N 123°50.446' E	1524	84
	2	3	24°51.494' N 123°50.479' E	1474	~ 160

* 2nd fraction already discarded onboard

The ROV has more than five different video and photo cameras for both navigation of the vehicle and recording of overview or detail images of the investigated area from different perspectives. Almost all pictures within this study are made with the HDTV camera "Insite Zeus Plus Colorzoom" placed at the lowermost front of the ROV.

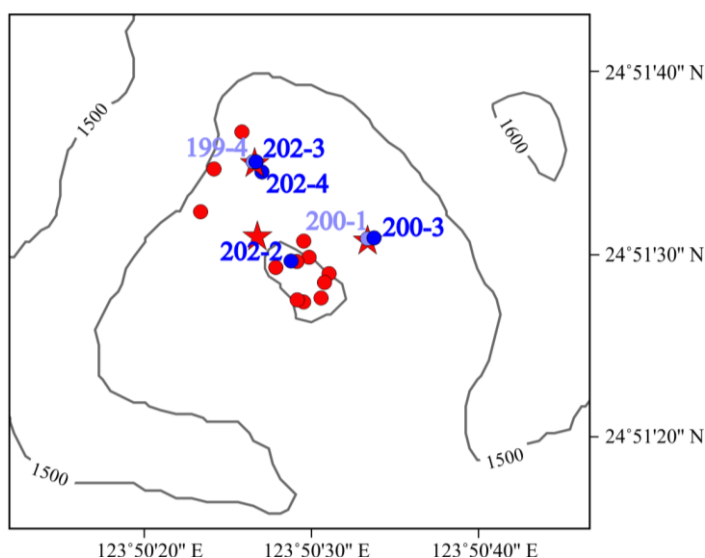


Fig. 8: Sampling stations of the condensed phases in the HK (blue circles). Known active hydrothermal vents are marked with red circles, known gas bubble sites with red stars [Furushima and Yamamoto, 2015; Toki et al., 2016; Watanabe, 2001].

“Sampling of the [...] condensed phases was performed by the use of [...] pressure-retaining gastight samplers [hereinafter referred to as gassampler or GS] consisting of a stainless steel tube (~ 62 ml inner volume) that can be closed by a ball valve with an inner diameter of 16 mm [Pape *et al.*, 2010].”³¹ The handling of the ball valve was carried out by the ROV.

The initial plan was to collect rising condensed phases in a funnel in front of the closed ball valve until a sufficient gas volume was reached (partly visible in Appendix IIIa). Opening of the valve should allow sampled gas to flow into the pre-evacuated GS. First tests (dive 199, GS 4 and dive 200, GS 1) showed that GH skins formed around the bubbles already in the funnel during sampling, due to temperature and pressure conditions. These solid GH prevented transfer of the gas into the GS almost completely. Therefore, subsequent sampling (since dive 200, GS 3) was carried out by direct sampling of the rising condensed phases through the open valve (Appendix IIIb). “The GS was positioned vertically [in a way] that rising bubbles and droplets could flow directly into the open GS [for capturing]. After complete filling [of the tube (7 to 13 minutes)], the ball valve was closed”³² and the sampler stored inside the front porch of the ROV.

4.2.2. First processing onboard

Onboard, all GS were connected with a pressure gauge, showing an inner pressure of 50 to 164 bar. For all GS from dive 202 the response of the pressure inside the GS on temperature change was studied by slow heating from 0 to 25°C (‘p/T-expansion experiment’).

For further investigations up to 6 subsamples (‘fractions’) were gained from each GS, however some of them were already discarded onboard, like the second fraction from dive 202, GS 4. The fractions were obtained by two different methods (Appendix IV). On the one hand the sample was transferred in a gas-tight Hamilton syringe for measurement onboard. Due to leakage problems during the cruise and non-constancy

^{31,32} My contribution of the cited part included all writing, which was proof-read by the co-authors.

of the calibration gas measurement, most measured concentrations onboard were not reliable and trustworthy, especially between the different measuring days. Relative standard deviations over the measurement time period of 9 days was between about 1.4 % for CO, C₂, and C₃ up to 4.4 % for CO₂ and 6.5 % for CH₄. Hence, these results are not used in this study. On the other hand the sample was transferred from the GS into a pre-evacuated subsampler – stainless steel tubes with inner volumes of 5.5 ml, sealable with two gastight and pressure-retaining spindle valves. Only the measurement results of these subsamplers are used in this study.

Last fractions were obtained by release of pressure (dive 200, GS 3) or expansion of the gas into a pre-evacuated high-volume vessel (dive 202, GS 4, 3, and 2).

4.2.3. Measurements in the laboratory

A total of 15 subsamplers were obtained from the six condensed phases (Table 1). These fractions were investigated for gas composition, helium isotopic and concentration signature, and carbon isotope composition. These parameters were measured between 6 and 7 years after sampling. During this period of time the subsamplers were stored cold and nearly free of movement. Pressure loss ranged between 5 and 60 bar, which is a decrease of 3 to 92 % compared to the initial pressure, the median loss being 18 %. Almost all subsamplers contained enough residual pressure to determine all of the geochemical parameters. However, for a few of them only one or two parameters could be measured, due to their very low pressure (e.g. dive 202, GS 3, fractions 2 and 4). Appendix IV gives an overview which parameters were obtained for each subsample.

In case of sufficient pressure for multi-parameter determination or especially for high pressure subsamples, the condensed phase in the subsamplers was transferred contamination-free into further stainless-steel subsamplers or tubes which have been flushed with nitrogen and evacuated repeatedly before. This approach ensured both the measurement of a homogenous sample, and it prevented the injection and

measurement systems from damage, which were thought to withstand a maximum pressure of approximately 2 bar.

4.2.3.1. Helium measurement

Determinations of helium concentration and helium isotopic ratio were performed with the cryogenic mass spectrometer-based measurement system at the University of Bremen, as mentioned in Chapter 4.1.2. The subsamplers were connected to the injection unit via Swagelok fittings and the gaseous phase was transferred into a glass ampule from where the sample was injected automatically into the measurement system under vacuum.

4.2.3.2. Determination of stable carbon isotope ratio

Subsamplers with an inner pressure of up to 2 bar were sent to the GEOMAR Helmholtz Centre for Ocean Research (Kiel) to determine $\delta^{13}\text{C}$ isotope ratio of methane and carbon dioxide. Gaseous phase was transferred into head space vials and measured as described in *Vielstädte et al.* [2015].

Table 2: Measurement range of the used gas chromatography system, covered by available calibration gases.

	PDD	TCD
CH ₄	< 1 mole-%	> 100 ppm
CO ₂	not measurable	> 100 ppm
H ₂ S	not measurable	> 8,000 ppm*
O ₂	< 5 mole-%	not separated
Ar	< 2 mole-%	
N ₂	< 2 mole-%	> 2 mole-%
CO	< 5 mole-%	not measurable
H ₂	< 4 mole-%	not measurable
C ₂ H ₆	< 2,5 mole-%	> 100 ppm
C ₂ H ₄	not measurable	> 1,500 ppm*
N ₂ O	not measurable	> 200 ppm

* Due to the small number of low-concentrated calibration gases, linearity of the calibration line is ensured only above this concentration, but likely applies already below.

4.2.3.3. Determination of gas composition

Determination of the gas composition was performed via gas chromatography at the Leibniz Institute for Baltic Sea Research (IOW, Germany). The measurement system consisted of a manometric dosing and injection system and two parallel analytical lines within the gas chromatograph (GC; Trace Ultra, Thermo Scientific). The carrier gas was helium 5.0 extra purified under usage of a heated helium purifier (VICI Valco Instruments) to remove residual nitrogen.

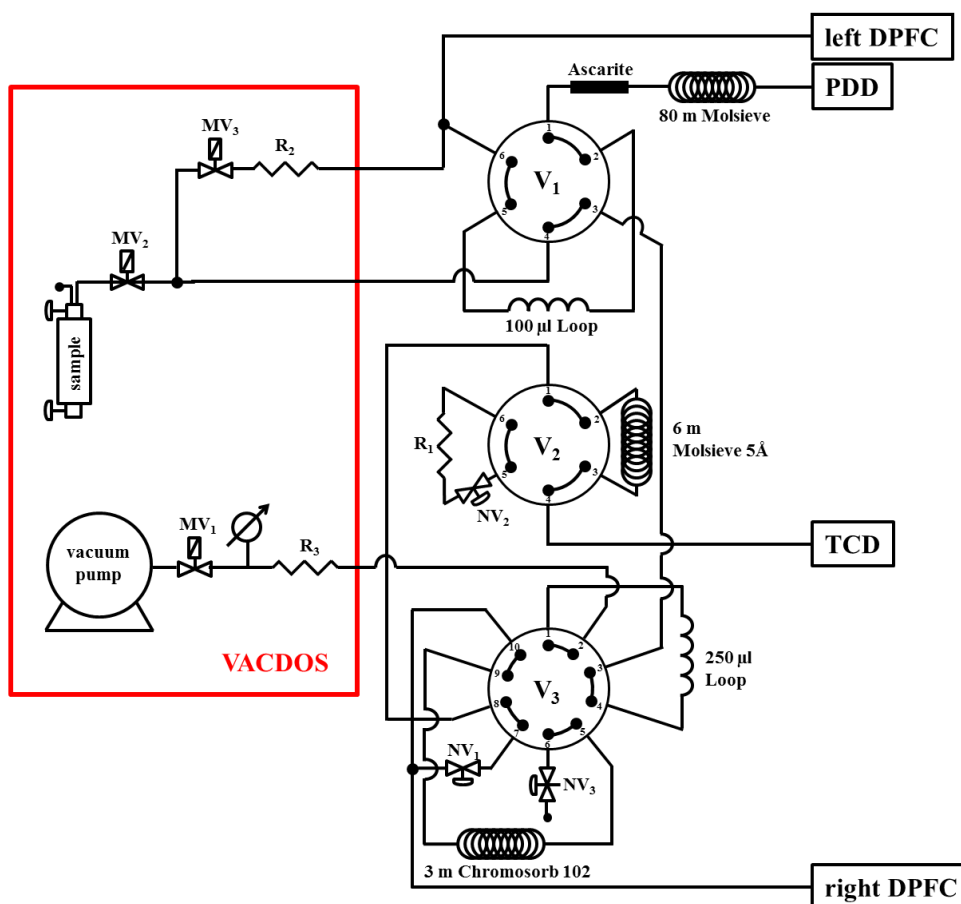


Fig. 9: Gas chromatographic measurement system with the manometric dosing and injection system VACDOS (red framed) and the two analytical lines. MV: magnetic valve (Parker), NV: needle valve (Swagelok, Fisons), V: variable ports 2-position valve (VICI Valco), R: resistor, DPFC: GC-injector (digital pressure and flow controller), PDD: pulse-discharge detector, TCD: thermal conductivity detector

The setup enabled the determination of a large number of gases both qualitatively and quantitatively within a wide mole fraction range of a few ppm up to 100 mole-% (Table 2). Fig. 9 shows a schematic illustration of the used gas chromatography

measurement system. Injection of the sample from the subsampler was performed using the manometric dosing system 'VACDOS' (S+H-Analytik, Mönchengladbach, Germany). The system consisted of three magnetic valves (Parker), a high-precision pressure sensor (SensorTechnics), and a vacuum pump (Edwards). Usage of a very precise pressure sensor allowed filling of the sample loops with pressure different from the standard pressure, both over and negative pressure of down to 50 mbar. These units and the data record from the pressure sensor was controlled by a National Instruments controlling and monitoring system and inherent user-interface software. After the subsampler was connected to the system via Swagelok fittings, the entire injection system was first flushed with carrier gas and then in case of sufficient pressure within the subsampler with sample gas, and evacuated repeatedly. This process enabled measurements of the gas components N₂, O₂, and Ar at low concentration ranges. Measured oxygen concentrations in the samples were in the range of blanks and O₂-free standard gas measurements (N₂: 0.2 - 0.6 mole-%, O₂: 48 - 512 ppm, Ar: 1 - 64 ppm). These low levels not only confirm the procedure used, but furthermore exclude contamination with air during handling, subsampling and storage of the subsamplers.

For calibration, sample loops were filled daily with different standard gas mixtures (Deuste Steiniger) and pressures. Calibration lines with $R^2 > 0.98$ were calculated. Because all samples were thought to contain huge amounts of hydrogen sulphide, the sample loops, as well as almost all further connection tubes, were made of sulfinert material to avoid absorption processes on the common stainless steel tubes.

The sample reaches the first analytical line connected to the pulse-discharge detector (PDD) via a 100 µl sample loop. Then the valve V₁ is switched and the gas is transferred to an Ascarite trap to remove H₂S from the gas sample. This process protects the separation column from hydrogen sulfide and sulphurous acid that arise due to the reaction with water. The subsequent MolSieve capillary separation column (Thermo Scientific, TG-Bond MSieve 5A, 50 + 30 m x 0.53 mm x 50 µm) is located in the GC oven. This analytical line permits measurements of the gas components N₂,

CO, H₂, and hydrocarbons CH₄ and C₂H₆ in a low-concentration range of up to 1 to 5 mole-%. Supernormal length and material of the used column enables the separation of oxygen and argon at an isotherm temperature of 40°C. Measurements of gases with strong interactions with the zeolite-stationary phase (CO₂, N₂O, and hydrocarbons > C₂) however fail with this arrangement.

High gas concentrations can be measured by the second analytical line, consisting of a 250 µl sample loop, two different separation columns, and a thermal conductivity detector (TCD). For pre-separation, a gas sample is first transported to a packed stripping column (Chromosorb 102, 3 m x 1/8''). The air components H₂, O₂, Ar, and N₂, as well as CH₄ and CO cannot be separated by this column. Hence, they have to be transferred by time controlled switching of valves V₂ and V₃ to a second packed column (MolSieve 5Å, 6 m x 1/8''), where they get separated under isotherm temperature conditions (40°C). Remaining gases like carbon dioxide, nitrous oxide, ethylene, ethane, and H₂S are separated already by the first stripping column and do not need to be transferred to the MolSieve column. They are temporarily held back during the second separation step of the other components and reach the detector without further separation steps by switching back the valve V₃. Due to the elevated number of separation columns and frequent switching operations of valves V₂ and V₃ during measurements, several gas components cannot be measured with this second analytical line. Strong adsorption by porous polymers in the first and second stripping column at 40°C avoids measurement of hydrocarbons with chain lengths longer than two carbon atoms and CO, respectively. Due to the shortness of the MolSieve column, oxygen and argon cannot be separated and are measured as one signal. The current settings at the GC additionally avoid the determination of H₂. This is because the gas and pressure surge caused by switching of valve V₂ reach the detector at almost the same time and prevent a proper integration of the H₂ peak in the chromatogram.

Since it was known beforehand, that the samplers from dive 199, GS 4 and dive 200, GS 1 contained water, due to the way of sampling, they were used for testing purposes of the measurement system. During partition, the subsampler was held upright to

prevent transfer of water into the new subsampler. During filling of the sample loops the subsamplers were depressurized only to a limited extent to avoid water contamination and discharge. Nonetheless, the results of both samplers were discarded because measurement results might be falsified. Hence, only the residual four samples will be discussed later on.

4.2.4. Further experiments during the dives

The rise of the condensed phases was investigated using the so called ‘bubble imaging box’ (short: bubble box). The device was constructed at the IOW by the internal machine shop, basically following the design of a device used at the Monterey Bay Aquarium Research Institute, Moss Landing, USA (MBARI). The box has an inner dimension of 30 · 100 · 25 cm (W · H · D) and is open at the top and bottom. The front and sidewalls of the box are made of transparent polycarbonate, the backwall is a white, opaque plastic plate. The latter acted as a diffuser for the backlight, generated by an array of deep-sea rated LED diodes which are powered by a Li-Ion Power Pack (both manufactured by CONTROS Systems and Solutions GmbH, Kiel).

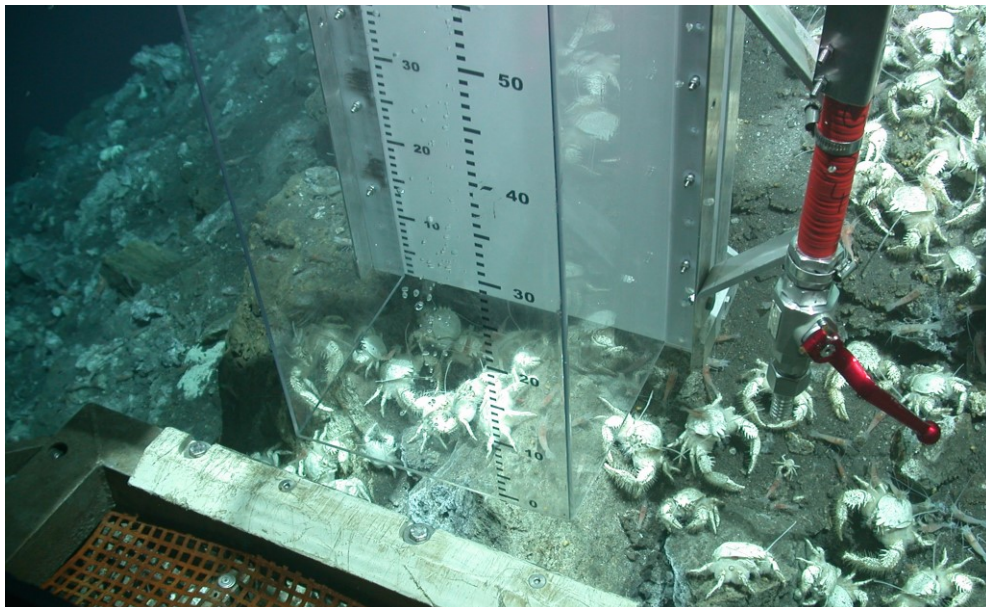


Fig. 10: Condensed phases ‘collected’ with the bubble box that is positioned above a hydrothermal vent during dive 205. Due to malfunction of the ROV 7-function manipulator arm during the second half of the expedition the GS was fixed at the arm of the bubble box.

The bubble box was positioned on the porch of the ROV or in such a way that the HDTV camera of the ROV focused on the inner most lighted part of the box, fitted with two graduated scales both at the front and the backwall (Fig. 10). During the bubble box experiments one of these scales was always in view of the camera to estimate the size of droplets. The device enabled the determination of a ‘collected’ condensed phase. However, the absence of a second, downward looking camera prohibits a parallax correction for the distance between the front- and backwall, as reported by *Brewer et al.* [2002], hence a precise size determination of the condensed phases. The device enabled the determination of a ‘collected’ condensed phase. Also, the ascent of the ROV by adjusted vertical velocity of the rising bubbles allowed monitoring of a condensed phase after emission during the rise through the water column. The box was dimensioned in such a way that the bubbles are allowed to fly vertically and almost undisturbed through the box without restricting effects of lateral movement by the sidewalls.

During dives 199, 200, and 202 a further self-constructed device was used to investigate the characteristics of a condensed phase created by Dr. K.-i. Nakamura from the National Institute of Advanced Industrial Science and Technology (AIST), Japan. The so called ‘T-corer’ was used in different versions because of damage and combined a transparent collection device, which was open at the bottom and closed at the top, with an integrated lance for temperature record inside the device (with 5 temperature probes distributed along the lance) and of the ambient seawater. During filling with condensed phase the ‘T-corer’ was held by the manipulator arm of the ROV in such a way that the HDTV camera focused on it.

4.3. Phase Calculations

Determination of data described in this subchapter was supported by Dr. Gregor Rehder and Dr. Edward Peltzer (Monterey Bay Aquarium Research Institute).

The Infochem Multiflash software calculates thermophysical behavior and properties of pure gases or gas mixtures of each phase (gas, liquid, solid, GH) based on

multiphase equilibrium calculations [Tummescheit and Eborn, 2002]. The software has been used for example for calculations of dissolution rates of GH and droplets in seawater [Brewer et al., 2002; Rehder et al., 2004]. A large number of physical property data banks as well as several thermodynamic mathematical models are available in this advanced software package. One of these models bases on the Redlich-Kwong-Soave equation of state.

The Redlich-Kwong equation derives from the van der Waals equation and aims at the enhancement of the equation of state for real gases

$$p = \frac{RT}{V_m - b} - \frac{a}{\sqrt{T}V_m(V_m + b)} \quad (1)$$

with p as pressure, R as the universal gas constant, T as temperature, and V_m as the molar volume. The parameters a and b represent the cohesion pressure and co-volume, respectively, and comprise the temperature and pressure at the critical point. Hence, both parameters represent the conditions at which a phase boundary ceases to exist. The Soave modification extends the Redlich-Kwong equation by the parameter α to incorporate the divergence of a molecule from the ideal spherical shape

$$p = \frac{RT}{V_m - b} - \frac{\alpha \cdot a}{V_m(V_m + b)} \quad (2)$$

Several parameters of condensed phases of different gas composition at various pressure and temperature conditions were simulated for this study using the advanced Redlich-Kwong-Soave model which includes further non-standard features like density correction for light gases, fitting of vapor pressure curves and mixing rules for highly non-ideal systems.

On the basis of the measured gas composition and emission depth of the condensed phases, the development of density and viscosity were simulated over a large temperature range between 100 and 0°C. The Multiflash software allows for multiphase equilibrium calculations between gaseous, liquid, solid phases, and GH. The phase stability analysis procedure determines which phase is likely present at equilibrium. Hence, also the dew and bubble point for gas mixtures and the boiling point for pure gases were calculated using this model. These phase transformation

calculations were performed for condensed phases of various gas compositions both on the basis of results from the GS and various ratios of the four main compounds carbon dioxide, methane, nitrogen, and hydrogen sulfide. The dew and bubble points are calculated for an individual range of temperature, with maximum values of 30°C and -83°C.

A combined hydrate model allows for the determination of properties at the phase boundary to GH. The model bases on the Redlich-Kwong-Soave equation and “consists of lattice parameters for the empty hydrate and parameters for the interaction of gas molecules with water in the hydrate” [Infochem, 2014]. The model is adjusted by binary interaction parameters (BIPs) describing the cross forces associated by the polar components of the gas hydrate.

The pressure at which GH formation occurs as well as the composition of GH depending on variable initial gas composition was calculated. The GH phase boundary was determined within a temperature range of 4 to 14°C for gas mixtures of gas composition of the condensed phase and between 0 and 15°C for fixed gas mixtures of carbon dioxide and methane with variable amounts of nitrogen or hydrogen sulfide. Both temperature ranges were chosen to calculate the composition of the initially formed GH, too. 0.01 mol of water needed to be added virtually to the gas mixture as a prerequisite of hydrate formation.

5. Geochemical observations within the water column at HK and YK

The following chapter includes content of the article “Geochemical observations within the water column at the CO₂-rich hydrothermal systems Hatoma Knoll and Yonaguni Knoll IV, in the southern Okinawa Trough”. The quoted sections and sentences are marked and contributions footnoted.

5.1. Reference stations

“Plots of temperature, salinity, and potential density show great uniformity of both reference stations 69 and 76 for water depths greater than about 900 m (Fig. 11a). At shallower water depths both profiles tend to diverge. Since the impact of the plume is restricted to the lower part of the water column, [...] an averaged reference profile of both reference stations [has been calculated]. The vertical distributions of C_T, pH, and ³He^{excess} are shown as a function of the potential density in Fig. 11b. To characterize the effect of the vents on the helium distribution, [...] ³He^{excess} [is used] instead of the frequently used δ³He notation, because ³He^{excess} refers to concentration units, which are thus more directly comparable with the presentation of C_T. The difference between the C_T at the reference station and at any other station at the same potential density is considered to represent the amount of C_T resulting from plume emissions (ΔC_T). In order to obtain reference C_T for the densities at the different sampling depths, a continuous function C_T(σ_{1.5}) was derived by fitting an exponential function to the C_T/σ_{1.5} data from both reference stations (R² = 0.99; Fig. 11b). Since the difference between C_T at the two reference stations was negligible, the data of both stations were pooled to calculate a single function C_T(σ_{1.5}) (Fig. 11b).

³He^{excess} differed significantly from zero especially in the deep water of the reference station, with maximum values of 1.3 μmol · kg⁻¹ (max. δ³He = 32.8 ‰). Enrichment of ³He in deep Pacific waters relative to the atmosphere has already been reported by e.g. Clarke *et al.* [1969]. [Probably the] elevated concentration is the result of a steady flux from the mantle into the water column [Lupton and Craig, 1975]. δ³He background

values of up to 20 % for the Pacific Ocean [Talley, 2007] and up to 39.3 % for the Lau BAB [German et al., 2006] indicate local variability of these values.”³³

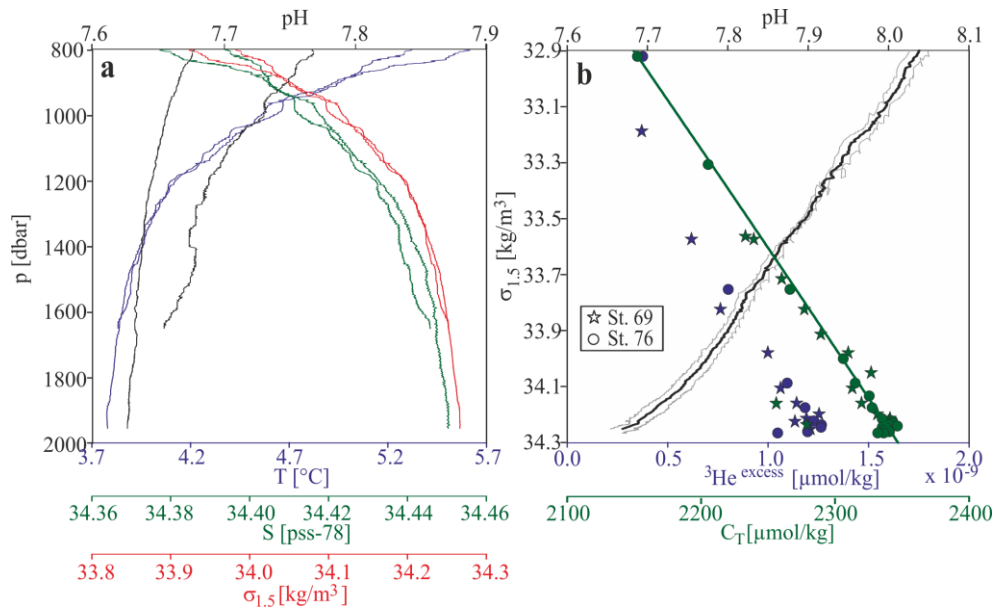


Fig. 11: “Vertical distribution of (a) pH (black), temperature (blue), salinity (green), and potential density (red) versus depth and (b) C_T (green), pH (grey), and $^3\text{He}^{\text{excess}}$ (blue) versus potential density at the reference stations 69 (stars) and 76 (circles). The solid green line in Figure b shows the exponential fit to the C_T data, the solid black line the mean pH profile. Note that the pH-profiles were not calibrated in a way which allows interpretation of the absolute pH values.”³⁴

5.2. Distribution of vent-induced anomalies

“The vertical ΔC_T , $^3\text{He}^{\text{excess}}$, and ΔpH distributions at almost all stations indicate anomalies with respect to the reference stations that are attributed to the influence of vent fluids. Fig. 12 shows water column profiles of three selected stations at YK and HK with different characteristics of these anomaly patterns.”³⁵ The anomalies at these stations do not show a continuous gradient, but are characterized by peaks at different water depths. “Not only the magnitude, but also the number of the peaks differs between the analyzed stations. Station 73 shows only one peak anomaly in about 130 m height above the seafloor, whereas the high-resolution pH and Eh sensor data from station 75 indicate four more or less pronounced minima in the lowermost 100 m (Fig. 12). In most cases the anomaly peaks of C_T , $^3\text{He}^{\text{excess}}$, ΔpH , and $d\text{Eh}/dt$ coincide

^{33, 35} My contribution of the cited part included all writing, which was proof-read by the co-authors.

³⁴ These figures and caption are used in the article mentioned above. Data analysis, construction and compilation of data in the figures was done by myself.

and thus confirm the suitability of these variables to identify the effect of hydrothermal vents on the water column chemistry.”³⁶ At almost all stations the Eh sensor records plume signals up to 10 m (equivalent to 10 seconds) earlier than the pH sensor (e.g. station 73 and 75, Fig. 12). The reason for this shift is not clear. At least, consistency of ΔC_T and ΔpH signals within the water columns indicate that the pH sensor does not have a significantly slower response time compared to the Eh sensor.

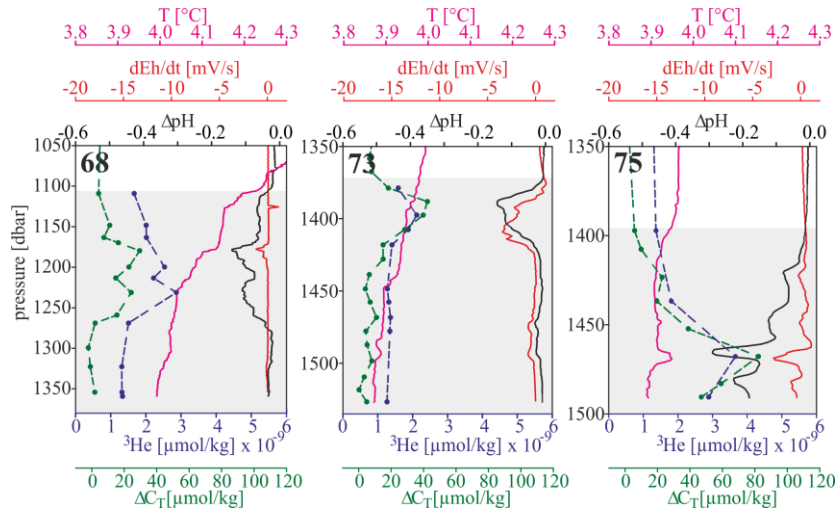


Fig. 12: “Plume-affected lowermost water column data of one station from YK (68) and two stations from HK (73 and 75); ΔC_T (green), ${}^3\text{He}^{\text{excess}}$ (blue), ΔpH (black), dEh/dt (red), and T (pink).”³⁷

“A summary of the peak ΔC_T , ${}^3\text{He}^{\text{excess}}$, and ΔpH and the corresponding water depth at the YK and HK research areas is given in Table 3. The stated distance from the seafloor is based on the approximation that the CTD cast stopped 10 m above the seafloor. The variability in the number and magnitude of anomaly peaks and their respective heights in the water column indicates temporal variations of vent flux intensity and the existence of different vent sites in close proximity [*Gamo et al.*, 2010]. A definite allocation of these anomalies to individual vents is impossible due to the large number of vent sites and water current-induced dissolution and distribution of the vented fluids.

Aside from the temporal variation of the sources, the height and dispersal of the anomalies in the water column at YK and at HK is further controlled by the interplay

³⁶ My contribution of the cited part included all writing, which was proof-read by the co-authors.

³⁷ These figures and caption are used in the article mentioned above. Data analysis, construction and compilation of data in the figures was done by myself.

between the flow field and the local bathymetry, which was found to differ significantly between the two research areas. At HK, the background flow within the caldera is restricted by the sidewalls and in the order of $0.1 \text{ m} \cdot \text{s}^{-1}$ [Furushima and Yamamoto, 2015], with no preferred direction. [...] Model predictions from TPXO7.2 indicate that tides are weak at this site, with amplitudes of less than $2 \text{ cm} \cdot \text{s}^{-1}$ of tidal flow (Appendix II). The absence of advective currents leads to a mostly unimpaired rise of the buoyant plumes within the caldera and [to a] reduced spreading of the hydrothermal signal.

In contrast, the open valley-like structure of the bathymetry at YK allows for variable, strong background currents of typically 0.2 to $0.3 \text{ m} \cdot \text{s}^{-1}$ close to the seafloor and up to $1.2 \text{ m} \cdot \text{s}^{-1}$ of the upper 500 m of the water column, which are strongest in along valley (NE to SW) direction [Nakamura *et al.*, 2008]. Further, the tidal forcing is stronger at YK. The predicted currents during the time of observation are of the order of 5 to $10 \text{ cm} \cdot \text{s}^{-1}$ (Appendix II), alternating in north-south direction.”³⁸

This leads on the one hand to a non-uniform horizontal dispersal of the buoyant and non-buoyant plume. On the other hand, variable and strong currents that interact with the rough topography are prone to excite internal waves. This process displaces the plume in the vertical and leads to diapycnal mixing, that distributes the hydrothermal fluids over a larger depth range in the water column [Walter *et al.*, 2010]. “Background flow affects the rise height of a hydrothermal plume insofar as stronger flow leads to plume bending and a reduced rise height [Lavelle *et al.*, 2013; Tao *et al.*, 2013]. A time-variable ocean current as observed at YK will therefore result in an equally variable rise height, and thus can account for the observed variability in the plume signals. Greatest heights [...] where geochemical parameters show peak anomalies are 260 m at YK (station 68) and 250 m at HK research area (station 81).”³⁹

³⁸ Writing of the cited part was done mainly by M. Walter. Me and the co-authors contributed by proof-reading.

³⁹ Writing of the cited part was done by myself and M. Walter. The co-authors contributed by proof-reading.

Table 3: “Maximum values of ΔC_T , ${}^3\text{He}^{\text{excess}}$, and ΔpH for all stations at YK and HK together with the depth of the peaks and approximate height over ground.”⁴⁰
 “For some stations the maximum of ΔC_T , ${}^3\text{He}^{\text{excess}}$, and ΔpH were not found at the same depths. In this case, more than one water depth is listed for the same station.”⁴¹

Station number	Research area	Maximum values for			Peak anomaly in	
		ΔC_T [$\mu\text{mol} \cdot \text{kg}^{-1}$]	${}^3\text{He}^{\text{excess}}$ [$\mu\text{mol} \cdot \text{kg}^{-1}$]	ΔpH	Water depth [dbar]	Height from ground [dbar]
9	YK	11.4	$1.6 \cdot 10^{-9}$	-0.05	1,355	10
10	YK	7.0			1,368	58
			$1.6 \cdot 10^{-9}$	-0.04	1,328	98
33	YK		$2.6 \cdot 10^{-9}$	-0.09	1,361	30
		28.3			1,311	80
45	YK		$2.5 \cdot 10^{-9}$	-0.10	1,315	14
		33.1	no value		1,277	52
46	YK			-0.70	1,375	0
		37.4	$2.9 \cdot 10^{-9}$	-0.14	1,275	110
47	YK	13.5		-0.80	1,406	0
			$1.8 \cdot 10^{-9}$		1,240	176
56	YK	13.2	no value	-0.06	1,222	156
			$1.7 \cdot 10^{-9}$		1,198	180
57	YK	19.1	no value		1,089	22
			$2.3 \cdot 10^{-9}$	-0.07	1,067	44
58	YK	10.8			1,273	56
			$1.5 \cdot 10^{-9}$	-0.03	1,149	180
59	YK		$2.1 \cdot 10^{-9}$	-0.06	1,252	10
		1.3			1,097	165
60	YK	13.1	$1.8 \cdot 10^{-9}$	-0.05	1,391	10
68	YK		$2.9 \cdot 10^{-9}$		1,231	139
		32.7	no value	-0.14	1,180	190
70	HK	3.0	$1.2 \cdot 10^{-9}$	-0.01	1,851	10
71	HK	10.0	$1.3 \cdot 10^{-9}$	-0.02	1,497	145
72	HK	36.3	no value	-0.14	1,457	87
			$2.2 \cdot 10^{-9}$		1,449	95
73	HK		$2.1 \cdot 10^{-9}$		1,398	139
		42.1	no value	-0.15	1,388	149
74	HK	12.3	$1.4 \cdot 10^{-9}$	-0.01	1,377	90
75	HK	83.3	$3.7 \cdot 10^{-9}$	-0.24	1,468	33
77	HK	24.0	no value	-0.08	1,499	43
78	HK	30.8	no value	-0.08	1,482	32
79	HK	10.7	no value		1,569	10
			no value	-0.03	1,448	131
80	HK	19.0	no value	-0.06	1,362	174
81	HK	15.4	no value	-0.06	1,417	171
98	YK	20.9	$2.0 \cdot 10^{-9}$	-0.08	1,361	10
99	YK	17.3		-0.07	1,296	39
			$2.5 \cdot 10^{-9}$		1,248	87

^{40, 41} The table and caption are used in the article mentioned above. Data analysis and compilation of data in the table was done by myself.

5.3. ${}^3\text{He}^{\text{excess}}$, ΔC_T and their relationship

Different tracers can be used to detect hydrothermal vents. One of them is the inert noble gas helium with its two stable isotopes, ${}^3\text{He}$ and ${}^4\text{He}$, that have primordial and radioactive origin, respectively. The helium is stored in the earth mantle since the formation of the earth. Hydrothermal fluids get enriched with helium during their rise through the earth's crust [Craig *et al.*, 1975]. After release into the water column the inert helium does not degrade by chemical reaction, but is mixed conservatively with ambient water and transported by currents [Craig *et al.*, 1975]. Concentrations and isotopic ratios of the helium isotopes can be used to identify the sources of rising fluids at hydrothermal vents [Lupton *et al.*, 1980].

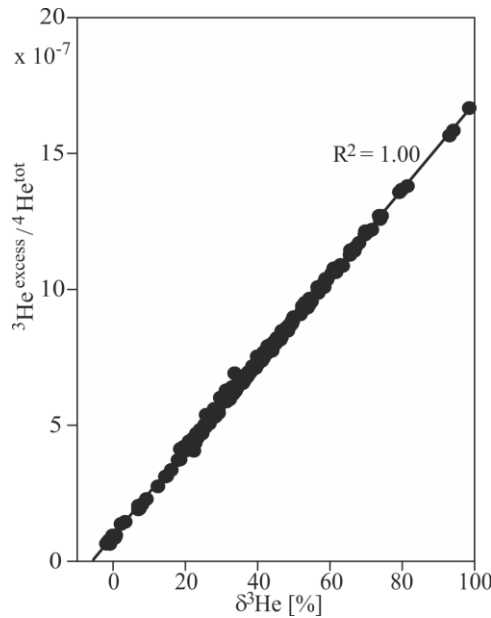


Fig. 13: “Linear correlation between ${}^3\text{He}^{\text{excess}} / {}^4\text{He}^{\text{tot}}$ and helium isotope ratio $\delta^3\text{He}$ for 267 samples. Two samples have been deleted from the data set due to obvious contamination with air and degassing [...]. The [...] regression line was calculated with a SMA analysis in R (package “lmodel2”, $n_{\text{perm}} = 99$).”⁴²

“The helium samples were used to calculate both ${}^3\text{He}^{\text{excess}}$ and $\delta^3\text{He}$. The relationship between these variables is given by the equation

$$\delta^3\text{He} = \frac{{}^3\text{He}^{\text{excess}}}{{}^4\text{He}^{\text{tot}}} \cdot \left(\frac{1}{R_{\text{atm}}} - \frac{1}{R_{\text{vent}}} \right) \cdot 100 \quad (3)$$

⁴² This figure and caption are used in the article mentioned above. Data analysis, construction and compilation of data in the figure was done by myself.

with ${}^4\text{He}^{\text{tot}}$ as total measured ${}^4\text{He}$ concentration and R_{vent} as ${}^3\text{He}/{}^4\text{He}$ ratio of vent plumes [derivation of this equation in Appendix I]. A distinct linear relationship exists between ${}^3\text{He}^{\text{excess}} / {}^4\text{He}^{\text{tot}}$ and $\delta^3\text{He}$ ($R^2 = 1.00$; Fig. 13). This indicates that the helium concentrations in the observed vent plumes are characterized by a uniform R_{vent} . Based on R_{atm} of $1.39 \cdot 10^{-6}$ [Lupton, 1983] the slope of the regression line in Fig. 13 yields a mean R_{vent} of $1.0 \cdot 10^{-5}$, which is thus about 7.5 times larger than R_{atm} . This ratio is within the range of MOR basalts (MORBs) and MOR lavas ($8 \pm 1 R_{\text{atm}}$), which indicates dominance of primordial helium (${}^3\text{He}$) from the upper mantle. R_{vent} of BAB basalts are typically in the same range or higher than MORBs [Lupton *et al.*, 2009], but fluids at arc or back-arc systems show lower R_{vent} [Ishibashi *et al.*, 1995; Lupton *et al.*, 2006; Resing *et al.*, 2009] induced by radiogenic helium (${}^4\text{He}$) from the subducted oceanic plate.

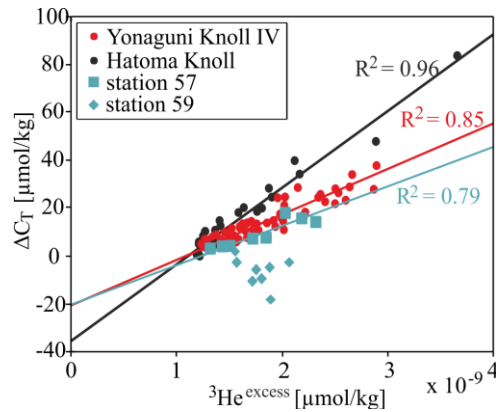


Fig. 14: “Plot of ΔC_T against ${}^3\text{He}^{\text{excess}}$ concentrations for all samples from the HK and YK research areas. Data points from stations 57 and 59 [...] are presented separately. Solid red, black, and blue lines are the linear [...] regression lines for the data points from YK, HK, and station 57, respectively (calculated with a SMA analysis in R; package “lmodel2”, $n_{\text{perm}} = 99$). $\Delta C_T/{}^3\text{He}$ ratios of the dominating fluids are derived from the slope of the regression lines.”⁴³

While the range of ΔC_T and ${}^3\text{He}^{\text{excess}}$ values of samples from the two [research sites] is almost identical (Fig. 14), the slope of the trend lines show that HK vent fluids are characterized by a higher $\Delta C_T/{}^3\text{He}$ signature ($3.2 \cdot 10^{10}$) than those at YK ($1.9 \cdot 10^{10}$), by a factor of about 1.7. Dominating fluids at HK clearly exceed $\Delta C_T/{}^3\text{He}^{\text{excess}}$ ratios from MORs Axial Volcano and Southern East Pacific Rise (SEPR) by a factor of 15

⁴³ This figure and caption are used in the article mentioned above. Data analysis, construction and compilation of data in the figure was done by myself.

[Resing *et al.*, 2004] due to the fact that carbonate-rich sediments from the subducted plate [influence] the composition of fluids during the formation process within the rock. [...] The slope of HK data is even higher (up to factor of about 10) than for most sampled high active areas at the Mariana Arc, and comparable to the trend observed at the Seamount X in the [...] Mariana Arc. Only for the volcano Ruby, fluids with a $\Delta C_T/{}^3\text{He}$ ratio higher by a factor of about 1.7 [Resing *et al.*, 2009] have been reported. Scatter of data from YK ($R^2 = 0.85$, Fig. 14) is slightly higher than from HK ($R^2 = 0.96$). A possible reason is the existence of various larger vents within the research area that might differ in their gas composition.”⁴⁴ The plumes distribute over a wide distance due to the strong and variable currents, with maximum horizontal velocities of about $30 \text{ cm} \cdot \text{s}^{-1}$ in the lowermost 300 m water depth [Buß, 2011].

The CO_2 flux was roughly estimated on the basis of the rising heights of the fluids in the YK research area. By means of the density and stability first the heat flux, then the volume flux, and finally the helium flux per vent was calculated using values from the literature ($\text{heat}/{}^3\text{He} = 3.2 \cdot 10^{-7} \text{ J} \cdot \text{atom}^{-1}$; Ishibashi *et al.* [1995]). Taking the $\Delta C_T/{}^3\text{He}$ ratio from the linear regression through the data points of the YK (Fig. 14), a CO_2 flux of about $5 \text{ mol} \cdot \text{s}^{-1} \cdot \text{vent}^{-1}$ is estimated roughly. This is possible, assuming that all vents have about the same emission strength and contribute to the plume signal collectively. The CO_2 flux of each vent in the YK research area is of a magnitude of about 10^8 mol per year. However, these calculations are very rough because they base on several assumptions and values from the literature. A direct comparison to other CO_2 emission sites is very difficult, because of the low number of published values for individual vents. Reported estimated C and CO_2 fluxes of MOR, BABs, arc and non-arc volcanoes are in the order of 0.5 to $18 \cdot 10^{12} \text{ mol} \cdot \text{year}^{-1}$, but comprise the global fluxes at these systems (e.g. IEA Report [2008], Marty and Tolstikhin [1998], Resing *et al.* [2004]). One of the few available data of an individual emission site is from the submarine vent C7 in the hydrothermal system of Panarea (Mediterranean Sea). The island Panarea is an outcrop of a volcanic arc formed by the subduction of the Ionian

⁴⁴ My contribution of the cited part included all writing, which was proof-read by the co-authors.

plate under the European plate [*Caramanna et al.*, 2011]. The Panarea gas vents emit CO₂-rich hot fluids and bubble plumes of volcanic origin from several hydrothermal vents and geothermal springs in shallow water depths of 10 to 80 m [*Schmidt et al.*, 2015]. Measured fluxes of about 25 mol · s⁻¹ and 8 · 10⁸ mol · year⁻¹ are in about the same range as calculated for the YK [*Gugliandolo et al.*, 2006]. Although both systems are hardly comparable, they demonstrate the reliability of the calculated values to a certain extent.

“The linearity of the regression line (Fig. 14) indicates that either a single source – or several sources with a very narrow CO₂/³He signature range – dominates the fluid flux, or that not all of these known different vent types are influencing the water column higher than 10 m above the seafloor.

Liquid CO₂ droplets are especially expected to differ in the CO₂/³He ratios from the hot and bubble forming vent fluids. Release of fluids and condensed phases with different biogeochemical signatures should result in even higher scattering of the data points and the determination of different trend lines for individual stations or areas. The absence of such observations indicates that gas fractionation during degassing and hydrothermal convection processes occurs only to a limited extent [*Resing et al.*, 2004], or that one of these fractions dominates the hydrothermal flux.

Data from the CTD temperature sensor indicate that the majority of the plume anomalies found in the HK research area is caused by hot vents. At six of the eleven stations, an increase of temperature concurrent with plume-induced anomalies of the other parameters was observed. However, due to fast dissipation of heat, temperature anomalies within the water column are very small and distributed over a large water depth range (e.g. station 73, Fig. 12). A pronounced temperature increase in the profiles was only measured at station 75 (Fig. 12), that is located in close proximity to the known hot vents in the center of HK, at the point where the instrument intersected the buoyant plume. However, smaller anomalies of the non-buoyant plumes were frequently recorded both at HK and YK, as is shown in Fig. 15.”⁴⁵

⁴⁵ My contribution of the cited part included all writing, which was proof-read by the co-authors.

“In Fig. 15b the difference between the buoyant and non-buoyant plumes can be seen from the different signature in T-S space: the buoyant plume (profile 75) is characterized by higher temperatures compared to its surroundings ($\Delta\theta > 0.05^\circ\text{C}$) while at the same time the density is reduced by almost $0.01 \text{ kg} \cdot \text{m}^{-3}$ compared to the background. In the non-buoyant plume (profile 73), the temperature increase is smaller ($\Delta\theta = 0.01^\circ\text{C}$), and density compensated, i.e. the density is not significantly decreased. Plume-associated temperature anomalies $\Delta\theta$ were always derived from local derivations of the relation of potential temperature and potential density undisturbed by plume signals.”⁴⁶

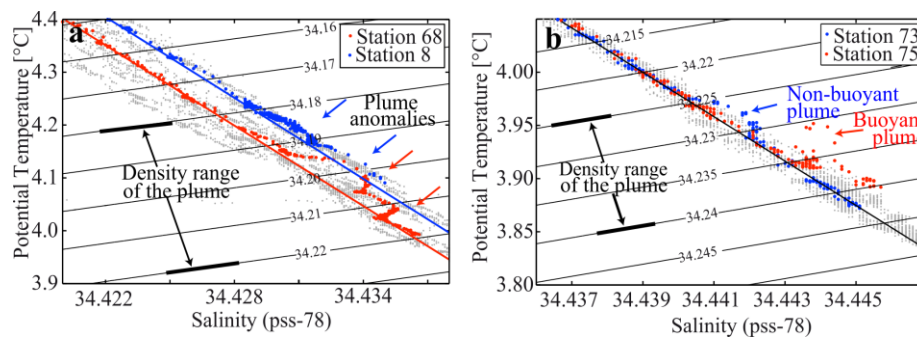


Fig. 15: “T/S- diagram showing plume anomalies in potential temperature and salinity at (a) YK (stations 68, 8) and (b) HK (stations 73, 75). Grey dots represent the scatter and serve to point out the variability in the measurements; the black line indicates an average profile undisturbed by plume signals. Plume anomalies are found in a density range of $34.18 \text{ kg} \cdot \text{m}^{-3} < \sigma_{1.5} < 34.22 \text{ kg} \cdot \text{m}^{-3}$ (YK) and $34.225 \text{ kg} \cdot \text{m}^{-3} < \sigma_{1.5} < 34.24 \text{ kg} \cdot \text{m}^{-3}$ (HK).”⁴⁷

“The assumption that the plume anomalies are caused mainly by hot vents is additionally supported by the $\text{CO}_2/{}^3\text{He}$ ratios of [condensed phase] sampled at HK. All of the investigated [...] condensed phases show $\text{CO}_2/{}^3\text{He}$ ratios in a range between 1.3 and $2.8 \cdot 10^{11}$ (Table 4). The slope of the linear trend line for the water column samples from HK research area (Fig. 14) indicates that the anomalies are caused by fluids with significantly lower $\text{CO}_2/{}^3\text{He}$ -ratios, by a factor of 4 to 9.

Two different theories about the source and origin of liquid CO_2 in BABs have been reported so far. *Lupton et al.* [2006] proposed a liquid CO_2 pool, capped by a CO_2 -GH

⁴⁶ Data analysis for this part was made by A. Buß. My contribution of the here cited part included all writing, which was proof-read by the co-authors.

⁴⁷ These figures and caption are used in the article mentioned above. Data analysis, construction and compilation of data in the figure was done by A. Buß and M. Walter.

layer beneath the seafloor. CO₂ droplets are released through the sediment surface, amplified by disturbance of the seafloor and penetration of the hydrate cap, or via interaction and entrainment into the hot fluid flow. According to the conceptual model of *Konno et al.* [2006], a CO₂-rich vapor phase that is produced by subseafloor boiling is subsequently cooled down to temperatures below 10°C, leading to the formation of GH within the sediment. Hydrates consolidate the sediments and may act as a caprock or seal for rising fluids that accumulate below the sediment surface. When the hydrate cap is ruptured, pressure and temperature conditions facilitate the release of liquid CO₂. Both theories can explain the CO₂-dominance of the fluids and condensed phases [in BABs]. [Due to the absence of] sedimentary coverage around the bubble and droplets release sites at HK, and despite extensive use of a sedimentary heat probe by the ROV in the YK research area, [no] release of droplets [was observed] after rupturing the sediment surface near the active sites.

The formation of GH should lead to gas fractionation, especially between hydrate-forming gases like CO₂ and smaller gas molecules which cannot stabilize the hydrate lattice [*Sloan and Koh, 2008*]. *Konno et al.* [2006] reported significant CO₂/H₂ fractionation for the YK field. Based on the fact that helium behaves similarly with respect to hydrate formation, [it can be assumed] that decomposition of GH should lead to a He-depleted liquid CO₂ phase. This is further supported by the clear evidence of He-exclusion from natural (methane-dominated) hydrate occurrences (e.g. *Winckler et al.* [2002]).⁴⁸

5.4. Correlation between ΔC_T and pH

“The relationship between ΔC_T and ΔpH can be used to distinguish between acidification caused by hydrothermal vent emissions of CO₂ and of that due to any other acidic compound [*Resing et al., 2004; 2009*]. This is illustrated by Fig. 16b, where the black horizontal dashed line describes acidification without any CO₂ increase (‘100 % acid’) and the brown sloped dashed line shows the expected trend

⁴⁸ My contribution of the cited part included all writing, which was proof-read by the co-authors.

line for changes in pH that are exclusively caused by the addition of CO₂ ('100 % CO₂'). The latter relationship was derived from the dissociation constants for the marine CO₂ system using the C_T, A_T, temperature, and salinity of the considered samples using the program CO2SYS (Pelletier *et al.*, 2007; settings for calculation: K₁ and K₂ constants from Millero *et al.* [2006], K_S values from Dickson [1990], total pH scale). With constant A_T, C_T was gradually increased in 10 μmol · kg⁻¹ intervals for each sample in the plume-induced water column up to ΔC_T of 100 μmol · kg⁻¹ and the resulting change in the pH value (ΔpH) was calculated. This calculation is very robust with respect to the analytical uncertainty of A_T. Results of this ΔC_T-ΔpH-correlation exclusively caused by addition of CO₂ are shown in Fig. 16a as grey lines for each sample. The brown dashed line (Figs. 14a and b) represents the mean of all ΔC_T-ΔpH trend lines calculated for the individual samples. The trends for stations 57 and 59 were not considered as explained in Chapter 5.5.

ΔC_T and ΔpH data of both the YK and the HK research areas plot close to the 100 % CO₂ line and show a distinct linearity (Fig. 16b). The linearity is even more pronounced when considering individual stations (e.g. station 68, Fig. 16b inset). This clearly indicates that the observed pH changes can be attributed almost entirely, but not exclusively, to the input of CO₂. The slightly smaller slope at YK might indicate a stronger influence of other acids on the fluids in comparison to HK, although the slope of the regression line has a relatively large confidence interval due to the scatter of data, bearing the risk of over- or underestimation.

[...] The observed CO₂-dominance on the pH reduction at both [areas] is in contrast to the release of large amounts of other acids reported from other BAB sites in the Western Pacific Ocean, where up to 80 % of the decrease in pH is due to addition of acidity [Fouquet *et al.*, 1991; Gamo *et al.*, 1997; Resing *et al.*, 2004] caused by interaction with [intermediate to] acidic volcanic rocks [Ishibashi and Urabe, 1995; Ishibashi, 1991]. However, these results are in agreement with the trend observed for the CO₂-dominated NW-Eifuku hydrothermal system [Resing *et al.*, 2009].”⁴⁹

⁴⁹ My contribution of the cited part included all writing, which was proof-read by the co-authors.

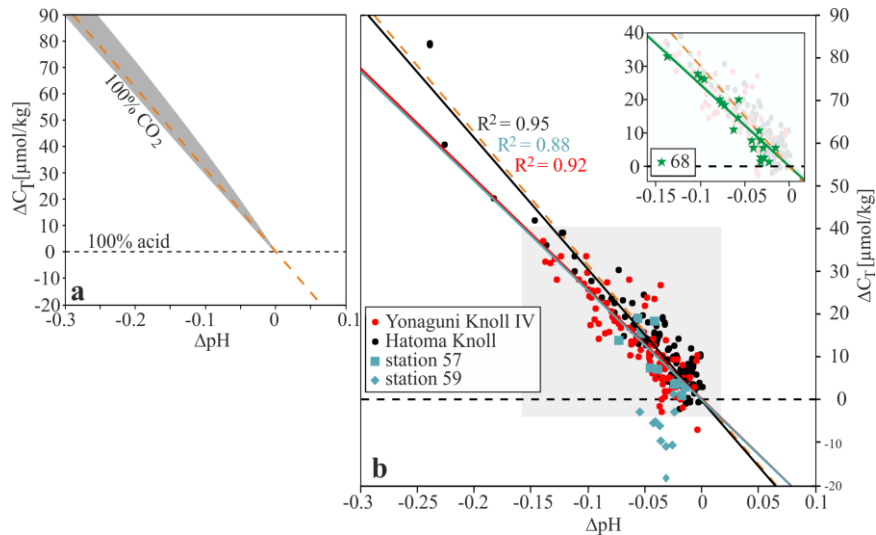


Fig. 16: “(b) Plot of ΔC_T against ΔpH for samples from YK, HK, and stations 57 and 59. Solid red, black, and blue lines are the linear [...] regression lines for the data points from YK, HK, and station 57, respectively (calculated with a SMA analysis in R; package „smatr“). Horizontal black dashed line indicates pH reduction by addition of pure acids (‘100 % acid’), the brown sloped dashed line describes the case that changes in pH are exclusively caused by the addition of CO₂ (‘100 % CO₂’). The latter is the mean slope of the ΔC_T - ΔpH -relationship of each sample (samples from station 57 and 59 excluded) in the plume-induced water column, calculated by incremental increase of C_T using the program CO2SYS (grey lines in Fig. a) [Pelletier *et al.*, 2007]. The inset at the top of Fig. b shows data from station 68, as an example of considerably lower scatter of the regression line of individual stations compared to the general approach of all samples in the YK research area.”⁵⁰

The linear relationship between ΔpH and ΔC_T , from both YK and HK, supports the independent ΔpH and ΔC_T approaches and in particular, the use of the pH sensor data after applying reference and background determination. As pointed out above (Chapter 4.1.1), sampling for C_T during continuous (but slow) upcast movement, as well as the use of pH-sensor with an inherent time lag, must have led to a smoothing and slight upward migration of the geochemical signals. However, the consistency of plume-related signals from the different sensors and sampling, and in particular the very strong correlation of ΔpH and ΔC_T , justifies the approach. In particular, the peak-formed shape of the hydrothermal plumes would have led to enhanced scatter or lack of correlation in the case that the correlated properties had been recorded or had samples with a significant phase shift (relative to the widths of the signals). Due to the

⁵⁰ These figures and caption are used in the article mentioned above. Data analysis, construction and compilation of data in the figure was done by myself.

linearity of the relationships between most individual parameters (${}^3\text{He}^{\text{excess}}$, ΔCO_2 , ΔpH), slight mixing effects will, to some extent, have affected the shape and amplitude of the observed hydrothermal signals, but not their relative values. Some of the scatter in Fig. 16b might be a result of [the] sampling approach. Despite the fact that pH-probes are frequently used for hydrographic surveys, the data are not often used for scientific analysis in the literature due to calibration and time lag issues. The use of aligned pH-profiles to derive water column pH deviations from a reference cast (ΔpH) from the upcast, in combination to a slow, highly reproducible, but uninterrupted sampling for discrete measurements, appears to be a promising method for the quantitative treatment of SBE 18 pH-sensor data for plume characterization.”⁵¹

5.5. *Characteristics of stations 57 and 59*

“In terms of position (horizontally and vertically), station 57 differs considerably from the remaining YK stations. It is located at the flank of the northeastern seamount in the YK research area, about one nautical mile away from the valley (Fig. 6a), and has a maximum water depth of 1100 m (Fig. 17). The maximum potential density at station 57 ($34.17 \text{ kg} \cdot \text{m}^{-3}$) is considerably lower than from all other investigated stations. ΔC_T , ${}^3\text{He}^{\text{excess}}$, and ΔpH from station 57 are similar to the residual YK stations, although in the lower part of the range. Correlation between these values indicates a slightly lower $\Delta C_T/{}^3\text{He}$ ratio in the initial fluids of station 57 ($1.6 \cdot 10^{10}$; Fig. 14) and almost the same influence of CO_2 on pH (Fig. 16), compared to remaining YK samples.

The vertical distribution of the geochemical parameters ${}^3\text{He}^{\text{excess}}$, ΔC_T , ΔpH , and $d\text{Eh}/dt$ indicates that the lower water column at station 57 is slightly influenced by plumes (Fig. 17). The dominant water current conditions during investigation towards south to southwest indicate that these anomalies originate from the north or northeast and therefore give evidence for a yet undiscovered vent located at the seamount. In 2002 elevated manganese and methane concentrations, as well as slightly reduced

⁵¹ My contribution of the cited part included all writing, which was proof-read by the co-authors.

light transmission were determined within the lowermost water column northeast of station 57, also indicating the existence of a hydrothermal vent in close proximity (SPOT-1; *Gamo et al.* [2010]). However, it has to be emphasized that the number of data points reported here is relatively low and additionally that the ΔC_T - $\Delta p\text{H}$ -plot shows large scatter. Thus, more data are needed for a detailed geochemical characterization of the initial fluid and to determine the exact position of the vent.

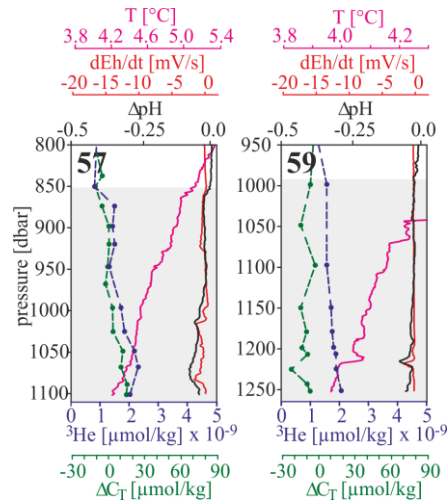


Fig. 17: “Lowermost 310 m of stations 57 and 59, both located at the slope of the northeastern seamount; ΔC_T (green), $^3\text{He}^{\text{excess}}$ (blue), $\Delta p\text{H}$ (black), $d\text{Eh}/dt$ (red), and T (pink).”⁵²

Station 59 is located at the lower part of the flank of this seamount, at about 1250 m water depth (Fig. 6a). Almost constant geochemical parameters along the water column show minimal indicators for hydrothermal activity [...] (Fig. 17). LADCP measurements show that water currents during the time of sampling were orientated in the west / southwest direction, which indicates that the water entered from a slight sill between two seamounts into the valley. Apparently, this water is characterized by a lower C_T than the reference station due to different biogeochemical background, which causes apparent negative ΔC_T values.”⁵³ There is no indication in the data, that this problem was encountered at any other station. Slight increase of $^3\text{He}^{\text{excess}}$ with increasing water depth, as well as small anomalies in $\Delta p\text{H}$ and $d\text{Eh}/dt$ at the station may point to the existence of a hydrothermal vent. However, wide scattering of the

⁵² These figures and caption are used in the article mentioned above. Data analysis, construction and compilation of data in the figure was done by myself.

⁵³ My contribution of the cited part included all writing, which was proof-read by the co-authors.

data regarding $\Delta C_T/{}^3\text{He}^{\text{excess}}$ and $\Delta C_T/\Delta\text{pH}$ ratio constrains statements about the potential $\text{CO}_2/{}^3\text{He}$ ratio of the initial fluid, and of the influence of CO_2 or acids on pH.

5.6. Expected geochemical signature of the lowermost water column

The pH decrease within the water column at both research areas, HK and YK, and at station 57 seems to be caused mainly by CO_2 addition, as inferred from the $\Delta C_T/\Delta\text{pH}$ regression line (Fig. 16). The slope of these lines indicates, that no significant CaCO_3 dissolution processes occurred during the rise of the fluids through the sediment. However, these results are only applicable to the hot fluids, which cause the main geochemical anomalies in the investigated part of the water column. “At cold and warm vents in the YK research area (temperature $< 90^\circ\text{C}$) CaCO_3 dissolution dominates the interaction of the rising fluids with the sediment [Häckel, 2011]. Lack of indicators for this process in the investigated samples leads to the conclusion that the influence of these fluids is limited to the lowermost 10 m of the water column and / or is obscured by the imprint of the dominating hot fluids.

Due to the diffuse flow of CO_2 from liquid or supercritical CO_2 from the sediments and subsequent dissolution of emitted bubbles and droplets, the lowermost water column might differ considerably from the investigated interval of the water column with respect to its geochemical signature. However, fast dissolution at the bottom layer and decreasing dissolution flow with increasing rising height will cause the formation of a gradient, at least with regard to CO_2 .”⁵⁴

⁵⁴ My contribution of the cited part included all writing, which was proof-read by the co-authors.

6. Geochemical variability of the condensed phases at HK

6.1. Differences between individual emission sites

All of the investigated emission sites at HK were characterized by rocky and stony seafloor with lack of sediment. Even in far distance to known hydrothermal sites, only a small extent of soft sediment was present, hence penetration of a temperature lance or sediment corer was not possible or only for a few centimeters.

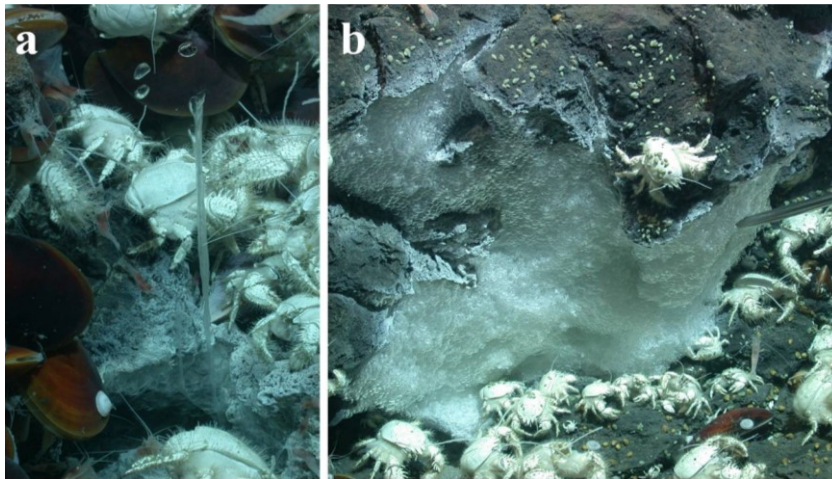


Fig. 18: Formation of translucent GH skins after emission as (a) elongated conical GH pipes or (b) foam-like accumulation at small rock ledges. copyright: MARUM University of Bremen

Condensed phase emission occurred in clusters. Several vents were located close together, separated by areas with absence of any hydrothermal emission activity. At most of the vents, the emission of the condensed phase occurred in a relatively steady flux of about 6 to $9 \text{ ml} \cdot \text{min}^{-1}$ taking the time needed to fill the GS completely. Individual vents showed inconsistent emission fluxes with longer times of inactivity. Irregular almost pulse-like emission reduced the rates to $5 \text{ ml} \cdot \text{min}^{-1}$. Two different kinds of vents were distinguished, based on temperature measured by the Hi-Temp lance and video material. Condensed phase was emitted discontinuously at the warm vent during dive 200. Vent temperatures of only about 5°C were measured at all vents from dive 202, partly located close to warm, non-bubble emitting vents, that influenced the surrounding deep sea water (ΔT up to 0.75°C). The condensed phases often tended to form translucent GH skins after emission. These coated condensed phases generated foam-like accumulations at small rock ledges (Fig. 18b).

6.1.1. Dive 199

In close proximity to the emission site of GS 4 condensed phases were released at several points. The vents were characterized by discontinuous emission with long periods of no activity and a sudden pulse-like emission plume.

Coated condensed phases accumulated in foam-like structures at small rock ledges, shortly after their release due to the fast formation of a GH skin (Fig. 18b). Elongated conical GH pipes were formed at this emission site (Fig. 18a) as already reported by *Sakai et al.* [1990a] at Izena Hole. The pipes grew continuously to lengths of several decimeters, before they got pinched off at the lower end, teared off, and rose upwards with the buoyancy of the fluids.

6.1.2. Dive 200

The emission site investigated during dive 200 was located at the north-eastern rim of the caldera. Video recording of the sampling site from GS 1 and 3 showed shimmering water (partly visible in Appendix III) of slightly elevated fluctuating temperature (Table 4). The vent emitted warm water continuously, but gas bubbles discontinuously and pulsatingly, which reduced the flux rate to about $5 \text{ ml} \cdot \text{min}^{-1}$. The flux was affected by interruptions, while the GS 1 was filled, but continued after being stimulated by moving a stone above.

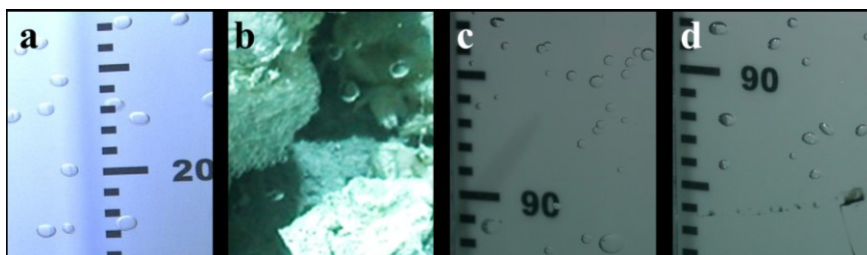


Fig. 19: Variable shape of condensed phases at the different emission sites: (a) dive 200, GS 3, (b) dive 202, GS 4, (c) dive 202, GS 3, and (d) dive 202, GS 2. Pictures a, c, and d show condensed phases „caught“ with the bubble box. The graduated scale enables only a rough estimation of the size due to potential distance parallax. copyright: MARUM University of Bremen

Only a few centimeters inside the rock of the vent, temperatures of up to 50°C were measured using a temperature probe. Right after emission, GH were formed in the sampling funnel of GS 1 during the residence time. Delayed GH coating during the

rise through the seawater was monitored during the bubble box-based rising experiments as well. Slightly oval bubbles with a solid structure - very rigid, hardly oscillating, rotating, and modifying in shape - were detected during the time of observation (Fig. 19a).

6.1.3. Dive 202

GS1, 3 and 4 were filled in close proximity to each other at the north-western rim of the caldera. Larger bubbles with a broader bubble size distribution were collected at an adjacent vent with GS 1, which however failed for unknown reasons. The GS was empty onboard. Temperature measurements at the release site of GS 4 indicated the emission of cold fluids (5.2°C). Although vent temperature from the GS 3 release site was not measured, constant and low ambient water temperatures lead to the assumption, that the fluids were low-temperated as well. The flux at the vent of GS 4 was relatively low ($6 \text{ ml} \cdot \text{min}^{-1}$), at the vent of GS 3 it was highest with about $9 \text{ ml} \cdot \text{min}^{-1}$. Video material from the bubble box showed condensed phases at the GS 3 vent with a more spherical shape and minor oscillation (Fig. 19c). The condensed phases rise relatively slow with velocities between $19 \text{ cm} \cdot \text{s}^{-1}$ and $24 \text{ cm} \cdot \text{s}^{-1}$, $22 \text{ cm} \cdot \text{s}^{-1}$ in average. Formation of a GH skin or a foam-like accumulation in close proximity to the vent was not observed. The condensed phases, which were caught at the entry of the GS, were easy to shake off.

The release site of GS 2 is located at the central mound - the hydrothermally most active area of the HK at the time. The emitted condensed phase was characterized by vigorous oscillation and fast ascent between $22 \text{ cm} \cdot \text{s}^{-1}$ and $30 \text{ cm} \cdot \text{s}^{-1}$, $25 \text{ cm} \cdot \text{s}^{-1}$ in average (Fig. 19d) which had a relatively high flux rate of $8 \text{ ml} \cdot \text{min}^{-1}$. At the sampling site low vent temperatures of about 5°C were measured, however no formation of GH skins became apparent. Further vents were detected in close proximity to this bubble emission site, partially emitting bubble-free, warm, or hot fluids. Temperatures of 66°C and higher were measured close to the sampling site (Fig. 20). Flares of these vents influenced the water column at the emission site of GS 2, apparent as slightly fluctuating temperatures measured by the ROV.

Table 4: Gas composition of the investigated gassampler fractions

Gassampler Fraction		Dive 200			Dive 202						
		3		4			3		2		
		1	3	1	3	4	1	4	1	3	
CO ₂	[mole-%]	62.6	62.8	82.0	84.4	81.2	71.2	88.8	43.7	43.3	
CH ₄	[mole-%]	32.6	32.5	14.6	13.2	15.9	22.8	8.7	50.1	50.3	
H ₂ S	[mole-%]	0.9	0.8	1.9	0.9	0.8	0.7	1.3	0.4	n.d.	
N ₂	[mole-%]	3.8	3.8	1.5	1.5	2.0	2.9	1.2	5.6	6.1	
O ₂	[ppm]	278	279	358	282	438	254	170	440	695	
Ar	[ppm]	232	193	70	74	160	202	98	382	401	
H ₂	[ppm]	342	19	n.d.	77	n.d.	23,311	241	136	225	
C ₂ H ₆	[ppm]	302	284	77	52	130	< LOQ	< LOQ	933	922	
C ₃ H ₈ **	[ppm]	n.d.		5.5		5.4		3.3	7.4	108	
³ He	[ppt]	2.2	7.4	4.5		3.9	5.6		2.9		
⁴ He	[ppm]	0.3	0.7	0.8		0.6	0.7		0.6		
R/R _{atm}		5.8	7.2	4.2		4.7	6.1		3.5		
δ ¹³ C(CH ₄)	[‰ VPDB]	-45.1	-44.8	-48.2	-47.8		-47.6	-47.9*	-47.6	-47.5	
δ ¹³ C(CO ₂)	[‰ VPDB]	-7.5	-6.5	-7.4	-7.7		-7.2	-7.0*	-6.5	-7.2	
CO ₂ / ³ He	[· 10 ¹¹]	2.81	0.85	1.82		2.08	1.27		1.51		
Water temperature	[°C]	3.94 – 4.52 (Ø 4.14)			3.91			3.91		3.99 – 4.74 (Ø 4.35)	
vent temperature	[°C]	50			5.2			----		5	

* δ¹³C values from Fraction 2 ** already measured onboard

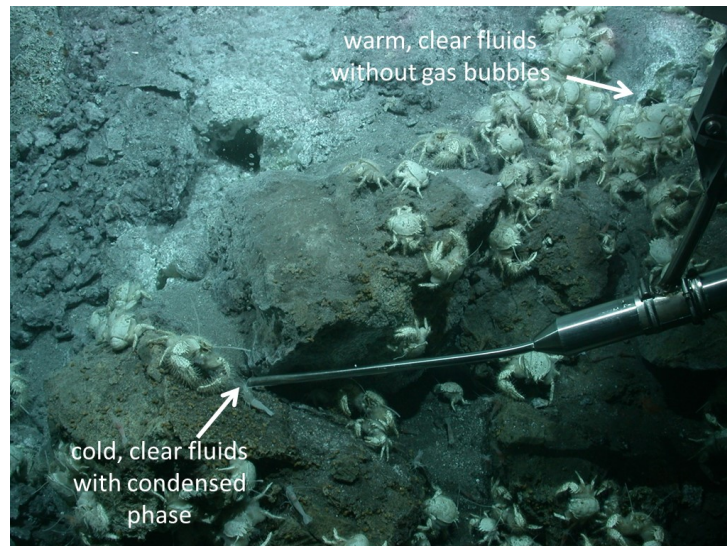


Fig. 20: Close proximity of the low-temperature vent 202, GS 2 (5°C) emitting clear fluids and condensed phase (lower left corner) and warm, clear fluids (up to 66°C) without condensed phase (right upper corner). For estimation of the distance, length of metal lance is about 40 cm. copyright: MARUM University of Bremen

6.2. *Variability of the gas composition*

The sampled condensed phases mainly consist of carbon dioxide and methane (> 93 %; Table 4). However, the ratio of both gases differs and can be classified as CO₂-dominant or almost equal, with strong impact on the nature of the condensed phase. The residual volume fraction consists of nitrogen, oxygen, argon, hydrogen, hydrogen sulfide, ethane, propane, and helium. Such a comprehensive geochemical composition of condensed phases has not been determined before, hence the comparability with other studies is limited.

Last fraction of each sample represents the initial gas composition of the emitted condensed phase, because composition homogeneity only occurs after pressure reduction by release or expansion. As previously mentioned, results of samples from dive 199, GS 4 and dive 200, GS 1 are discarded from acquisition due to difficulties during sampling. GH formation within the funnel possibly led to fractionation. Less soluble gases like methane accumulate in the gas phase due to the presence of pore water inside the GS.

6.2.1. CO₂-dominated condensed phases

CO₂-dominated condensed phases are collected at the northwestern flank of the caldera (dive 202, GS 3 and 4) and east of the central mound (dive 200, GS 3). The last fractions of each GS vary in CO₂ concentration between 62.8 and 88.8 mole-%. These values are lower than the 84 – 98 % and 89 – 100 % from the condensed phases that are emitted in the residual OT [Konno *et al.*, 2006; Sakai *et al.*, 1990a; Shitashima *et al.*, 2008], and Mariana and Tonga-Kermadec Arc [Lupton *et al.*, 2006; 2008], respectively (Appendix V), but agree with the general knowledge on CO₂-richness of hydrothermal fluids at arc-related hydrothermal systems.

The second most common gas in the GS is methane with concentrations of 8.7 to 32.5 mole-%. Despite the great variation between the samples, they exceed almost all reported values from other deep-sea condensed phases, which are in the range of some hundred ppm. Only three condensed phases at BABs and MORs with methane levels similar to dive 202, GS 3 and 4 are known so far. Konno *et al.* [2006] measured almost comparable elevated concentrations in the droplets in YK (up to 15.4 %). Likewise enhanced CH₄ levels arise in the gas phase at the JADE hydrothermal area [Sakai *et al.*, 1990a], however it is not clear how high the contribution of methane and hydrogen is to the up to 11 % of ‘residual gas’. Collected gas bubbles from the Jan Mayen vent field at the Arctic Mid-Atlantic Ridge contain elevated methane concentration of 7.1 % on average (Pedersen and Baumberger [2011]; <https://doi.pangaea.de/10.1594/PANGAEA.788169>), though values are thought to be even higher due to dilution with air during sample handling and measurements [T. Baumberger, pers. comm.].

N₂ concentrations of the three GS (1.2 to 3.8 mole-%) are in the range of the arc-related hydrothermal systems [Lupton *et al.*, 2008], although the number of comparable reports are limited, because of not quantifying nitrogen [Konno *et al.*, 2006; Sakai *et al.*, 1990a; Shitashima *et al.*, 2008] or of evidence of contamination with air during sample handling and measurements [Lupton *et al.*, 2006; 2008].

In literature, the values for hydrogen sulfide and hydrogen are more limited. The values from the GS range between 0.8 - 1.3 mole-% H₂S and are up to 241 ppm H₂. They are comparable or even lower than values from the Mariana Arc, Tonga-Kermadec Arc, and the residual OT [Konno *et al.*, 2006; Lupton *et al.*, 2006; 2008; Sakai *et al.*, 1990a; Shitashima *et al.*, 2008].

6.2.2. *Non-CO₂-dominated condensed phase*

Highly enhanced methane concentrations are detected in dive 202, GS 2. Even though the number of investigated systems in arc- and ridge-related hydrothermal areas is limited, this high value exceeds all so far known deep-sea condensed phases [Konno *et al.*, 2006; Lupton *et al.*, 2008; Sakai *et al.*, 1990a]. Such elevated concentrations are only known from cold seeps at the ocean margins and continental shelves [Römer *et al.*, 2012; Sahling *et al.*, 2014], and cold, shallow, natural hydrocarbon seepage sites [Clark *et al.*, 2003; 2010]. It seems that the biogeochemical, tectonic, lithospheric, and sedimentary conditions at the OT promote the excessive formation and/or enhancement of methane in those fluids (Chapter 6.3).

The content of the residual gas components varies between CO₂- and non-CO₂-dominated samples, with the exception of ⁴He, whose concentration is almost constant for all samples. Nitrogen, argon, and ethane are considerably enriched in the non-CO₂-dominated sample. Hydrogen concentration is also elevated in this sample and is about the same level like dive 202, GS 3. Hydrogen sulfide is not detectable in GS 2.

6.3. *Potential origin of the gas components*

The geochemical signature of the fluids is primarily affected by the geological conditions at the deep hydrothermal reaction zone, when the seawater subterraneously interacts with rock and magma at high temperatures [Kawagucci, 2015; Kawagucci *et al.*, 2020; Sakai *et al.*, 1990a]. Ishibashi [1991] suggests, that all emitted gases at sediment-starved hydrothermal systems are primarily magmatic in origin. Due to the complexity of tectonic processes at the BABs, the composition of the magma is not

only influenced by the earth's mantle, but also by the crust and deposited sedimentary material from the subducted tectonic plate [Gamo *et al.*, 2006; Marty *et al.*, 1989].

Additionally, microbial, chemical, and advective processes and effects in the low-temperature discharge zone are reported to influence the gas composition. A scheme of potential sources of the different gas components at the HK is presented in Fig. 21 based on geochemical tracers (isotope ratio, concentration, relative abundance of different gases) and results of former investigations at hydrothermal vents. The enrichment and distribution processes are presented schematically and partly simplified in Fig. 21, for example in the high-temperature reaction zone. On the one hand deposited material from the crust and the sediments on the subducted Philippine Sea Plate attains the magma chamber by melting. Prevailing temperature and pressure conditions promote thermal degradation and finally outgassing or complete degassing towards the hydrothermal fluids. Just as important, but more difficult to depict, is on the other hand the direct interaction of hydrothermal fluids with the subducted plate before they reach the magma chamber, which is already hot due to its proximity. In Fig. 21 both processes are represented with two interconnected arrows left of the magma chamber ('high-temperature reaction zone'). A differentiation of both processes is not possible only by the use of geochemical tracers. Hence, all gases that are subsequently identified to be of subduction zone origin reach the hydrothermal fluids by one of these two processes.

It has to be mentioned that these geochemical tracers can only give hints to the supposed gas origin and are indicative only to a limited extent. Especially concentrations and relative abundances of different gases bear the risk of over-interpretation. Most limiting for classification of different sources are results from laboratory experiments or field work at natural hydrothermal vents, which are only valid for systems with dissolved gas emission. There are only very few investigations of condensed phases. Hence, it is difficult to estimate, if these attributes of classification apply for condensed phases as well. Fractionation between gases due to their different solubility in magma and water or different potential to form GH, is very

likely in these fluids. Hence, they are significant only to a limited extent, such as the $\text{CO}_2/{}^3\text{He}$ ratios [Lupton *et al.*, 2015]. Nevertheless, all geochemical tracers are interpreted in the following chapters to estimate the most likely sources of all these gases due to their potential indication.

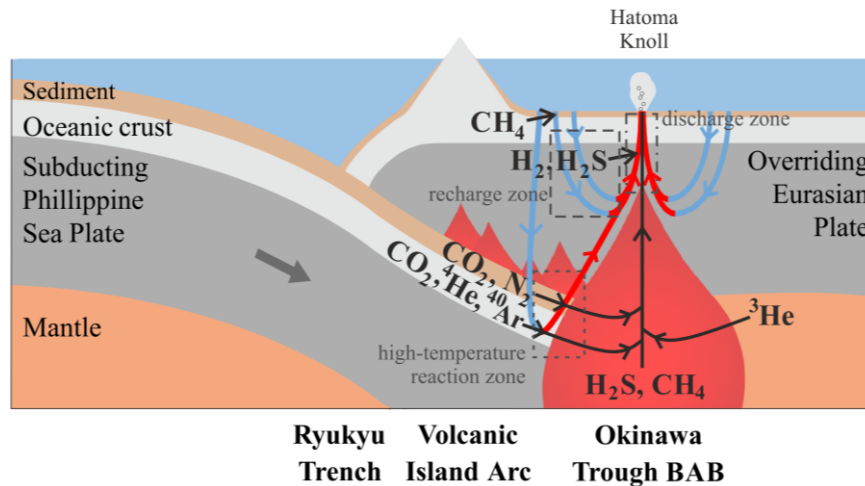


Fig. 21: Formation of hydrothermal fluids at the OT back-arc basin (BAB) and different assumed sources of gas components for the investigated HK vents.

6.3.1. Carbon dioxide

$\delta^{13}\text{C}(\text{CO}_2)$ ratios of all collected condensed phases are very uniform and roughly in the range of the hot fluids (325°C) close to the main active vent in the center of the HK (-7.9‰ ; Kawagucci [2015]). Konno *et al.* [2006] reported the same uniformity of the isotopic ratio for the hydrothermal vents in the YK. Following their conclusions, all different vent fluids within the HK research area derive from a common CO_2 source independent on location or temperature of the vent. Within the discharge zone secondary modification processes will lead to the variability in CO_2 content.

The geochemical tracers hint to two different origins of the carbon dioxide. Very high CO_2 concentrations indicate, that the gas has its origin in the direct degassing of the magma body. Based on studies from Javoy *et al.* [1986] this assumption is supported by the measured isotopic ratio of the carbon dioxide ($\delta^{13}\text{C}(\text{CO}_2) = -6.5$ to -7.7‰). They reported values between -5 to -8‰ to point to a mantle-derived input.

In contrast to this, Holland and Gilfillan [2013] declare that stable carbon isotope ratios as low as -8‰ can also indicate crustal sources such as the metamorphism of carbonate rocks. This assumption is supported by the very high $\text{CO}_2/{}^3\text{He}$ ratios of 0.9

to $2.1 \cdot 10^{11}$. Values greater than $1 \cdot 10^{10}$ indicate, that the CO_2 originates from the crust, that is depleted in ^3He and not from the mantle, which has a significant amount of magmatic ^3He ($< 1 \cdot 10^{10}$) [Holland and Gilfillan, 2013].

At first sight, both substantially different conclusions on the basis of the geochemical tracers to mantle-derived and crustal source of the CO_2 can hardly be brought into agreement. However, the special characteristic of BABs, that the oceanic crust of the subducted Philippine Sea Plate has a considerable influence on the geochemical composition of the magma body, reconciles both presumable origins.

Furthermore, CO_2 from sedimentary marine organic- and carbonate-rich material of the subducted tectonic plate can incorporate into arc melts [Hilton *et al.*, 2002] which elevates the CO_2 content of the fluids. The isotopic composition of the carbon dioxide seems to be affected only to a limited extent. The $\delta^{13}\text{C}(\text{CO}_2)$ ratio of marine carbonates is about 0 ‰ [Hoefs, 1980] and compensates the light carbon isotopy of marine organic material which is about in the range of -29 and -7 ‰ [Hunt, 1966].

6.3.2. Methane

The origin of methane in the hydrothermal fluids at HK can be determined using the ratios of hydrogen and methane (H_2/CH_4), methane and the sum of ethane and propane ($\text{C}_1/(\text{C}_2+\text{C}_3)$) as well as the geochemical tracer $\delta^{13}\text{C}(\text{CH}_4)$.

Very low H_2/CH_4 ratios of almost all gas samples are an indicator for microbial methane input. H_2/CH_4 ratios in the last fractions of all samples are below $3 \cdot 10^{-4}$, hence in the range of microbial produced methane ($\text{H}_2/\text{CH}_4 < 0.02$). This assumption is further supported by a very high relative abundance of CH_4 to non-methane hydrocarbons ($5 \cdot 10^2$ to $9 \cdot 10^3$). Based on Whiticar [1999], $\text{C}_1/(\text{C}_2+\text{C}_3)$ ratios greater than about $1 \cdot 10^2$ indicate a biogenic source (Fig. 22).

Kawagucci [2015] pointed out that thermal decomposition of thermogenic hydrocarbons into methane will also lead to an elevated $\text{C}_1/(\text{C}_2+\text{C}_3)$ ratio in the range of biogenic methane. He concludes, that even a ratio of more than $1 \cdot 10^3$ is no definite indicator for pure biogenic hydrocarbon production. Also the carbon-isotopic ratios ($\delta^{13}\text{C}(\text{CH}_4)$) of the gas samples rather indicate thermal decomposition of organic

matter as the origin of methane, using the Bernard diagram from *Whiticar* [1999] (based on investigations of *Bernard* [1978]; Fig. 22, grey areas). $\delta^{13}\text{C}$ values of -45 and -48 ‰ VPDB are very close to the transitional area between bacterially and thermogenically produced methane. Furthermore, recent studies presume that thermogenic methane in the OT rather comprises a carbon-isotope range of -30 to -20 ‰ and that the very low $\delta^{13}\text{C}$ values measured by *Whiticar* [1999] are an artefact of mixing of thermogenic methane with ^{13}C -depleted biogenic CH_4 (-100 to -40 ‰) (*Kawagucci* [2015] and references therein; Fig. 22, blue striped area).

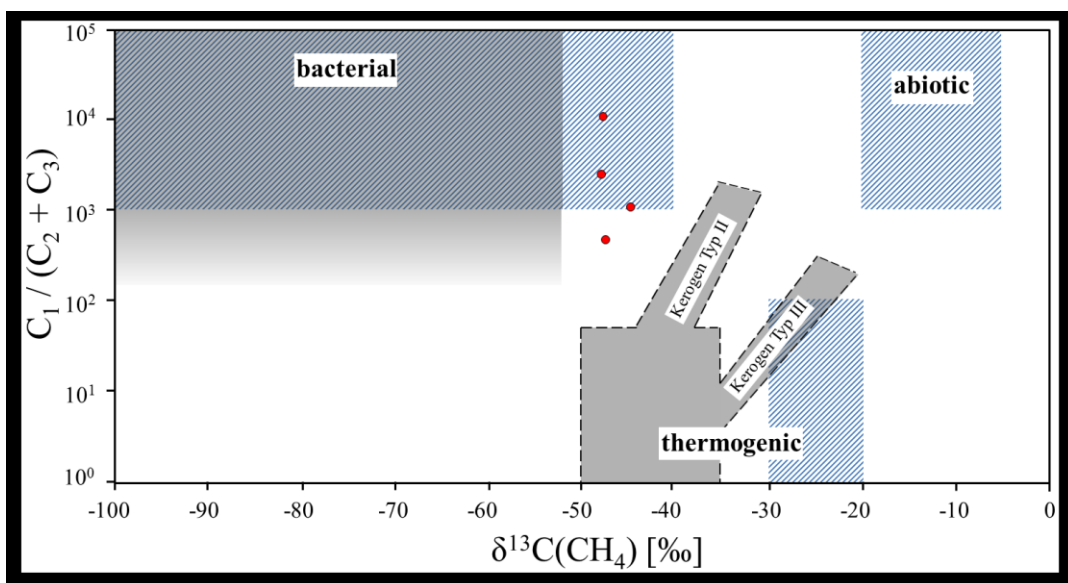


Fig. 22: Bernard diagram (after *Bernard* [1978]). The red points show the relative abundances of methane and non-methane hydrocarbons and carbon-isotopic ratios of the measured gas samples. Grey filled areas represent the estimations after *Whiticar* [1999], blue striped areas the results from *Kawagucci* [2015]. The abiotic methane-area from *Kawagucci* [2015] is an assumption based on sediment-starved vent fields in the OT.

It seems that the origin of methane is a combination of biogenic and thermogenic methane input. However, the conditions at the vents contradicts this. During ROV dives on cruise SO 196-2, only small sedimentary coverage appears in the whole HK caldera [*Häckel*, 2011], which is furthermore penetrated with solid precipitates [*Rehder and Schneider von Deimling*, 2008]. The seafloor close to the vents seems to be composed solely of rocks. Lack of sediment in the discharge zone impedes hydrogenotrophic or organotrophic methanogenesis.

The 'Microbial Methanogenesis at Recharge stage' (MMR) model is an approach to bring these issues in accordance [Kawagucci *et al.*, 2011; 2013]. It assumes that the hydrothermal fluid is already enriched in methane in the organic-rich sedimentary recharge zone due to chemical and biological processes. Inertness of methane against the conditions in the high-temperature hydrothermal reaction zone prevents degradation or consumption, hence methane is still present in the fluid in the discharge zone and during ascent. Because a distance of some kilometers between recharge zone and vent is possible, the sediment-rich seafloor around the HK caldera is supposed to be a likely location of the recharge zone [Kawagucci, 2015]. Mukumoto *et al.* [2019] identified a large gas reservoir more than 5 km along the rifting axis as the potential distribution pathway of the methane emitted at the Iheya North Knoll (mid-OT). Similar to the results from CO₂, carbon isotope ratios are uniform in the condensed phases, hot fluids (325°C), and the surrounding water body close to the main active vent in the center of the HK (-45.2 to -50 ‰; Kawagucci [2015]; Yamamoto *et al.* [2015]). This indicates a common source of methane. Within the discharge zone, molecular fractionation leads to variable methane concentrations in the fluids.

6.3.3. Hydrogen and Hydrogen sulfide

Hydrothermal degradation of sedimentary organic matter at high temperatures and pressures is a potential origin of hydrogen [Kawagucci *et al.*, 2011]. However, rapid reaction kinetic diminishes the hydrogen content within or ahead of the reaction zone and therefore buffers almost all of the H₂ produced up to this point [Kawagucci, 2015]. Hence, hydrogen reaches the fluids especially in the discharge zone. Chemical weathering of rocks due to thermogenic interaction with the hot fluids during the ascent is a likely source for hydrogen [Von Damm, 2000]. For hydrothermal fluids containing dissolved hydrogen, it has been reported that the concentration of H₂ in the fluids can indicate the host rock type [Kawagucci *et al.*, 2013]. The rather low hydrogen concentrations in almost all GS indicate interaction with silicic rocks. Kawagucci *et al.* [2011] estimated the fluid residence time in the discharge zone to be approximately one hour. Within such a brief period, the interaction between the fluid

60

and the rock is limited, which might be an additional explanation for the rather low H₂ concentrations in almost all of the GS.

Hydrogen sulfide reaches the rising fluids very likely by the same fluid-rock interaction processes. Additionally, reduction of magmatic SO₂ with H₂, or disproportionation of SO₂ into H₂S and H₂SO₄ has been reported [*Herzig et al.*, 1998].

6.3.4. Residual gases (Nitrogen, Argon, Helium)

The very low measured oxygen concentrations in the GS exclude contamination with air during handling, subsampling and storage of the subsamplers. Hence, the listed contents of nitrogen and argon in the Table 4 reflect the real concentration of these compounds in the hydrothermal fluids.

Sano et al. [2001] detect different sources of nitrogen for BAB hydrothermal systems, like the upper mantle and sedimentary material from the subducted tectonic plate. The N-content in the earth's mantle is assumed to be homogenous. Hence, the elevated N₂ content in the condensed phases of HK must be caused by a further source. A conceivable origin is the deposited material from the subducted Phillipine Sea Plate. It is enriched in inorganic nitrogen, which can turn to N₂ due to devolatilization processes. The subducted oceanic crust is also the origin of argon. It is the product of the radioactive decay of ⁴⁰K, which solely takes place in the crust. ³He/⁴He ratios of the condensed phases are between the ratios of crustal (0.01 – 0.1 R_{atm}; *Well et al.* [2001]) and mantle helium (~8 R_{atm}; *Well et al.* [2001]) and indicate a mixture of ⁴He-dominated crustal helium with an additional, but variable mantle-derived input of 'primordial' ³He.

7. Phase condition and behavior of the condensed phases

Results of Infochem Multiflash calculations regarding the influence of gas composition on phase condition, transformation, and fractionation during GH formation are presented in the following chapters. Various processes and calculation approaches were chosen to obtain a complete impression of the phase conditions in situ and possible phase change processes. These approaches base on processes observed during the SO 196-2 or earlier cruises (Fig. 23).

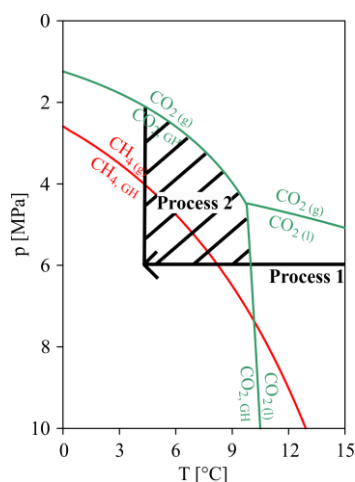


Fig. 23: Schematical illustration and calculation approaches of the phase conditions in situ and possible phase change processes. Process 1: sudden shrinkage and phase change into liquid. Process 2: emission within GHSZ (hatched area).

- Process 1: A gas bubble gets emitted by a hot vent and quenches due to fast cooling by contact with the cold seawater. The bubble changes into the liquid phase and hence collapses due to the suddenly increasing density. This process will occur directly after release into the water column, thus the calculations were performed with constant in situ pressure and various temperatures. Not all considered gas mixtures undergo this phase change under in situ conditions, hence the calculations were extended to a broad temperature range between minimum of -83°C and maximum 100°C to achieve almost all liquid-gas phase change temperatures.
- Process 2: A condensed phase gets emitted into the water column under p-T-conditions characteristic for the GHSZ. Questions arise, if the conditions allow the formation of GH. What is the maximum water temperature which allows the

formation under in situ pressure (calculation with constant pressure)? How high does the GHSZ reach when the condensed phase rises (calculation with decreasing pressure while the increase of the deep water temperature during the ascent is negligible and hence temperature is kept constant)?

- Process 3: An emitted condensed phase forms a GH layer and fractionates because the gas composition changes in comparison to the initial condensed phase.

The processes were calculated for gas mixtures with variable gas composition (Chapters 7.1.1 and 7.1.2) and for the measured gas compositions of the condensed phases from HK (Chapter 7.1.3). Some of the calculated data are limited to about 900 m because availability of sufficient data is limited to this water depth. Hence, these calculations are rather conceptual. Whenever possible, calculations were done with in situ pressure and temperature.

7.1. Theoretical considerations

7.1.1. Phase transformation between liquid and gaseous phase

Other than pure gases, phase transformation between liquid and gaseous phases of gas mixtures occur in a pressure-depending region between dew and bubble point. The dew point is defined as the temperature, at which dew forms (at a defined pressure), that means condensation of a gaseous phase begins. Analogous, the bubble point is the highest temperature to arise phase transformation from liquid to gas. At temperatures above the dew point, the gas mixture is in a homogenous gaseous phase. At temperatures below the bubble point it is in a homogenous liquid phase (shown as grey or blue shaded areas in the following figures). The region between both dew and bubble point curves are characterized by a mixture of both phases ('2-phase region').

Condensed phases from HK contain a mixture of diverse gas components, which influence the phase transformation in different or even divergent ways. Due to the complexity, each gas component is reviewed individually in dependency of its concentration hereafter.

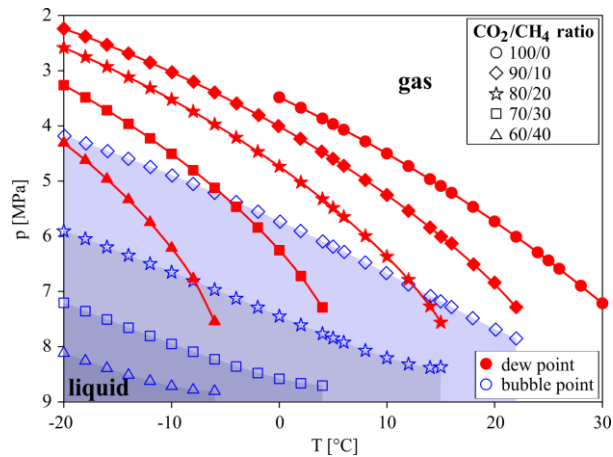


Fig. 24: Dew (red marks) and bubble point curves (blue marks) of gas mixtures with changing $\text{CO}_2 / \text{CH}_4$ ratio. The blue shaded areas below the bubble point curves indicate the p-T-conditions for a homogenous liquid phase.

Phase transformation behavior of a gas mixture, that consists of both main components carbon dioxide and methane, is strongly dependent on their ratio. The changes in dew and bubble point in dependency of the ratio of both gases are shown in Fig. 24, ranging from a pure CO_2 phase to a mixture of 60 % CO_2 and 40 % CH_4 . The dew point curve becomes steeper with increasing amount of methane, hence the influence of the pressure on the dew point increases. The bubble point curve in contrast becomes flatter, hence the bubble point is less dependent on the pressure.

At a fixed water temperature of 4°C , the liquid phase of a CO_2 droplet with 10 % methane is stable up to a water depth of 621 m (6.1 MPa) until the bubble point is reached, meaning the gas transformation into the gaseous phase would begin. In contrast, the bubble point of a droplet with a CO_2/CH_4 ratio of 70/30 is already reached at a pressure of 8.7 MPa (888 m water depth).

At a fixed release depth, the increase of methane causes a shift of the dew point towards lower temperatures. To condensate a gaseous mixture, the fluid has to be considerably colder. At 7 MPa, the dew point varies with the phase composition: about 29°C (pure CO_2 phase), about 21°C (CO_2/CH_4 ratio of 90/10), about 13°C (80/20), and about 5°C (70/30). If CH_4 accounts for more than 40 % of the gas mixture, it even impedes the formation of a liquid phase in aqueous environments at that pressure, because the dew point is lowered to temperatures far below 0°C , which is out of the naturally possible range.

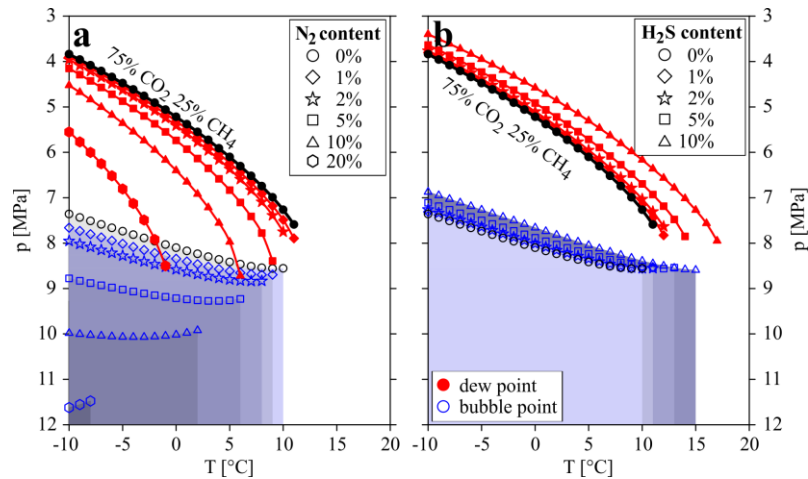


Fig. 25: Dew (red marks) and bubble point curves (blue marks) of gas mixtures with changing (a) nitrogen and (b) hydrogen sulfide content at a constant carbon dioxide/methane ratio of 3:1. The blue shaded areas below the bubble point curves indicate the p-T-conditions for a homogenous liquid phase.

The presence of nitrogen in a CO_2/CH_4 gas mixture enhances this effect of destabilization of the liquid phase even more. In Fig. 25a the change of the dew and bubble point curve is shown for a carbon dioxide/methane mixture with a fixed ratio of 3:1 with increasing N_2 concentration from 0 to 20 %. Similar to CH_4 , the enhancement of nitrogen steepens the dew point curve and flattens the bubble point curve. At a fixed pressure of 7 MPa, the dew point decreases from about 9°C in the absence of nitrogen to about 5°C at 5 % N_2 and about 2°C at 10 % N_2 content. At even higher concentrations, the formation of a liquid phase can be excluded under natural marine conditions. At a fixed water temperature of 4°C the bubble point of a nitrogen-free droplet is up to 853 m water depth (8.4 MPa). A N_2 content of 2 % enhances the pressure to 8.9 MPa (894 m). The formation of a liquid phase for gas mixtures containing 20 % N_2 is impossible at water temperatures of 4°C .

Hydrogen sulfide has an opposite effect on the stability of the liquid phase of a CO_2/CH_4 gas mixture, however it is not that pronounced (Fig. 25b). Increase of H_2S content causes a shift of the dew and bubble point curve to higher temperatures and lower pressures. Hence, the region in which the liquid phase is stable, is bigger. Even at higher vent temperatures or lower release depths, the emission of droplets is likely.

7.1.2. Formation of gas hydrates

GH formation and stability is strongly influenced by the gas components of the initial gas mixture incorporated into the GH lattice. The gas type or the combination of different trace gases define whether a GH is formed or if it dissociates at higher or lower temperature [Sloan and Koh, 2008].

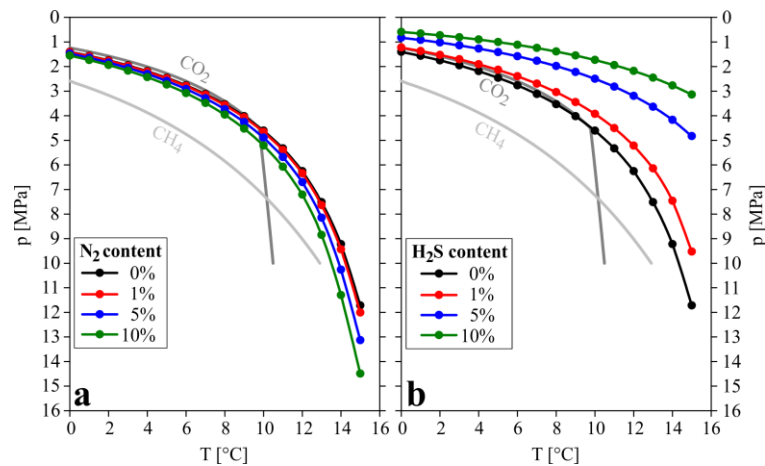


Fig. 26: GH phase boundary of gas mixtures with changing (a) nitrogen and (b) hydrogen sulfide content at a constant carbon dioxide/methane ratio of 3:1. Curves from pure carbon dioxide (dark grey) and methane hydrates (light grey) are also shown, calculated by usage of the software CSMGem.

Offset of the GH phase boundary, that is caused by varying concentrations of stabilizing and destabilizing gas components, are shown in Fig. 26. The curves for a gas mixture of carbon dioxide and methane with a ratio of 3:1 (black curves in both figures) differ considerably from the pure gases. In the low temperature range, the similarity to the pure CO₂ still remains, however the GH phase boundary is slightly flatter and shifted towards higher pressures, closer to the curve of pure methane. Even at slightly elevated temperatures, the GH phase boundary of the CO₂-CH₄-mixture steadily decreases up to high pressures. It shows no sharp bend like the curve of pure CO₂ at about 10°C.

The addition of nitrogen into this gas mixture promotes a shift of the GH phase boundary to higher pressure (Fig. 26a). N₂ is a poor hydrate former, it rather destabilizes the GH lattice and causes an offset to higher pressures and lower temperatures, the conditions to form GH become more extreme. However, even highly elevated concentrations of nitrogen have only a limited effect. At a pressure of 7 MPa,

the temperature of the GH phase boundary varies only slightly. A pure CO₂-CH₄-gas mixture (ratio 3:1) is stable up to temperatures of about 12.5°C. The addition of 10 % nitrogen reduces this value only by half a degree to about 12°C. At a water temperature of 4°C the GH phase boundary of a nitrogen-free condensed phase is 2.2 MPa (223 m). The addition of 10 % nitrogen decreases the value to 2.4 MPa (248 m). For comparison: the GH phase boundary is about 2 MPa for pure CO₂ at a temperature of 4°C, for pure methane it is already 3.9 MPa.

A totally different effect on the GH phase boundary is caused by the GH stabilizing hydrogen sulfide. Addition of H₂S causes a shift into the direction of lower pressures and higher temperatures with wider distances between the individual curves (Fig. 26b). The pressure-temperature range of the GHSZ is thus strongly enlarged. Hydrogen sulfide molecules are built into GH cages of the structural type I, just like CO₂ and CH₄. The more H₂S is present in the initial gas mixture the more GH cages are filled, which promotes the stability of the GH cluster. At a pressure of 7 MPa, the temperature of the GH phase boundary exceeds 15°C at a H₂S content as low as 5 %. At 4°C the GH phase boundary is 1.3 MPa (129 m). A GH coated condensed phase with 10 % H₂S can be formed up to a water depth of 92 m (0.9 MPa).

Not only stability, but also the composition of the GH (amount of each substance incorporated into the lattice as guest molecules) is influenced by the initial gas mixture composition. Hydrate formation from the gas phase results in gas fractionation, i.e. the mole fraction of the gas molecules in the initial gas phase can considerably deviate from that of the condensed phase. In order to investigate gas fractionation during this process, the formation of a GH was simulated by calculating the hydrate composition of the hydrate phase when a minimal amount of water is allowed to get in contact to a large amount of the gas mixture.

Water constitutes the highest amount of substance in the GH lattice. The dominance of this compound was expected, because the molar ratio between water and the gases, which form GH of structural type I (CO₂, CH₄, H₂S), is in the order of 1 : 5.75. For nitrogen, which is co-included in GH of structure II, the ratio is 1 : 5.67 [Sloan and

Koh, 2008]. Hence, for further investigations the molar fractions of the residual gas components are used in order to enable comparability of the gas mixtures and comprehensibility of the fractionation processes.

The distribution of the component changes with increasing nitrogen and hydrogen sulfide content is illustrated in Fig. 27 at a constant pressure of 15.271 MPa (1,517 m water depth, approximate depth of the sites emitting condensed phases at HK) and displayed in Table 5, exemplary for 4°C.

Table 5: Mole fraction of the gas components of a condensed phase and corresponding sI hydrate with increasing N₂ or H₂S amount at a fixed CO₂ : CH₄ ratio of 3 : 1 in the initial condensed phase. Data are exemplary for 4°C and 15.271 MPa.

	condensed phase	sI hydrate	
		N ₂ incorporation	H ₂ S incorporation
0 % N ₂ /H ₂ S	25,0 % CH ₄ 75,0 % CO ₂	41,7 % CH ₄ 58,3 % CO ₂	
1 % N ₂ /H ₂ S	24,8 % CH ₄ 74,2 % CO ₂ 1,0 % N ₂ /H ₂ S	40,9 % CH ₄ 58,4 % CO ₂ 0,7 % N ₂	39,2 % CH ₄ 54,9 % CO ₂ 5,9 % H ₂ S
5 % N ₂ /H ₂ S	23,8 % CH ₄ 71,2 % CO ₂ 5,0 % N ₂ /H ₂ S	37,9 % CH ₄ 59,0 % CO ₂ 3,1 % N ₂	31,8 % CH ₄ 44,7 % CO ₂ 23,5 % H ₂ S
10 % N ₂ /H ₂ S	22,5 % CH ₄ 67,5 % CO ₂ 10,0 % N ₂ /H ₂ S	34,5 % CH ₄ 59,8 % CO ₂ 5,7 % N ₂	26,2 % CH ₄ 36,5 % CO ₂ 37,3 % H ₂ S

The formation of a GH from a condensed phase of only CH₄ and CO₂ leads to an enrichment of CH₄ relative to CO₂ in comparison to the initial condensed phase. For the exemplary conditions from Table 5 the CO₂ : CH₄ ratio decreases from 3 : 1 to 1.4 : 1.

The presence of N₂ in the hydrate-building condensed phase slightly increases the CO₂ : CH₄ ratio up to 1.7 : 1 for 10 % nitrogen content. The nitrogen uptake influences the consumption of the GH insofar as the incorporation of mainly CH₄ into the GH is reduced, but not of CO₂. The mole fraction of nitrogen in the GH is low and even below the percentage amount in the initial gas mixture. Reason for this process is that the GH can only host a limited number of lattice destabilizing molecules. Hence, the nitrogen uptake is suppressed and the mole fraction of the poor GH former N₂ is

low in the GH. The remaining condensed phase after the formation of the GH will be strongly depleted in carbon dioxide, in methane to a lesser extent and enriched with nitrogen compared to the initial gas mixture.

In contrary, the uptake of H₂S into the GH is preferred. The higher the H₂S concentration in the initial gas mixture, the higher its relative amount in the gas hydrate lattice (Table 5). The amount of both guest molecules CO₂ and CH₄ decrease accordingly, while the CO₂ : CH₄ ratio remains constant. H₂S more likely competes with the GH cages trapped with CO₂, hence CO₂ is more suppressed than CH₄ and the incorporation into the GH of both gases CH₄ and CO₂ is reduced.

The temperature dependency of the individual components in the GH is shown in Fig. 27. The mole fraction of methane decreases by about 3 to 5 % between 0 and 15°C, whereas carbon dioxide increases by the same amount. The mole fraction of nitrogen decreases by almost a fifth, the amount of hydrogen sulfide in the GH lattice increases very slightly and is almost stable in this temperature range. With increasing temperature the formed GH shifts closer to its GH phase boundary. Hence, the GH tends to incorporate more of the best stabilizing compounds CO₂ and H₂S.

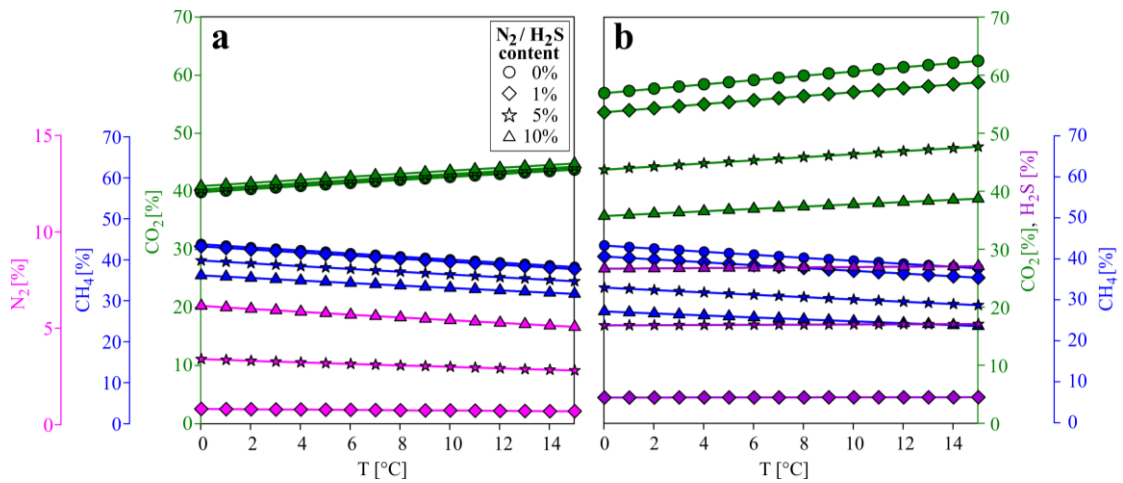


Fig. 27: Mole fraction of the components in the GH lattice formed out of a gas mixture with changing (a) nitrogen and (b) hydrogen sulfide content at a constant carbon dioxide/methane ratio of 3:1. Compounds considered are CO₂ (green), CH₄ (blue), N₂ (pink) and H₂S (dark pink). Note the different scales of the components, chosen for better clarity.

7.1.3. Phase behavior calculated for sample composition

The previous chapters focused on the influence of only one added component (hydrogen sulfide or nitrogen) on the dew and bubble point and the GH phase boundary. As an example of the interaction of all four gas components, calculations for dive 202, GS 3 (fraction 1) are shown in Fig. 28. The sample has a $\text{CO}_2 : \text{CH}_4$ ratio of about 3 : 1 and is highly comparable to the theoretical calculations. The nitrogen content is 2.9 %, the hydrogen sulfide content is 0.7 % in this fraction (Table 4).

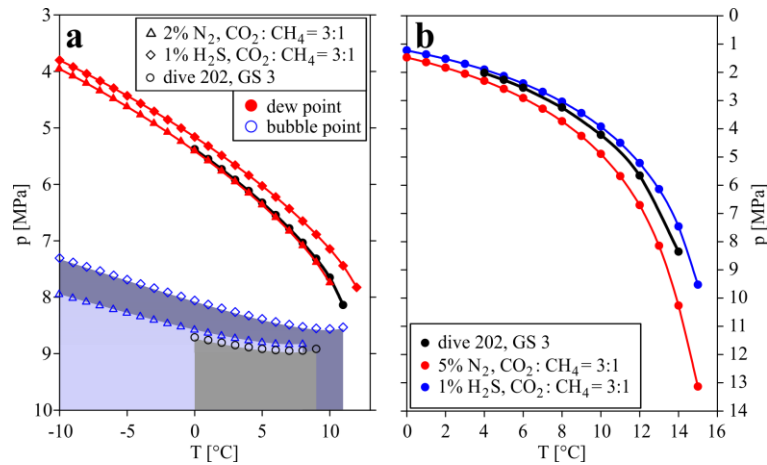


Fig. 28: (a) Dew (filled marks) and bubble point curves (empty marks) of gas mixtures with 2 % nitrogen (triangle) and 1 % hydrogen sulfide content (diamond) at a constant carbon dioxide/methane ratio of 3:1 in comparison to fraction 1 of dive 202, GS 3 (black circles). The blue and grey shaded areas below the bubble point curves indicate the p-T-conditions for a homogenous liquid phase. (b) GH phase boundary of the sample in comparison to gas mixtures with 5 % nitrogen (red) and 1 % hydrogen sulfide content (blue).

Fig. 28a shows the dew and bubble point curves of the sample in comparison to the calculated 3-component-gas mixtures with 2 % nitrogen (triangle marks) and 1 % hydrogen sulfide (diamond marks). The dew point curve of GS 3 is located between both 3-component-curves as expected, however tends towards the nitrogen curve. One reason is that the 2.9 % of nitrogen in the sample are slightly higher than in the depicted curve of 2 % N₂. Because N₂ has a very strong influence on the dew point (Fig. 25a), the increase of nitrogen content in the gas mixture of only 0.9 % causes a significant shift of the dew point curve. Another reason is that the impact of H₂S on the dew point is rather low (Fig. 25b). A shift of the dew point curve towards the hydrogen sulfide curve is only limited and almost negligible due to the very dominant

influence of nitrogen. The bubble point curve of GS 3 is located even below the 2 % nitrogen curve, because the influence of nitrogen on the bubble point is higher. The very low concentration of hydrogen sulfide of 0.7 % in the sample hardly affects the shift of the curve.

In contrast to the dew and bubble points, the GH stabilizing hydrogen sulfide has a major influence on the GH phase boundary, far larger than the poor hydrate former nitrogen. The curve of the GS 3 (Fig. 28b) resembles the curve of the 3 : 1 mixture with 1 % H₂S more closely.

Of course, the calculated values for the liquid-gaseous phase shift are purely theoretical. They assume a constancy of the gas composition of the condensed phase between the depth of emission and the bubble point curve, which is a rising height of more than 600 m. The condensed phase of dive 202, GS 3 is released into the water column at a water depth of 1,524 m, hence within the GHSZ. A GH skin will be formed around the condensed phase very fast and the gas composition of the condensed phase will change insofar that the hydrate stabilizing compounds are depleted because they are preferentially incorporated into the GH, out of which they will dissolve. During the long ascent of the coated condensed phase, dissolution processes out of the GH lattice and potentially also between the condensed phase and seawater occur, leading to further changes in gas composition of the condensed phase and hence different phase shift points. The curves in Fig. 28 are intended exclusively as an illustration of the interaction between the four gas components in comparison to the results of Chapter 7.1.1 and 7.1.2 for the 3-compound-phases of carbon dioxide and methane, and hydrogen sulfide and nitrogen, respectively.

These interactions can also be demonstrated for dive 202, GS 4. Fig. 29 shows the curves of the dew and bubble points and of the GH phase boundary of fractions 1 and 3 of this sample. Both fractions differ regarding the CO₂ : CH₄ ratio (fraction 1 with 5.6 : 1; fraction 3 with 6.4 : 1) and regarding the H₂S content (1.9 % and 0.9 %, respectively), see Table 4. The concentration of nitrogen is equal in both fractions. For

comparison, the curves of two hydrogen sulfide concentrations (1 and 2 % H₂S) at a constant CO₂ : CH₄ ratio of 3 : 1 are demonstrated in Fig. 29.

The shift of the dew and bubble point curves of GS 4 to the upper-right area of the diagram is apparent, in contrast to both comparison curves. This shift means an enlargement of the stability zone of the liquid phase to lower pressures and higher temperatures. These very pronounced shifts of both dew and bubble point curves are very likely caused by the increased CO₂/CH₄ ratio of the sample (Chapter 7.1.1). It is about twice as high as the ratio of the comparison calculations.

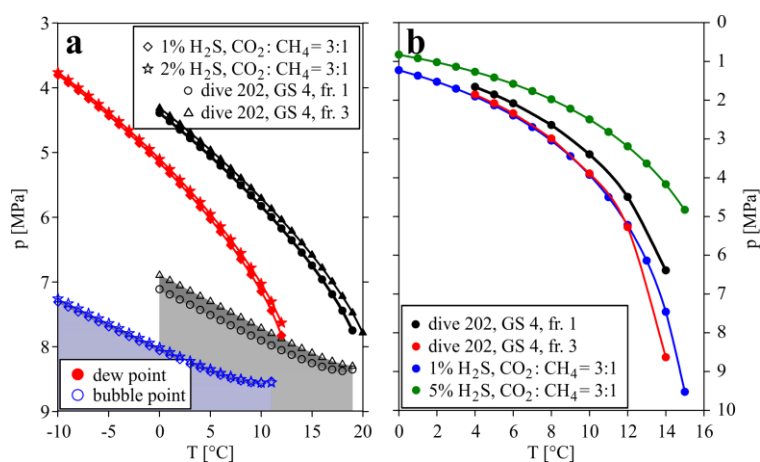


Fig. 29: (a) Dew (filled marks) and bubble point curves (empty marks) of gas mixtures with 1 and 2 % hydrogen sulfide content at a constant carbon dioxide/methane ratio of 3:1 in comparison to fraction 1 and 3 of dive 202, GS 4 (black marks). The blue and grey shaded areas below the bubble point curves indicate the p-T-conditions for a homogenous liquid phase. (b) GH phase boundary of the fractions from the sample in comparison to gas mixtures with 1 and 5 % hydrogen sulfide content (blue).

The difference between the dew and bubble point curves of both fractions is rather small, because both fractions have a similar gas composition. The curves from fraction 3 are shifted towards lower pressures compared to fraction 1, very likely caused by the increase of the CO₂/CH₄ ratio. The influence of hydrogen sulfide is negligible. A decrease of the H₂S content by 1 % causes a slight shift in the opposite direction as can be seen in both comparison curves (Fig. 29a).

Hydrogen sulfide has a bigger influence on the GH phase boundary. In comparison to GS 3, the GH phase boundary curve of GS 4 is shifted towards lower pressures and higher temperatures, by others due to the higher H₂S concentration, and increases the

GHSZ. The decrease of H₂S between fraction 1 and fraction 3 shifts the curve into the opposite direction and causes a reduction of the GHSZ. Thereby, the GH phase boundary curve of fraction 3 is very similar to the 1 % H₂S curve. At temperatures above 12°C, the negative slope of the curve from this sample increases and both curves enlarge the distance from each other. Only from this point on, the greater contribution of CO₂ in the sample appears to cause the sharp bend of the curve, that is characteristic for pure carbon dioxide.

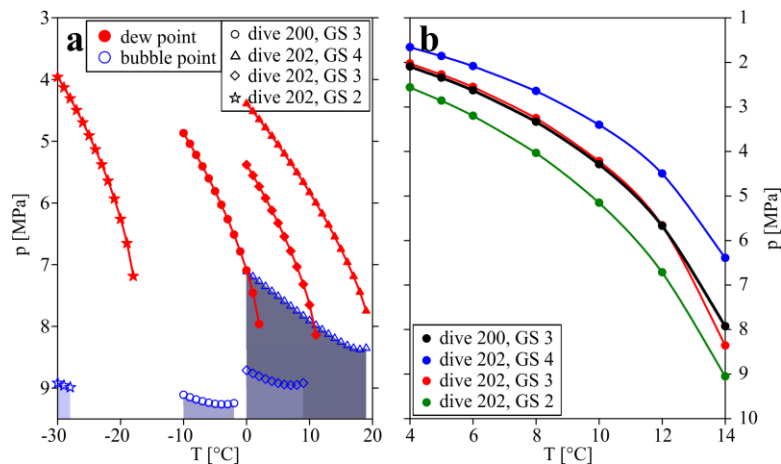


Fig. 30: (a) Dew (red) and bubble point curves (blue) of the first fractions of the dive 200, GS 3 and dive 202, GS 2 to 4. The blue shaded areas below the bubble point curves indicate the p-T-conditions for a homogenous liquid phase. (b) GH phase boundary of these samples.

In Fig. 30a the dew and bubble point curves of all four GS are summarized, with substantial differences between the individual samples. The curves from dive 202, GS 2 are found in the lowest temperature range. For this gas composition, the pressure and temperature range for which the liquid phase is stable, is relatively narrow. Natural marine pressure and temperature conditions are clearly outside this range. The gas mixture is in the gaseous aggregate phase at the time of emission. The formation of a liquid phase is even impossible during the ascent. For dive 200, GS 3 there is also only a low probability to get emitted in a liquid aggregate phase or to liquefy during the ascent through the water column. Extrapolations of the polynomial curves for the dew and bubble point cause an intersection at a temperature of about 3.6°C (data not shown). Water temperatures at this low level are rare. In case of the emission of a

liquid phase or the formation of a droplet in the water column due to suitable conditions, the life time of this phase is supposed to be short.

Unlike the two previously discussed samples, the liquid phase stability zones of dive 202, GS 3 and 4 are bigger. Even emission at elevated water temperatures allows for the formation of a liquid phase.

The direct dependency of the dew points on the gas composition is visible in Fig. 30a. The dew points of the GS increase in the following order: dive 202, GS 2 < dive 200, GS 3 < dive 202, GS 3 < dive 202, GS 4 (from left to right in Fig. 30a). The CO₂/CH₄ ratio as well as the H₂S content increases and the N₂ content decreases in exactly the same order in the GS (Table 4). As described in Chapter 7.1.1 and shown in Fig. 24 and Fig. 25 the dew point is mostly influenced by the CO₂-CH₄ ratio. The higher the amount of CO₂, the higher is the dew point. The CO₂-CH₄ ratio of the GS increases from 1 : 1.1 in dive 202, GS 2 over 1.9 : 1 (dive 200, GS 3) and 3.1 : 1 (dive 202, GS 3) to 5.6 : 1 in dive 202, GS 4. Hydrogen sulfide has the same impact, but to a considerably lesser extent. The H₂S concentration increases from 0.4 to 1.9 mole-% in the GS in about the same order. Nitrogen influences the dew point in the contrary way. Decrease of the nitrogen content promotes an increase of the dew point. Highest N₂ concentration is measured in dive 202, GS 2 and decreases continuously till dive 202, GS 4. Hence, the increasing or decreasing concentrations of the compounds and the dew points of the GS are in a direct proportionality. The different distances between the dew point curves are caused by the combination of the individual compounds and their diverse impact.

In Fig. 30b the GH phase boundaries of all four GS are shown. The curves of the GS are arranged in the same order in this p-T-diagram as the dew points in Fig. 30a - from the bottom to the top. The curve from dive 202, GS 2 is located furthest towards high pressures and low temperatures and hence has the narrowest GHSZ. In contrast, the dive 202, GS 4 is the sample with the widest range of the GHSZ. At an ambient water temperature of 4°C, the GH phase boundaries of both samples differ by about 90 m water depth. At a water temperature of 14°C the difference increases to about 270 m.

However, the p-T-conditions at the vents of both condensed phases are well within the GHSZ. The formation of a GH skin is very likely in both cases, whereas the phase change occurs from gaseous to solid (GH) for GS 2 and liquid to solid (GH) for GS 4 due to the previously described shift of both dew point curves.

The position of the GH boundary curves in the diagram are also influenced by the gas composition of the mixture. Especially hydrogen sulfide has a great impact. This is reflected in the similar curve progression of both GS 3 from dives 200 and 202 with their almost equal H₂S concentration. Also the residual three gas components affect the slope and the position of the curves. The higher nitrogen concentration of dive 200, GS 3 might be the crucial factor, which explains why this curve is located slightly below the sample from dive 202, GS 3.

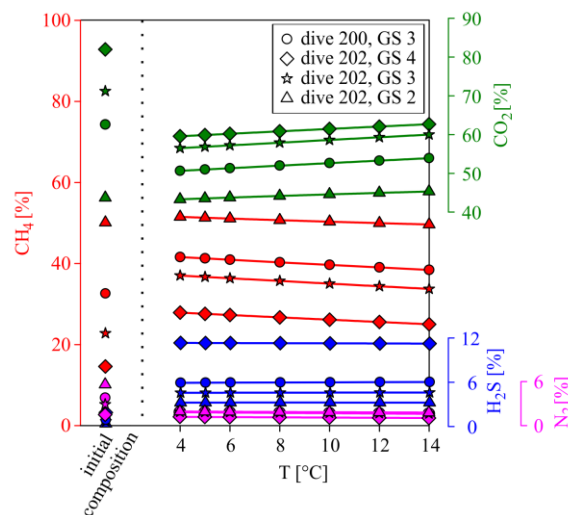


Fig. 31: Mole fraction of the components in the GH formed out of the gas mixtures of the different GS as a function of temperature. Compounds considered are CH₄ (red), CO₂ (green), H₂S (blue), and N₂ (pink). The left part of the diagram shows the initial gas composition before GH formation.

The composition of the GH, according to the different initial composition of the condensed phase, is shown in Fig. 31. The comparison of both main components CO₂ and CH₄ regarding their relative concentration between the initial condensed phase and the GH, reveals big differences especially for the CO₂-dominated samples. The amount of carbon dioxide decreases strongly, whereas the mole fraction of methane increases significantly. Hence, the CO₂/CH₄ ratio decreases considerably, even though CO₂ remains the dominant compound in the GH. The increase of the mole fraction of

methane in the GH in comparison to the initial sample implies a relative depletion in the remaining condensed phase. A condensed phase with an elevated CO_2/CH_4 ratio remains at the phase boundary to the GH skin. Nitrogen as a poor GH former enriches in the condensed phase, whereas the mole fraction of hydrogen sulfide increases in the GH by a factor of up to 8 in comparison to the initial composition of the condensed phase, because of its stabilization effect on the GH cluster.

Almost all components display the same dependency of the temperature, as presented in Fig. 27. The higher the temperature, the more CO_2 and H_2S are incorporated into the GH lattice, whereas methane and nitrogen concentrations decrease in a varying extent. The increase of temperature leads to a decrease of thermodynamic fractionation, hence causes a convergence of the CO_2/CH_4 ratio towards the initial value. The only non- CO_2 -dominated sample (dive 202, GS 2) behaves similar, whereby the methane remains the dominant compound over the entire investigated temperature range. At the lowermost calculated temperature of 4°C , the CO_2/CH_4 ratio is also below the ratio of the initial condensed phase. The increase of this ratio due to the inverse trend of carbon dioxide and methane concentrations with increasing temperature leads to a higher CO_2/CH_4 ratio than the initial ratio at 10°C , already.

7.1.4. Possible phase change and fractionation processes

The data and results of the previous chapters provide insights about possible phase change and fractionation processes under in situ pressure and temperature conditions.

- Process 1: Gas bubbles which are emitted by a hot vent can quench, liquefy and hence collapse due to fast cooling by contact with the cold seawater. The temperature of the ambient water has to be cooler than the dew point of the gas mixture. Methane and nitrogen influence the dew point insofar that the dew point shifts into the direction of colder temperatures. Hence, elevated concentrations of both compounds can reduce the p-T-range for liquefaction, hence it is not encountered under in situ conditions.
- Process 2: The formation of a GH skin around condensed phases which are emitted by deep cold vents, should be possible in general under in situ conditions.

But also the emission from hot vents does not prevent the formation. Cold ambient seawater leads to fast cooling of the emitted fluids, hence the condensed phase reaches the temperature of the GH phase boundary relatively soon after emission. An elevated nitrogen content in the condensed phase shifts the phase boundary into the direction of colder temperatures and hence reduces the area of the GHSZ. The formation of GH is possible for all condensed phases, even if they cannot obtain the p-T-condition of the liquid aggregate state due their gas composition.

- Process 3: The formation of GH leads to fractionation between the initial, remaining condensed phase, and GH. GH stabilizing compounds like CO₂, CH₄, and H₂S are integrated preferentially in the lattice, however with different privilege. These compounds enrich in the GH in comparison to the initial condensed phase, and the remaining condensed phase gets depleted. Poor GH-forming compounds like N₂ can be incorporated into the GH lattice only to a limited extent because of their destabilizing influence. These compounds enrich in the remaining condensed phase. The formation of GH at the boundary between condensed phase and ambient water influences the solubility of the individual components which in turn effects the gas composition [Rehder *et al.*, 2004].

7.2. Conclusions on phase behavior under in situ conditions

The measurements of vent temperature and the visual studies at the emission sites (Chapter 6.1), paired with analysis of the gas composition (Chapter 6.2) and its development with decreasing pressure, as well as theoretical calculations via Infochem Multiflash (Chapter 7.1) help determining the aggregate state of the emitted condensed phases in situ. Additionally in this chapter, results from experiments onboard ('p/T-expansion experiment', Chapter 4.2.2), as well as from further simulations with the Infochem Multiflash software are considered. The expected development of the density of the condensed phase as a function of temperature at their specific pressure conditions at the emission sites is illustrated in Fig. 32. The diagram indicates the temperature range, where liquid or gaseous phase can persist at the in situ pressure. Unfortunately, only limited data are available for dive 200, GS 3

due to a mistake in the manual data input. Still, it is apparent, that its curve is located below the curve from dive 202, GS 3.

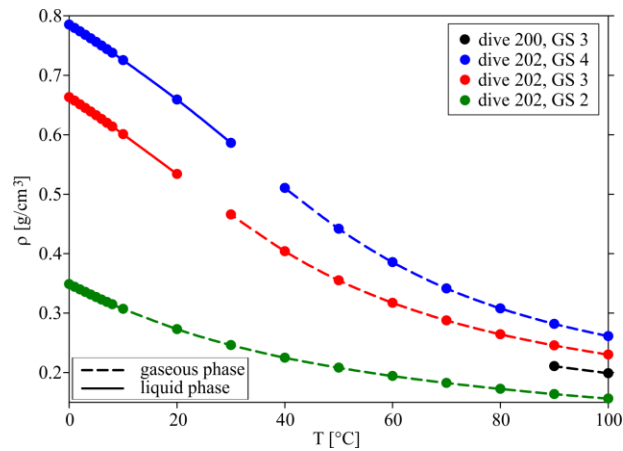


Fig. 32: Development of the density as a function of temperature for the gaseous (dotted line), as well as liquid phase (solid line). Only limited data are available for dive 200, GS 3.

7.2.1. Dive 200, GS 3

The change in concentration with decreasing inner pressure of the two dominant gas compounds methane and carbon dioxide in the GS are described in Fig. 33. Despite a pressure difference of more than 40 bar, the gas composition of the fractions 1 and 3 of GS 3 are almost identical (Table 4). The consistency of the gas composition with decreasing pressure indicates the presence of only one homogenous phase in the GS. A heterogenous 2-phase system of liquid and gas as well as the presence of water in the GS would have caused a change of the gas composition between the individual fractions due to different enrichment tendency in the liquid phases and delayed outgassing due to pressure decrease.

Video records of the emission site show small emissions of condensed phase, most likely bubbles, because of their variability in shape, buoyancy, and oscillation. The bubbles are non-coated with GH, because of the prevailing warm fluid temperatures. During the ascent of the emitted condensed phase, a GH skin is formed very quickly visible in their change in oscillation and shape. The bubbles became slightly oval with a solid structure and rotated rigidly.

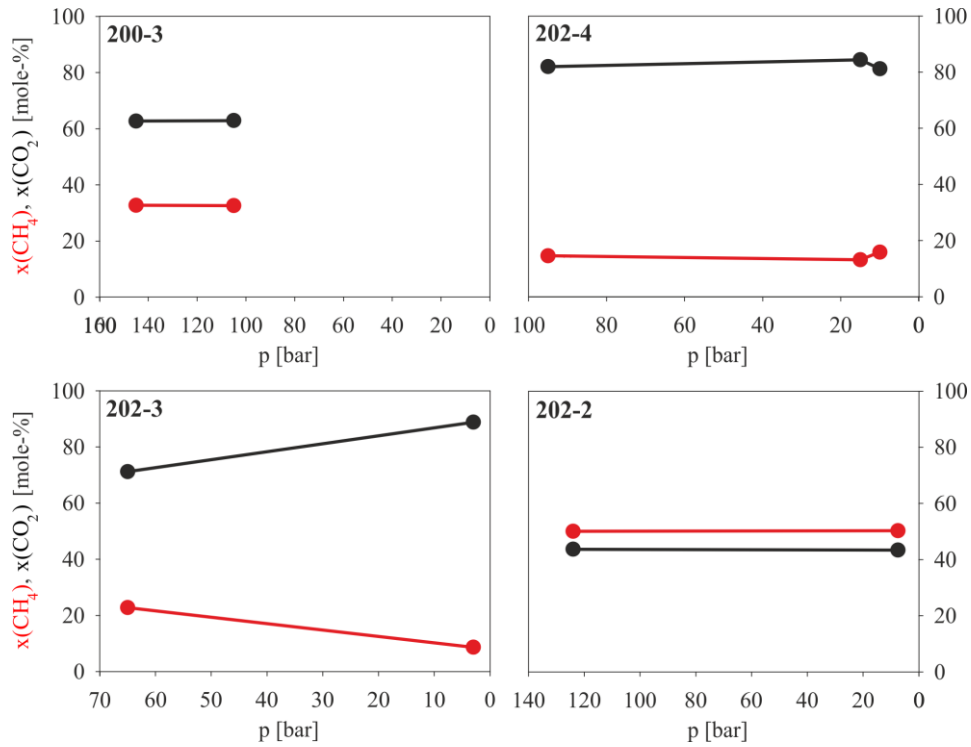


Fig. 33: Development of the mole fraction of the two dominating gas compounds methane (red) and CO_2 (black) in the GS with decreasing inner pressure.

Dew and bubble point curves of the sample indicate the stability of a liquid phase only at very low temperatures (Fig. 30). The vent temperature at the emission site is 50°C , hence it is very likely that a gaseous phase is emitted. If the gas bubbles are removed from the vent induced warm water area, condensation occurs due to cooling below the temperature limit, however it is accompanied by the formation of a GH skin. Accumulation of coated bubbles delays a fast and complete cooling of the condensed phase, which is confirmed by an experiment with the ‘T-corer’ at this vent (Chapter 4.2.4). For this experiment some milliliter of the rising condensed phase were collected in the device. A GH skin formed instantaneously around the bubbles. The inner temperature of the GH accumulation remained 40°C , which is still close to the 50°C vent temperature and still in the gaseous phase stability range. Because the collected bubbles in the GS are thought to behave equally, the collection of a homogenous, gaseous phase is very likely. The formation of the GH leads to variation in gas composition. The higher CO_2/CH_4 ratio of the GH skin compared to the initial gas mixture leads to a decrease of the CO_2/CH_4 ratio in the residual condensed phase.

The gas-liquid-phase boundary shifts towards lower temperatures and prevents the transformation into a liquid phase.

7.2.2. Dive 202, GS 2

The consistency of the gas composition of both fractions 1 and 3 from dive 202, GS 2 (Table 4) also hints to a homogenous phase. The fast rising velocity of $25 \text{ cm} \cdot \text{s}^{-1}$ on average and the behavior of the condensed phase point to the emission of gas bubbles, because droplets are thought to rise slower due to their higher density. The dew and bubble point calculations exclude the formation of a liquid phase at natural marine conditions. The density calculations at the prevailing pressure conditions support this conclusion (Fig. 32). Even at temperatures as low as 0°C , the condensed phase of this composition appears solely in a gaseous state. The ‘p/T-expansion experiment’ with the GS after subsampling of fraction 1 supports this conclusion as well (Fig. 34). At temperatures above 5°C , the inner pressure increases almost linearly. There is no indicator for the presence of a second liquid phase, which would cause a delayed and steeper increase of pressure.

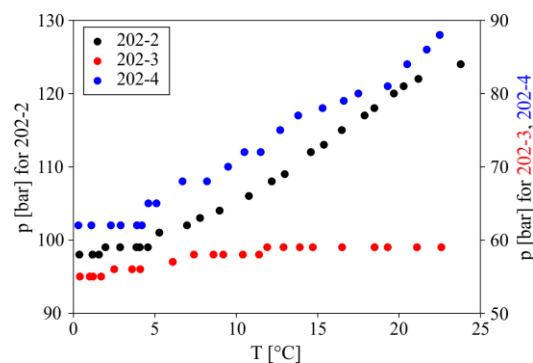


Fig. 34: Development of pressure inside the GS from dive 202 on temperature change by slow heating from 0 to 25°C (‘p/T-expansion experiment’).

7.2.3. Dive 202, GS 3

GS 3 of dive 202 is the first and only sample with strong variability between first and subsequent fraction concerning all gas components (Table 4). Inhomogeneity between the fractions hints to the presence of a liquid phase or a 2-phase mixture of gas and liquid in the GS at the time of subsampling onboard. Fraction 1 is characterized by high CO_2 and CH_4 concentrations. After subsampling of fraction 1, the sample was

allowed to expand in a high-volume vessel. Decompression led to a complete vaporization of the liquid phase into a homogeneous gaseous phase.

The video records of the rising fluids hint to the emission of droplets, because of the more spherical shape, minor oscillation and slower rising velocity of $22 \text{ cm} \cdot \text{s}^{-1}$ on average, which is a result of the greater viscosity and the higher density in comparison to bubbles. The vent temperature was not measured at this emission site, however the temperature sensor of the ROV didn't reveal an increase of water temperature during the time of investigation and sampling. Hence, there is no evidence for the emission of warm, but likely cold fluids. The density calculations reveal that the liquid state is preferred at temperatures below 20 or 30°C, taking into account the prevailing pressure conditions during emission (Fig. 32).

Results from the 'p/T-expansion experiment' indicate a homogenous liquid phase within the GS. The pressure difference between the starting temperature of 0°C and 25°C is almost negligible (Fig. 34). The liquid aggregate state is assumed to be stable throughout the entire temperature range, hence the pressure increase is limited. However, the measured pressure difference has a surprisingly small extent. The relatively low inner pressure might be an indicator for the presence of a liquid phase, which has a significant higher density than the gaseous phase (Fig. 32).

7.2.4. Dive 202, GS 4

All gas components of dive 202, GS 4 appear uniformly between the different fractions (Table 4), which leads to the assumption of the presence of a homogenous phase within the GS. Results from the Infochem Multiflash software point to the emission of a liquid phase, that is stable at temperatures of at least 30°C. A vent temperature of 5.2°C is measured, hence the emission of droplets seems very likely. However, neither magnitude nor development of pressure with increasing temperature during the 'p/T-expansion experiment' can give clear hints on the aggregate state in the GS. The inner pressure of 115 bar after sampling is much lower than the about 160 bar of both gaseous samples (dive 202, GS 2 and dive 200, GS 3), but not as low as the 84 bar of the presumable liquid sample in dive 202, GS 3. The increase of

pressure with temperature furthermore resembles the GS 2 (Fig. 34), which is likely gaseous.

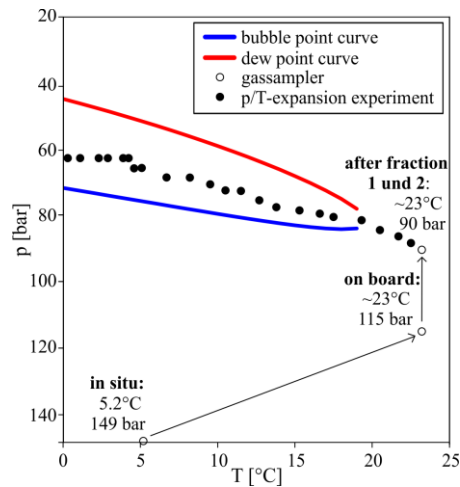


Fig. 35: Phase diagram for the gas composition of dive 202, GS 4. Open circles indicate the pressure and temperature conditions within the GS during sampling and first processing onboard. Collected parameters during ‘p/T-expansion experiments’ (filled circles) are located in the 2 phase region between bubble (red line) and dew point curve (blue line).

As shown for GS 3, the presence of a liquid phase causes a significant difference in gas composition between the fractions before and after decompression, because of different tendencies of the individual components to enrich in the liquid phase. A closer look at the data in fact shows such a difference between fraction 1 and 3, however it is small compared to GS 3. It is difficult to estimate, if this small difference is a sufficient indicator for the presence of a liquid phase in the GS. In this case, the decompression of the sample by expansion into the high-volume vessel should evaporate the liquid phase into a homogeneous gaseous phase, which is consistent in its composition. Fraction 4 however differs from fraction 3 and rather resembles the first fraction. The reason for this occurrence is not clear. The phase diagram in Fig. 35 shows a potential explanation of these various, partly contradictory observations. Sampling occurred at a temperature of 5.2°C, very likely in a liquid phase. On board, the GS and the condensed phase therein were warmed up to about 20 or 25°C. The data for this area of the phase diagram is poor, but it seems possible, that the sample was vaporized completely already at this stage. Hence it is likely that the GS contains a homogenous gaseous phase at this time. Subsampling of the first two fractions cause

a decrease of the inner pressure to 90 bar. The subsequent 'p/T-expansion experiment' steers the sample into the 2 phase region between bubble and dew point curve. It might be possible, that parts of the gaseous phase degenerate into the liquid state again during this experiment. It is also possible, that the sample had not been homogenized completely at the time of subsampling of fraction 3, which would cause a slightly different gas composition of this fraction.

7.2.5. Aggregate states of condensed phases

The phase diagram of the first fractions of all four GS is shown in Fig. 36. It summarizes the phase boundary between liquid and gaseous phase (dew and bubble point) and GH phase boundary. At the vent site of dive 202, GS 2, the gas bubbles are emitted with no opportunity of condensation to a liquid phase. The emission of a gaseous phase at the site of dive 200, GS 3 is also very likely due to the elevated vent temperature of 50°C. A phase shift due to cooling is possible, but there is no evidence for this process. Visual observations, theoretical calculations, as well as geochemical parameters lead to the presumption, that a liquid phase was collected into the dive 202, GS 3. At the vent from dive 202, GS 4, the formation of a liquid phase is in fact very likely at in situ conditions, however measurements and experiments onboard could not unambiguously confirm this. A 2-phase system within the GS is probable.

During their ascent, the condensed phases move out of the vent induced (partly warm) water area and in the GHSZ. Assuming a constant flux of the condensed phase over time, the mentioned values of 5 to 9 ml · min⁻¹ in combination with the measured CO₂ content translate to a CO₂ emission into the water column in the order of 10² mol · year⁻¹ · vent⁻¹, which is rather low compared to the estimated 10⁸ mol CO₂ · year⁻¹ · vent⁻¹ of the fluids at YK (Chapter 5.3).

Due to the formation of a GH skin it is possible, that the condensed phases rise higher through the water column before complete dissolution. This extends the influence of the geochemical signature beyond the lowermost 10 m assumed in Chapter 5.6. In principle, the rising height of the condensed phase is limited by the density of the GH coated phases in comparison to the ambient sea water. However, it is much more

likely that the condensed phases will dissolve completely during the ascent considerably before reaching these water depths, despite the thermodynamic stability of the CO₂ hydrates, because CO₂ is under-saturated in the ambient water (e.g. *Rehder et al. [2004], Bigalke et al. [2009]*).

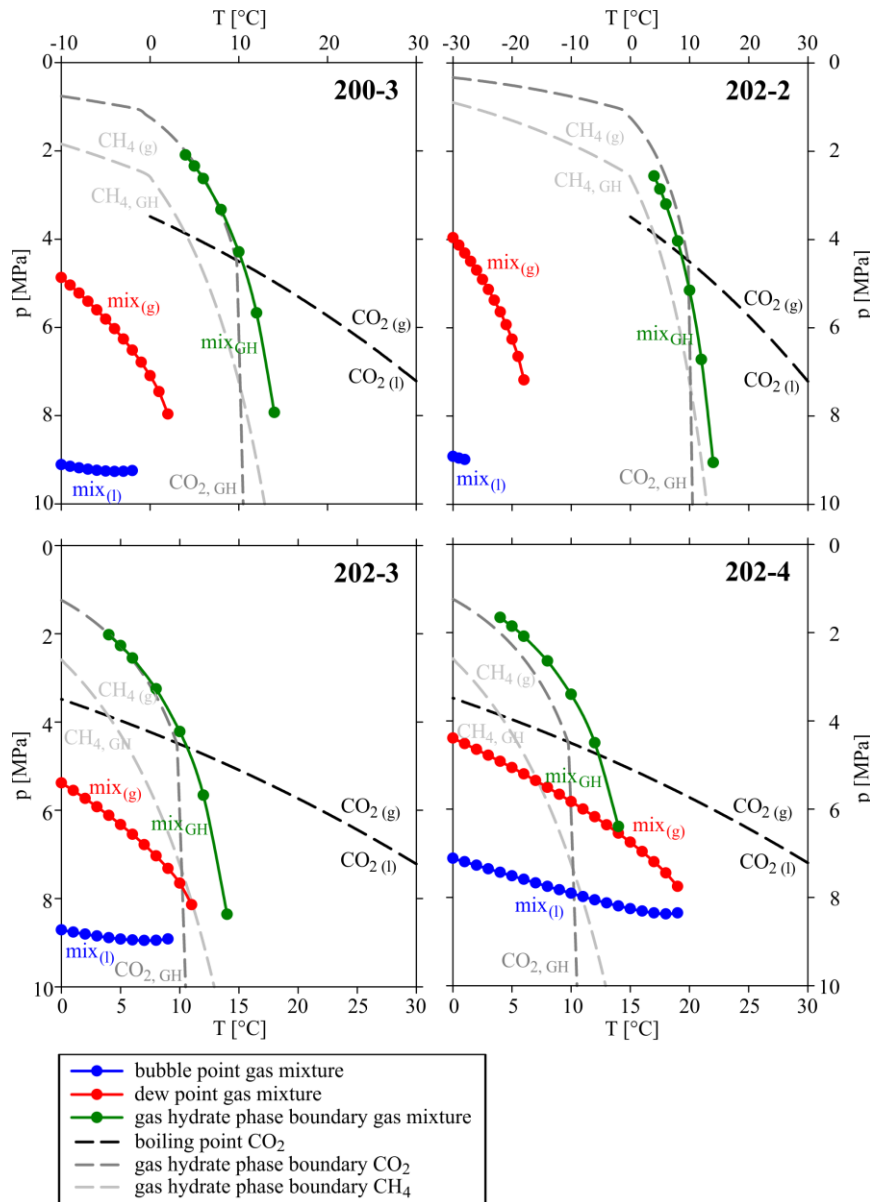


Fig. 36: Phase diagram of all four GS showing phase boundary between gaseous (g), liquid (l), and solid phase (GH - gas hydrate) of the gas mixture (mix), pure carbon dioxide (CO₂), and pure methane (CH₄).

7.3. Potential processes inducing geochemical variability

The last fraction of all GS is supposed to represent the initial gas composition of the emitted condensed phase. They show a uniform $\delta^{13}\text{C}$ isotopy of both main components CO₂ and CH₄ (Table 4). These carbon isotopic ratios are in about the

range of values, which were measured in hot fluids and in the water column close to the main active vents in the center of the HK in earlier campaigns [Kawagucci, 2015; Yamamoto *et al.*, 2015]. The condensed phases originate from the hydrothermal fluids, based on the conclusions from Konno *et al.* [2006], who also found a carbon isotopic relationship between liquid phase and hydrothermal fluids in the YK research area. Hence, all four gassamples from HK are likely to have a common source. However, the gas compositions vary between them considerably, although the vents are situated in relatively close distance. The variability will be caused by ‘secondary modification processes’, whereby different phases and different forms of these processes seem to occur. For example, the emission sites of dive 202, GS 3 and 4 are located less than 20 m apart. The condensed phases of both samples show a similar composition, which differ widely from the residual two samples. This indicates the occurrence of a fundamental modification process. Nonetheless at least one further process will take place close to the emission sites, which accounts for the small differences between both samples despite their close proximity.

A closer look at the path of the rising hydrothermal fluids through the discharge zone reveals possible processes. The homogenous, gas-rich, boiling fluids rise buoyantly towards the seafloor, because of their low density. The formation of the condensed phases is assumed to be caused by oversaturation and degassing of the gas-rich fluids due to pressure relief, or condensation of the dissolved gases due to cooling. First phase partitioning processes can occur due to separation of vapor or steam at temperatures above 100°C and gas exsolution of specific gas species as a consequence of supersaturation [Barry *et al.*, 2012]. During the further ascent, a variety of different fractionation processes can cause geochemical variability dependent on magnitude and velocity of cooling of the condensed phases.

Four different possible phase separation or fractionation processes are shown in Fig. 37. Process 1 describes the cooling process of the rising condensed phase to temperatures above the dew point of the gas mixture, hence causing the formation and emission of gas bubbles. Fractionation due to a phase shift into liquid or the formation

of GH is not expected at these fluid temperatures. Condensed phases generated by this process might reflect a gas composition close to the initial composition of the hydrothermal fluids.

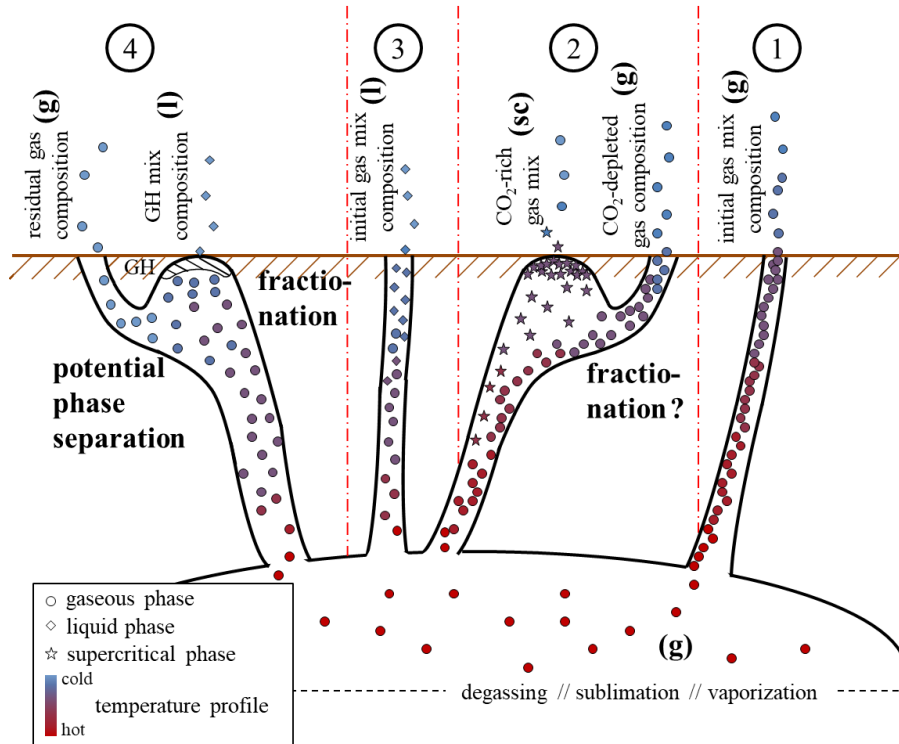


Fig. 37: Possible phase transformation, separation and fractionation processes proceeding with the hydrothermal fluids during their ascent to the seafloor. Presence of gaseous (circles), liquid (diamond) or supercritical phase (star) is dependent on the velocity and magnitude of cooling illustrated by a temperature profile from hot (red) to cold (blue).

Above temperatures of 30.98°C and pressures of 7.375 MPa, carbon dioxide is in a supercritical state. Zhang *et al.* [2020] report the detection of supercritical CO₂ (CO₂(sc)) bubbles in the YK research area (process 2) by means of in situ Raman spectroscopy. A great number of Raman peaks indicate the presence of methane, hydrogen sulfide, and large amounts of nitrogen within these bubbles, likely due to the strong solvent properties of the CO₂(sc). Further, partly unknown compounds are assumed to reach the supercritical bubbles by leaching out of organic material from the sediment or as reaction products within the bubbles. It is not known whether a fractionation process due to phase separation and segregation between the CO₂(sc) and a CO₂-depleted gaseous phase occurs. Zhang *et al.* [2020] pointed out the close proximity of the supercritical bubble emission site to the hydrothermal vents with

liquid CO₂ emission. However, it is more likely that both condensed phases result from different seafloor modification processes. Similar to liquid CO₂ [Francis, 1954], CO_{2 (sc)} is known as a good solvent for light hydrocarbons [Shi *et al.*, 2015]. However, neither Konno *et al.* [2006] nor Zhang *et al.* [2020] measured highly enhanced methane concentration in the CO₂ droplets and supercritical CO₂ bubbles, respectively. This could occur from a relatively low methane concentration of the initial condensed phase before phase separation at their investigated sites or a limited time of contact between both phases due to fast dissipation, hence the achievement of an equilibration and the dissolution of hypothesized large amounts of methane was hindered.

The emission of droplets is a result either of fast cooling of the rising condensed phases to temperature below the bubble point (process 3) or of ‘melting’ seafloor GH (process 4). Fractionation processes are not expected in the process 3, hence the gas composition does not change during this phase shift and the liquid phase is assumed to reflect the initial composition of the hydrothermal fluids. On the contrary the formation of GH in process 4 leads to fractionation between GH stabilizing compounds like carbon dioxide, methane, and hydrogen sulfide that enrich in the GH phase on the one hand, and the residual gas components remaining in the fluids and get emitted at another vent in close proximity. These condensed phases are characterized by an elevated concentration of light gases like hydrogen and helium that are too small to incorporate into the GH lattice. The occurrence of a previous phase separation process has a significant impact on the gas composition of both GH and residual gas composition. Konno *et al.* [2006] suggested that the high carbon dioxide concentration in the CO₂ droplets at YK arise from thermally driven decomposition of seafloor CO₂ hydrates, which were formed by cooling of fluid vapor that has been produced by phase separation. The formation of GH from a non-purified gas mixture leads to much more complex changes in mole fraction due to different property of GH stability and tendency of incorporation as shown in Table 5 and Fig. 31.

An exact assignment of the condensed phases to the described processes is difficult due to the complexity of possible phase and composition changes and is possible only to a limited extent without knowledge of the gas composition of the initial fluid uninfluenced by the modification processes. It is very likely that a combination of various secondary modification processes affect the fluids during their rise to the sediment surface. The most possible processes with the probably greatest influence on the composition of the individual collected condensed phases are considered hereinafter.

Condensed phase of dive 200, GS 3 is thought to undergo process 1 due to the elevated vent temperature of 50°C which is above the dew point of the gas mixtures (Fig. 36). The vent perhaps reflects the gas composition, which is close to the initial composition of the hydrothermal fluids, because no fractionation processes are expected at this temperature. With only a low probability this condensed phase could have been collected at the residual vent of process 2 after accumulation of the supercritical CO₂ phase, based on the relatively low CO₂/CH₄ ratio of the sample. However, the relatively high concentration of nitrogen in the sample contradict this process. *Zhang et al.* [2020] measured large amounts of nitrogen in the supercritical bubbles, hence the remaining phase would have been depleted in N₂. In general, it is not clear if this fractionation process due to phase separation occurs.

It is rather likely that the condensed phase of dive 202, GS 2 has its origin in the process 2. Temperature measurement of the Hi-Temp lance indicate a low vent temperature of 5°C directly at the emission site in close proximity to another vent emitting fluids with temperatures of up to 66°C (Fig. 20). Hence, the overall seafloor of this emission area seems to be warm and the condensed phase cools immediately before the release. In general, the formation of a supercritical CO₂ phase is possible at these conditions. Based on the low CO₂/CH₄ ratio, which is even smaller than in dive 200, GS 3, the collected condensed phase might be the separated residual CO₂-depleted gas phase. Solely the elevated nitrogen concentration in this sample is not consistent with this theory.

The gas composition of the condensed phases of dive 202, GS 3 and 4 exhibit the highest similarity to the CO₂ droplets at YK reported by *Konno et al.* [2006]. Hence, the process 4 might be a potential pathway of formation. However, it should be noted that the formation of GH of such complex gas mixtures is associated with a significant fractionation, as shown in Table 5 and Fig. 31. The CO₂/CH₄ ratio in the GH is apparently lower in comparison to the initial gas mixture. Especially for samples with such a high CO₂/CH₄ ratio like GS 3, it is not possible to determine an initial gas mixture, which would allow the formation of those GH. Furthermore, in the first fraction of GS 3 an extended H₂ concentration of 2.3 % was measured (Table 4). It has to be mentioned that it is not clear, whether the hydrogen is of hydrothermal origin, meaning a real component of the fluids. Replicate measurements confirm the high values in the subsample (23,370 and 23,252 ppm), but it can't be ruled out that the subsampler was contaminated or hydrogen got enriched in the subsampler via unknown pathways like catalytic degradation processes in the vessel during storage. In case of GH melting as the origin of the liquid phase, the sample should be hydrogen-free, because of non-stability of hydrogen in GH cages.

It is more likely, that the condensed phases of dive 202, GS 3 and 4 are formed by process 3. The hot hydrothermal fluids are allowed to cool down very fast to temperatures below the bubble point, hence transforms into a liquid phase without changes in the gas composition. A potential form of this phase transition is a spontaneous gas bubble collapse due to condensation. This process has been observed in close proximity to the vent of GS 3, as a gaseous phase got in contact with cold ambient deep sea water. This process can also occur in contact with cold pore water just below the seafloor surface. An incomplete gas-liquid phase shift due to fragmentary quenching can also explain the equivocal conclusions on the phase condition in situ of the condensed phase of GS 4 (Chapter 7.2.4).

8. Summary

The following chapter includes content of the article “Geochemical observations within the water column at the CO₂-rich hydrothermal systems Hatoma Knoll and Yonaguni Knoll IV, in the southern Okinawa Trough”. The quoted section is marked and the contribution footnoted.

The behavior of gas bubbles and droplets regarding dissolution and distribution in aquatic systems has been of interest to scientists for many decades (e.g. *Brewer et al.* [2002]; *Liebermann* [1957]; *Maini and Bishnoi* [1981]; *Rehder et al.* [2009]). The presented study contributes to our understanding of carbon dioxide and methane dominated condensed phases at two natural gas release areas (YK and HK) in the OT, western Pacific Ocean. They act as natural sites to investigate a leakage scenario of deep-water CCS. During cruise SO 196-2 the influence of the emitted gas-rich hydrothermal fluids and their distribution patterns have been investigated with in situ measurements as well as collection of discrete samples. Furthermore, the gas and isotopic composition of condensed phases were measured. In combination with thermodynamic calculations possible formation and fractionation processes of these condensed phases have been determined.

“Gas emission at both sites is dominated by carbon dioxide. The very high $\Delta C_T/{}^3\text{He}$ ratios in the water column of HK exceed almost all measured values reported for hydrothermal systems worldwide. So far, a higher CO₂/³He ratio has been measured only at volcano Ruby in the Mariana Arc [*Resing et al.*, 2009]. The composition of the fluids differs distinctly between the two investigated areas. Fluids from the YK are characterized by a $\Delta C_T/{}^3\text{He}$ signature which is about a factor of 1.7 lower than that from HK. A more moderate slope of the linear trend line in the $\Delta C_T/{}^3\text{He}$ -plot (Fig. 14) was observed at station 57, in the northeastern part of the YK. Predominant water current conditions during the investigation of this station support the hypothesis of the existence of a yet undiscovered vent at this seamount.

Linearity in the $\Delta C_T/{}^3\text{He}$ of the HK and YK samples indicates that only one fluid source dominates the flux of CO₂ fluids into the water column at each of the sites.

Based on temperature data, the main [CO₂] input in both hydrothermal systems originates from hot vent fluids (Fig. 15). This interpretation is further supported by the very high CO₂/³He ratios of the measured bubbles and droplets at the cold gas vents at HK, exceeding the values in the main plume at HK by a factor of 4 - 9.

The pH decreases within the water column at both research areas, HK and YK, and at station 57, seems to be caused mainly by CO₂ addition, as inferred from the $\Delta C_T/\Delta \text{pH}$ trend line (Fig. 16b). The slopes of these lines exclude a significant influence of other acids on pH, in contrast to results from *Fouquet et al.* [1991], *Gamo et al.* [1997], and *Resing et al.* [2004] at other BABs. Measured and calculated C_T and pH anomalies are close to the range of values reported from the NW Eifuku (Mariana Arc) [*Resing et al.*, 2009].

The trend lines also indicate that the fluids which influence the investigated water column have not been exposed to significant CaCO₃ dissolution processes during their rise through the sediment. However, it cannot be excluded that diffuse flow of liquid or supercritical CO₂ leads to pronounced CaCO₃ dissolution in the sediment and that these processes affect the geochemistry of the near-bottom layer of both systems [...]. Very high A_T values measured in pore waters of the upper sediment close to active sites in YK [*de Beer et al.*, 2013; *Neumann*, 2012] support this assumption, however, further investigations are required.”⁵⁵

The hot hydrothermal fluids influence the investigated water column at HK and YK up to 260 m height regarding helium and C_T signature, Eh and pH. The CO₂ flux of the upper water column is dominated by the hot hydrothermal fluids, while the condensed phases are assumed to mainly affect the lowermost 10 m of the water column, because this part of the water column has not been investigated geochemically. Nonetheless, the condensed phases rise to shallower water depths. Especially the formation of a GH skin in case of the emission into the GHSZ enables higher rising heights due to thermal stability and reduced dissolution. The faster dissolution of CO₂ out of the GH lattice leads to an enrichment of methane during the

⁵⁵ My contribution of the cited part included all writing, which was proof-read by the co-authors.

ascent. This change in gas composition will cause a phase transformation within the droplet from liquid to gaseous. The resulting decrease of the density will increase the buoyancy and rising height. The rising height is also influenced by the dissolution processes between the condensed phase and seawater which is reduced by the GH skin, but not hindered completely (e.g. *Rehder et al.* [2004]). The rise of a condensed phase emitted at the vent from dive 202, GS 3 was monitored for 144 m until the bubble box lost it. Nonetheless, the significantly lower flux of the condensed phase (about $10^2 \text{ mol} \cdot \text{year}^{-1} \cdot \text{vent}^{-1}$) hardly affects the CO_2 budget of the upper water body in comparison to the dominant CO_2 input of the hot fluids ($10^8 \text{ mol} \cdot \text{year}^{-1} \cdot \text{vent}^{-1}$).

Phase transformation and fractionation processes below the seafloor, at the time of emission, and during the ascent through the water column are complex. The sources and processes with highest possibility are outlined schematically within the presented study. The available data and scientific knowledge impedes clear identification of the origin of each compound, and declaration which processes are able to cause the great differences in gas composition between the vents despite spatial proximity. A complex combination of phase shift, phase separation and segregation and fractionation processes potentially affect the condensed phases during their rise to the seafloor. Video material, measured gas composition, and the results of the phase calculation indicate on the collection of two gaseous (dive 200, GS 3, dive 202, GS 2) and one liquid condensed phase (dive 202, GS 3). The results of dive 202, GS 4 are equivocal. It is probable that a 2-phase system has been collected.

The homogenous isotope data of the samples indicate a common origin of the condensed phases. It can be assumed that the dive 200, GS 3 reflects the gas composition, which is close to the initial composition of the hydrothermal fluids, because the number of possible modification processes able to change the gas composition is limited at this elevated temperature. *Zhang et al.* [2020] found evidence for the emission of supercritical CO_2 bubbles at YK. However, this is the first discovery of a natural $\text{CO}_2(\text{sc})$ vent, hence the knowledge of its formation and possible fractionation processes is limited.

The emitted liquid CO₂-dominated droplets (dive 202, GS 3) are very likely not formed in a way described by *Sakai et al.* [1990a] and *Konno et al.* [2006], because the gas composition of the condensed phase is not compatible to the expected fractionation processes (Table 5, Fig. 31). Furthermore, the absence of appreciable sediment coverage at the emission sites at HK prevents the reported process of the formation of a subsedimentary CO₂-rich vapor phase with a GH caprock. An accumulation of this phase is of course possible under a rocky fault, but cannot get emitted into the water column by rupture. The geological formation rather promotes the direct injection of the condensed phase into the water column, hence with an apparently shorter residence time in the cold subseafloor before escaping into the water column.

References

- Adams, E. E., and K. Caldeira (2008). Ocean storage of CO₂, *Elements*, 4(5), 319-324.
- Bach, W. (2011), Reports and preliminary results of RV Sonne Cruise SO 216, BAMBUS, *Berichte, Fachbereich Geowissenschaften*, University of Bremen, 280, pp. 87.
- Baker, E. T., G. J. Massoth, K.-i. Nakamura, R. W. Embley, C. E. J. de Ronde, and R. J. Arculus (2005), Hydrothermal activity on near-arc sections of back-arc ridges: Results from the Mariana Trough and Lau Basin, *Geochem. Geophys. Geosyst.*, 6(9), Q09001.
- Baker, E. T., J. A. Resing, S. L. Walker, F. Martinez, B. Taylor, and K.-i. Nakamura (2006), Abundant hydrothermal venting along melt-rich and melt-free ridge segments in the Lau back-arc basin, *Geophys. Res. Lett.*, 33(7), L07308.
- Baross, J., and S. Hoffman (1985), Submarine hydrothermal vents and associated gradient environments as sites for the origin and evolution of life, *Orig. Life Evol. Biosph.*, 15(4), 327-345.
- Barry, P. H., D. R. Hilton, T. P. Fischer, J. M. De Moor, F. Mangasini, and C. Ramirez (2012), Helium and carbon isotope systematics of cold “mazuku” CO₂ vents and hydrothermal gases and fluids from Rungwe Volcanic Province, southern Tanzania. *Chem. Geol.*, 339, 141-156.
- Bernard, B. B. (1978), Light hydrocarbons in marine sediments, *Medium: X*; 154 pp.
- Bigalke, N. K., L. I. Enstad, G. Rehder, and G. Alendal (2010), Terminal velocities of pure and hydrate coated CO₂ droplets and CH₄ bubbles rising in a simulated oceanic environment, *Deep Sea Res. Part I: Oceanogr. Res. Pap.*, 57(9), 1102-1110.
- Brewer, P. G., E. T. Peltzer, G. Friederich, and G. Rehder (2002), Experimental determination of the fate of rising CO₂ droplets in seawater, *Environ. Sci. Technol.*, 36(24), 5441-5446.
- Bushuyev, O. S., P. De Luna, C. T. Dinh, L. Tao, G. Saur, G., J. van de Lagemaat, S. O. Kelley, and E. H. Sargent (2018), What should we make with CO₂ and how can we make it?. *Joule*, 2(5), 825-832.
- Buß, A. (2011), Plume dispersal at hydrothermal vent fields with natural CO₂ seeps in the North-West Pacific, *Master Thesis, University of Bremen, Bremen, Germany*.
- Butterfield, D. A., G. J. Massoth, R. E. McDuff, J. E. Lupton, and M. D. Lilley (1990), Geochemistry of Hydrothermal Fluids From Axial Seamount Hydrothermal Emissions Study Vent Field, Juan de Fuca Ridge: Subseafloor Boiling and Subsequent Fluid-Rock Interaction, *J. Geophys. Res.*, 95(B8), 12895-12921.
- Caramanna, G., Voltattorni, N., and Maroto-Valer, M. M. (2011), Is Panarea Island (Italy) a valid and cost-effective natural laboratory for the development of detection and monitoring techniques for submarine CO₂ seepage?, *Greenh. Gases*, 1(3), 200-210.
- Chen, C.-T. A., and S.-L. Wang (1998), Influence of intermediate water in the western Okinawa Trough by the outflow from the South China Sea, *J. Geophys. Res.: Oceans*, 103(C6), 12683-12688.
- Circone, S., L. A. Stern, S. H. Kirby, W. B. Durham, B. C. Chakoumakos, C. J. Rawn, A. J. Rondinone, and Y. Ishii (2003), CO₂ hydrate: synthesis, composition, structure, dissociation behavior, and a comparison to structure I CH₄ hydrate, *J. Phys. Chem. B*, 107(23), 5529-5539.

- Gena, K., K. Kase, H. Chiba, and K. Nakashima (2005), Tin-bearing chalcopyrite and platinum-bearing bismuthinite in the active Tiger sulfide chimney, Yonaguni Knoll IV seafloor hydrothermal system, Okinawa Trough, Japan, *Eos Trans. AGU*, AGU Fall Meeting abstract #V51C-1492.
- German, C. R., E. T. Baker, D. P. Connelly, J. E. Lupton, J. Resing, R. D. Prien, S. L. Walker, H. N. Edmonds, and C. H. Langmuir (2006), Hydrothermal exploration of the Fonualei Rift and Spreading Center and the Northeast Lau Spreading Center, *Geochem. Geophys. Geosyst.*, 7(11), Q11022.
- Glasby, G. P., G. A. Cherkashov, G. M. Gavrilenko, V. A. Rashidov, and I. B. Slovtsov (2006), Submarine hydrothermal activity and mineralization on the Kurile and western Aleutian island arcs, N.W. Pacific, *Mar. Geol.*, 231(1-4), 163-180.
- Gugliandolo, C., F. Italiano, and T. L. Maugeri (2006), The submarine hydrothermal system of Panarea (Southern Italy): biogeochemical processes at the thermal fluids-sea bottom interface, *Ann. Geophys.*, 49(2/3), 783-792.
- Häckel, M. (2011), Sequestrierung von CO₂ in marinen Sedimenten: Geochemische Einsichten in das natürliche Labor Yonaguni Knoll im südlichen Okinawa Trog, in *Statusseminar Meeresforschung mit FS Sonne 2011*, Forschungszentrum Jülich, Energie, Ökologie, Bereich Meeres- und Polarforschung, pp. 103-106, Hannover.
- Halbach, P., K.-i. Nakamura, M. Wahsner, J. Lange, H. Sakai, L. Käselitz, R.-D. Hansen, M. Yamano, J. Post, B. Prause, R. Seifert, W. Michaelis, F. Teichmann, M. Kinoshita, A. Märten, J. Ishibashi, S. Czerwinski, and N. Blum (1989), Probable modern analogue of Kuroko-type massive sulphide deposits in the Okinawa Trough back-arc basin, *Nature*, 338, 496-499.
- Hawkins, J. W., S. H. Bloomer, C. A. Evans, and J. T. Melchior (1984), Evolution of intra-oceanic arc-trench systems, *Tectonophysics*, 102(1-4), 175-205.
- Herzig, P. M., M. D. Hannington, and A. Arribas Jr (1998), Sulfur isotopic composition of hydrothermal precipitates from the Lau back-arc: implications for magmatic contributions to seafloor hydrothermal systems, *Mineral. Deposita*, 33(3), 226-237.
- Herzog, H., D. Golomb, and S. Zemba (1991), Feasibility, modeling and economics of sequestering power plant CO₂ emissions in the deep ocean, *Environ. Prog.*, 10(1), 64-74.
- Herzog, H. and D. Golomb (2004), Carbon Capture and Storage from Fossil Fuel Use, *Enc.energ.*, 1(6562), 277-287.
- Hilton, D. R., T. P. Fischer, and B. Marty (2002), Noble Gases and Volatile Recycling at Subduction Zones, *Rev. Mineral. Geochem.*, 47(1), 319-370
- Hoefs, J. (1980), *Stable Isotope Geochemistry*, 2nd edition, 208 pp., Springer Verlag, Berlin, Heidelberg, New York.
- Holder, G. D., A. V. Cugini, and R. P. Warzinski (1995), Modeling clathrate hydrate formation during carbon dioxide injection into the ocean, *Environ. Sci. Technol.*, 29(1), 276-278.
- Holland, G., and S. Gilfillan (2013), Application of Noble Gases to the Viability of CO₂ Storage, in *The Noble Gases as Geochemical Tracers*, edited by P. Burnard, pp. 177-223, Springer Berlin Heidelberg.
- Honda, M., J. Hashimoto, J. Naka, and H. Hotta (1995), CO₂ hydrate formation and inversion of density between liquid CO₂ and H₂O in deep sea: Experimental study using submersible 'Shinkai 6500', *Direct ocean disposal of carbon dioxide. TERRAPUB*, 35-43.
- Horibe, Y., K. R. Kim, and H. Craig (1986), Hydrothermal methane plumes in the Mariana back-arc spreading centre, *Nature*, 324(6093), 131-133.

- House, K. Z., D. P. Schrag, C. F. Harvey, and K. S. Lackner (2006), Permanent carbon dioxide storage in deep-sea sediments, *Proc. Nat. Acad. Sci.*, 103(33), 12291-12295.
- Hunt, J. M. (1966), The significance of carbon isotope variations in marine sediments, in *Advances in Organic Geochemistry. Proceedings of the Third International Congress*, (Vol. 32), 27-35, London.
- IEA Greenhouse Gas R&D Programme (2008), Assessment of Sub Sea Ecosystem Impacts *Rep. 2008/8*, Orchard Business Centre, Stoke Orchard, Cheltenham, UK
- Inagaki, F., M. M. M. Kuypers, U. Tsunogai, J.-i. Ishibashi, K.-i. Nakamura, T. Treude, S. Ohkubo, M. Nakaseama, K. Gena, H. Chiba, H. Hirayama, T. Nunoura, K. Takai, B. B. Jorgensen, K. Horikoshi, and A. Boetius (2006), Microbial community in a sediment-hosted CO₂ lake of the southern Okinawa Trough hydrothermal system, *Proc. Natl. Acad. Sci.*, 103(38), 14164-14169.
- Infochem (2014), User Guide for Multiflash for Windows (Version 4.4), Infochem Computer Services.
- Ishibashi, J.-i. (1991), Geochemical studies of hydrothermal fluids in the middle Okinawa Trough back arc basin, *PhD thesis*, University of Tokyo, Tokyo, Japan.
- Ishibashi, J.-i., J. E. Lupton, T. Yamaguchi, J. Querellou, T. Nunoura, and K. Takai (2006), Expedition reveals changes in Lau Basin Hydrothermal System, *Eos Trans. AGU*, 87(2), 13-17.
- Ishibashi, J. I., K. Okino, and M. Sunamura (2015). *Subseafloor Biosphere Linked to Hydrothermal Systems*, Springer Japan: Imprint, Springer.
- Ishibashi, J.-i., Y. Sano, H. Wakita, T. Gamo, M. Tsutsumi, and H. Sakai (1995), Helium and carbon geochemistry of hydrothermal fluids from the Mid-Okinawa Trough Back Arc Basin, southwest of Japan, *Chem. Geol.*, 123(1-4), 1-15.
- Ishibashi, J.-I., and T. Urabe (1995), Hydrothermal activity related to arc-backarc magmatism in the Western Pacific, in *Backarc Basins: Tectonics and Magmatism*, edited by B. Taylor, pp. 451-195, Plenum Press, New York.
- Javoy, M., F. Pineau, and H. Delorme (1986), Carbon and nitrogen isotopes in the mantle, *Chem. Geol.*, 57(1-2), 41-62.
- Johnson, K. M., A. E. King, and J. M. Sieburth (1985), Coulometric TCO₂ analyses for marine studies; an introduction, *Mar. Chem.*, 16(1), 61-82.
- Johnson, K. M., J. M. Sieburth, P. J. I. Williams, and L. Brändström (1987), Coulometric total carbon dioxide analysis for marine studies: Automation and calibration, *Mar. Chem.*, 21(2), 117-133.
- Kawagucci, S. (2015), Fluid Geochemistry of High-Temperature Hydrothermal Fields in the Okinawa Trough, in *Subseafloor Biosphere Linked to Hydrothermal Systems: TAIGA Concept*, edited by J. Ishibashi, K. Okino and M. Sunamura, Springer, Tokyo.
- Kawagucci, S., H. Chiba, J.-i. Ishibashi, T. Yamanaka, T. Toki, Y. Muramatsu, Y. Ueno, A. Makabe, K. Inoue, N. Yoshida, S. Nakagawa, T. Nunoura, K. Takai, N. Takahata, Y. Sano, T. Narita, G. Teranishi, H. Obata, T. Gamo (2011), Hydrothermal fluid geochemistry at the Iheya North field in the mid-Okinawa Trough: Implication for origin of methane in subseafloor fluid circulation systems, *Geochem J.*, 45(2), 109-124.
- Kawagucci, S., Y. Matsui, and G. L. Früh-Green (2020), Radiocarbon content of carbon dioxide and methane in hydrothermal fluids of Okinawa Trough vents., *Geochem. J.*, 54(3), 129-138.
- Kawagucci, S., K. Shirai, T. F. Lan, N. Takahata, U. Tsunogai, Y. Sano, and T. Gamo (2010), Gas geochemical characteristics of hydrothermal plumes at the HAKUREI

- and JADE vent sites, the Izena Cauldron, Okinawa Trough, *Geochem J.*, 44, 507-518.
- Kawagucci, S., Y. Ueno, K. Takai, T. Toki, M. Ito, K. Inoue, A. Makabe, N. Yoshida, Y. Muramatsu, N. Takahata, Y. Sano, T. Narita, G. Teranishi, H. Obata, S. Nakagawa, T. Nunoura, T. Gamo (2013), Geochemical origin of hydrothermal fluid methane in sediment-associated fields and its relevance to the geographical distribution of whole hydrothermal circulation, *Chem. Geol.*, 339(0), 213-225.
- Kimura, M. (1985), Back-arc rifting in the Okinawa Trough, *Mar. Petrol. Geol.*, 2(3), 222-240.
- Konno, U., U. Tsunogai, F. Nakagawa, M. Nakaseama, J.-i. Ishibashi, T. Nunoura, and K.-i. Nakamura (2006), Liquid CO₂ venting on the seafloor: Yonaguni Knoll IV hydrothermal system, Okinawa Trough, *Geophys. Res. Lett.*, 33(16), L16607.
- Lavelle, J. W., D. Di Iorio, and P. Rona (2013), A turbulent convection model with an observational context for a deep-sea hydrothermal plume in a time-variable cross flow, *J. Geophys. Res. Oceans* 118, 1–16.
- Lee, C.-S., G. G. Shor Jr, L. D. Bibee, R. S. Lu, and T. W. C. Hilde (1980), Okinawa Trough: Origin of a back-arc basin, *Mar. Geol.*, 35(1-3), 219-241.
- Letouzey, J., and M. Kimura (1985), Okinawa Trough genesis: structure and evolution of a backarc basin developed in a continent, *Mar. Petrol. Geol.*, 2(2), 111-130.
- Letouzey, J., and M. Kimura (1986), The Okinawa Trough: Genesis of a back-arc basin developing along a continental margin, *Tectonophysics*, 125(1-3), 209-230.
- Liebermann, L. (1957), Air Bubbles in Water, *J. Appl. Phys.*, 28(2), 205-211.
- Lu, R. S., J. J. Pan, and T. C. Lee (1981), Heat flow in the southwestern Okinawa Trough, *Earth Planet. Sci. Lett.*, 55(2), 299-310.
- Lupton, J. E. (1983), Terrestrial Inert Gases: Isotope Tracer Studies and Clues to Primordial Components in the Mantle, *Annu. Rev. Earth Planet. Sci.*, 11(1), 371-414.
- Lupton, J. E., R. J. Arculus, R. R. Greene, L. J. Evans, and C. I. Goddard (2009), Helium isotope variations in seafloor basalts from the Northwest Lau Backarc Basin: Mapping the influence of the Samoan hotspot, *Geophys. Res. Lett.*, 36(17), L17313.
- Lupton, J. E., D. Butterfield, M. Lilley, L. Evans, K.-i. Nakamura, W. Chadwick Jr., J. Resing, R. Embley, E. Olson, G. Proskurowski, E. Baker, C. de Ronde, K. Roe, R. Greene, G. Lebon, and C. Young (2006), Submarine venting of liquid carbon dioxide on a Mariana Arc volcano, *Geochem. Geophys. Geosyst.*, 7(8), Q08007.
- Lupton, J. E., and H. Craig (1975), Excess ³He in oceanic basalts: Evidence for terrestrial primordial helium, *Earth Planet. Sc. Lett.*, 26(2), 133-139.
- Lupton, J. E., G. P. Klinkhammer, W. R. Normark, R. Haymon, K. C. MacDonald, R. F. Weiss, and H. Craig (1980), Helium-3 and manganese at the 21°N East Pacific Rise hydrothermal site, *Earth Planet. Sci. Lett.*, 50(1), 115-127.
- Lupton, J. E., M. Lilley, D. Butterfield, L. Evans, R. Embley, G. Massoth, B. Christenson, K.-i. Nakamura, and M. Schmidt (2008), Venting of a separate CO₂-rich gas phase from submarine arc volcanoes: Examples from the Mariana and Tonga-Kermadec arcs, *J. Geophys. Res.*, 113(B8), B08S12.
- Lupton, J. E., K. H. Rubin, R. Arculus, M. Lilley, D. Butterfield, J. Resing, E. Baker, and R. Embley (2015), Helium isotope, C/³He, and Ba-Nb-Ti signatures in the northern Lau Basin: Distinguishing arc, back-arc, and hotspot affinities. *Geochem. Geophys. Geosyst.*, 16(4), 1133-1155.
- Maini, B. B., and P. R. Bishnoi (1981), Experimental investigation of hydrate formation behaviour of a natural gas bubble in a simulated deep sea environment, *Chem. Eng. Sci.*, 36(1), 183-189.

- Martinez, F., K. Okino, Y. Ohara, A.-L. Reysenbach, and S. K. Goffredi (2007), Back-arc basins, *Oceanography*, 20(1), 116-127.
- Marty B., A. Jambon, and Y. Sano (1989), Helium isotopes and CO₂ in volcanic gases of Japan, *Chem. Geol.*, 76(1-2), 25-40.
- Marty, B., and I. N. Tolstikhin (1998), CO₂ fluxes from mid-ocean ridges, arcs and plumes, *Chem. Geol.*, 145(3-4), 233-248.
- Massoth, G. J., D. A. Butterfield, J. E. Lupton, R. E. McDuff, M. D. Lilley, and I. R. Jonasson (1989), Submarine venting of phase-separated hydrothermal fluids at Axial Volcano, Juan de Fuca Ridge, *Nature*, 340(6236), 702-705.
- Matsumoto, T., M. Kinoshita, M. Nakamura, J.-C. Sibuet, C.-S. Lee, S.-K. Hsu, Y. Hashimoto, K. Tatekawa, and M. Kimura (2001), Volcanic and hydrothermal activities and possible "segmentation" of the axial rifting in the westernmost part of the Okinawa Trough. Preliminary results from the YOKOSUKA/SHINKAI 6500 Lequios Cruise, *JAMSTEC J. Deep Sea Res.*, 19, 95-107.
- McGinnis, D. F., J. Greinert, Y. Artemov, S. E. Beaubien, and A. Wüest (2006), Fate of rising methane bubbles in stratified waters: How much methane reaches the atmosphere?, *J. Geophys. Res.: Oceans*, 111(C9), C09007.
- Merlivat, L., F. Pineau, and M. Javoy (1987), Hydrothermal vent waters at 13°N on the East Pacific Rise: isotopic composition and gas concentration, *Earth Planet. Sci. Lett.*, 84(1), 100-108.
- Millero, F. J., T. B. Graham, F. Huang, H. Bustos-Serrano, and D. Pierrot (2006), Dissociation constants of carbonic acid in seawater as a function of salinity and temperature, *Mar. Chem.*, 100(1-2), 80-94.
- Miyazaki, J., S. Kawagucci, A. Makabe, A. Takahashi, K. Kitada, J. Torimoto, Y. Matsui, E. Tasumi, T. Shibuya, K. Nakamura, S. Horai, S. Sato, J.-i. Ishibashi, H. Kanzaki, S. Nakagawa, M. Hirai, Y. Takaki, K. Okino, H. K. Watanabe, H. Kumagai, and C. Chen (2017), Deepest and hottest hydrothermal activity in the Okinawa Trough: the Yokosuka site at Yaeyama Knoll, *R. Soc. Open Sci.*, 4(12), 171570.
- Monecke, T., S. Petersen, and M. D. Hannington (2014), Constraints on water depth of massive sulfide formation: Evidence from modern seafloor hydrothermal systems in arc-related settings. *Econ. Geol.*, 109(8), 2079-2101.
- Mukumoto, K., T. Tsuji, and A. Hendriyana (2019), Large gas reservoir along the rift axis of a continental back-arc basin revealed by automated seismic velocity analysis in the Okinawa Trough, *Geophys. Res. Lett.*, 46(16), 9583-9590.
- Nakamura, H., A. Nishina, H. Ichikawa, M. Nonaka, and H. Sasaki (2008), Deep countercurrent beneath the Kuroshio in the Okinawa Trough, *J. Geophys. Res.*, 113(C6), C06030.
- Nakamura, K.-i., S. Veirs, C. P. Sarason, R. E. McDuff, F. Stahr, D. R. Yoerger, and A. M. Bradley (2000), Electrochemical signals in the rising buoyant plumes and tidally oscillation plumes at the main Endeavour vent field, Juan de Fuca Ridge, *Eos Trans. AGU*, AGU Fall Meeting abstract #OS52I-05.
- Nealson, K. (2006), Lakes of liquid CO₂ in the deep sea, *Proc. Nat. Acad. Sci.*, 103(38), 13903-13904.
- Neumann, J. (2012), Effect of high CO₂ and low pH on benthic communities of the deep sea, *PhD thesis*, University of Bremen, Bremen, Germany.
- Nunoura, T., and K. Takai (2009), Comparison of microbial communities associated with phase-separation-induced hydrothermal fluids at the Yonaguni Knoll IV hydrothermal field, the Southern Okinawa Trough, *FEMS Microbiol. Ecol.*, 67(3), 351-370.

- Nunoura, T., H. Oida, M. Nakaseama, A. Kosaka, S. B. Ohkubo, T. Kikuchi, H. Kazama, S. Hosoi-Tanabe, K.-i. Nakamura, M. Kinoshita, H. Hirayama, F. Inagaki, U. Tsunogai, J.-i. Ishibashi, and K. Takai (2009), Archaeal Diversity and Distribution along Thermal and Geochemical Gradients in Hydrothermal Sediments at the Yonaguni Knoll IV Hydrothermal Field in the Southern Okinawa Trough, *Appl. Environ. Microbiol.*, 76(4), 1198-1211.
- Pape, T., A. Bahr, J. Rethemeyer, J. D. Kessler, H. Sahling, K.-U. Hinrichs, S. A. Klapp, W. S. Reeburgh, and G. Bohrmann (2010), Molecular and isotopic partitioning of low-molecular-weight hydrocarbons during migration and gas hydrate precipitation in deposits of a high-flux seepage site, *Chem. Geol.*, 269(3-4), 350-363.
- Pedersen, R. B., and T. Baumberger (2011), Cruise Report Jan Mayen vent fields (JMVf) ; R/V G.O. Sars, Expedition No. 2011108/CGB2011, 10. – 22. June 2011, Bergen – Bergen, Norway *Rep.*, Centre for Geobiology, UiB, Bergen, Norway.
- Pelletier, G., E. Lewis, and D. Wallace (2007), CO2sys.xls: a calculator for the CO₂ system in seawater for Microsoft Excel/VBA, Washington State Department of Ecology/Brookhaven National Laboratory, Olympia, WA/Upton, NY, USA.
- Rackley, S. A (2017), *Carbon Capture and Storage*, Butterworth-Heinemann, 2nd edition, pp. 698.
- Rehder, G., P. W. Brewer, E. T. Peltzer, and G. Friederich (2002), Enhanced lifetime of methane bubble streams within the deep ocean, *Geophys. Res. Lett.*, 29(15).
- Rehder, G., S. H. Kirby, W. B. Durham, L. A. Stern, E. T. Peltzer, J. Pinkston, and P. G. Brewer (2004), Dissolution rates of pure methane hydrate and carbon-dioxide hydrate in undersaturated seawater at 1000-m depth, *Geochim. Cosmochim. Ac.*, 68(2), 285-292.
- Rehder, G., I. Leifer, P. G. Brewer, G. Friederich, and E. T. Peltzer (2009), Controls on methane bubble dissolution inside and outside the hydrate stability field from open ocean field experiments and numerical modeling, *Mar. Chem.*, 114(1-2), 19-30.
- Rehder, G., and J. Schneider von Deimling (2008), RV Sonne Cruise Report SO 196 SUMSUN 2008 *Rep.*, Leibniz Institute for Baltic Sea Research Warnemünde, Warnemünde.
- Resing, J. A., E. T. Baker, J. E. Lupton, S. L. Walker, D. A. Butterfield, G. J. Massoth, and K.-i. Nakamura (2009), Chemistry of hydrothermal plumes above submarine volcanoes of the Mariana Arc, *Geochem. Geophys. Geosyst.*, 10(2), Q02009.
- Resing, J. A., J. E. Lupton, R. A. Feely, and M. D. Lilley (2004), CO₂ and ³He in hydrothermal plumes: implications for mid-ocean ridge CO₂ flux, *Earth Planet. Sci. Lett.*, 226(3-4), 449-464.
- Römer, M., H. Sahling, T. Pape, G. Bohrmann, and V. Spieß (2012), Quantification of gas bubble emissions from submarine hydrocarbon seeps at the Makran continental margin (offshore Pakistan), *J. Geophys. Res.: Oceans*, 117(C10).
- Saegusa, S., U. Tsunogai, F. Nakagawa, and S. Kaneko (2006), Development of a multibottle gas-tight fluid sampler WHATS II for Japanese submersibles/ROVs, *Geofluids*, 6(3), 234-240.
- Sahling, H., M. Römer, T. Pape, B. Bergès, C. dos Santos Fereirra, J. Boelmann, P. Geprägs, M. Tomczyk, N. Nowald, W. Dimmler, L. Schroedter, M. Glockzin, and G. Bohrmann (2014), Gas emissions at the continental margin west of Svalbard: mapping, sampling, and quantification, *Biogeosciences*, 11(21), 6029-6046.
- Sakai, H., T. Gamo, E. S. Kim, M. Tsutsumi, T. Tanaka, J. Ishibashi, H. Wakita, M. Yamano, and T. Oomori (1990a), Venting of Carbon Dioxide-Rich Fluid and

- Hydrate Formation in Mid-Okinawa Trough Backarc Basin, *Science*, 248(4959), 1093-1096.
- Sakai, H., T. Gamo, E. S. Kim, K. Shitashima, F. Yanagisawa, M. Tsutsumi, J. Ishibashi, Y. Sano, H. Wakita, T. Tanaka, T. Matsumoto, T. Naganuma, and K. Mitsuzawa (1990b), Unique chemistry of the hydrothermal solution in the mid-Okinawa Trough Backarc Basin, *Geophys. Res. Lett.*, 17(12), 2133-2136.
- Sano, Y., N. Takahata, Y. Nishio, T. P. Fischer, and S. N. Williams (2001), Volcanic flux of nitrogen from the Earth, *Chem. Geol.*, 171(3-4), 263-271.
- Saunders, A. D., and J. Tarney (1984), Geochemical characteristics of basaltic volcanism within back-arc basins, *J. Geol. Soc London, Special Publications*, 16(1), 59-76.
- Schmidt, M., Linke, P., Sommer, S., Esser, D., and Cherednichenko, S. (2015), Natural CO₂ seeps offshore Panarea: A test site for subsea CO₂ leak detection technology, *Mar. Tech. Soc. J.*, 49(1), 19-30.
- Sdrolias, M., and R. D. Müller (2006), Controls on back-arc basin formation, *Geochem. Geophys. Geosyst.*, 7(4), Q04016.
- Seewald, J. S., K. W. Doherty, T. R. Hammar, and S. P. Liberatore (2002), A new gas-tight isobaric sampler for hydrothermal fluids, *Deep Sea Res. Part I: Oceanogr. Res. Pap.*, 49(1), 189-196.
- Shi, Q., L. Jing, and W. Qiao (2015), Solubility of n-alkanes in supercritical CO₂ at diverse temperature and pressure, *J. CO₂ Util.*, 9, 29-38.
- Shitashima, K. (1997), CO₂ supply from deep-sea hydrothermal systems, *Waste Manage.*, 17(5-6), 385-390.
- Shitashima, K., and Y. Maeda (2005), Fate of liquid CO₂ discharged from the hydrothermal area in the Okinawa Trough, *Eos Trans. AGU*, 86(52), AGU Fall Meeting, abstract #B33A-1018.
- Shitashima, K., Y. Maeda, Y. Koike, and T. Ohsumi (2008), Natural analogue of the rise and dissolution of liquid CO₂ in the ocean, *Int. J. Greenh. Gas Control*, 2(1), 95-104.
- Sibuet, J.-C., J. Letouzey, F. Barbier, J. Charvet, J.-P. Foucher, T. W. C. Hilde, M. Kimura, C. Ling-Yun, B. Marsset, C. Muller, and J.-F. Stéphan (1987), Back Arc Extension in the Okinawa Trough, *J. Geophys. Res.*, 92(B13), 14041-14063.
- Sloan, E. D., and C. Koh (2008), *Clathrate hydrates of natural gases*, CRC Press, Boca Raton, Fla.
- Span, R. and W. Wagner (1996), A New Equation of State for Carbon Dioxide Covering the Fluid Region from the Triple-Point Temperature to 1100 K at Pressures up to 800 MPa, *J. Phys. Chem. Ref. Data*, 25, 1509.
- Speer, K. G., and P. A. Rona (1989), A model of an Atlantic and Pacific hydrothermal plume, *J. Geophys. Res.: Oceans*, 94(C5), 6213-6220.
- Staudigel, H., S. R. Hart, A. Pile, B. E. Bailey, E. T. Baker, S. Brooke, D. P. Connelly, L. Haucke, C. R. German, I. Hudson, D. Jones, A. A. P. Koppers, J. Konter, R. Lee, T. W. Pietsch, B. M. Tebo, A. S. Templeton, R. Zierenberg, and C. M. Young (2006), Vailulu'u Seamount, Samoa: life and death on an active submarine volcano, *Proc. Natl. Acad. Sci.*, 103(17), 6448-6453.
- Stranne, C., R. A. Sohn, B. Liljebladh, and K.-i. Nakamura (2010), Analysis and modeling of hydrothermal plume data acquired from the 85°E segment of the Gakkel Ridge, *J. Geophys. Res.: Oceans*, 115(C6), C06028.
- Sültenfuß, J., W. Roether, and M. Rhein (2009), The Bremen mass spectrometric facility for the measurement of helium isotopes, neon, and tritium in water, *Isot. Environ. Health Stud.*, 45(2), 83-95.

- Suzuki, R., J.-I. Ishibashi, M. Nakaseama, U. Konno, U. Tsunogai, K. Gena, and H. Chiba (2008), Diverse Range of Mineralization Induced by Phase Separation of Hydrothermal Fluid: Case Study of the Yonaguni Knoll IV Hydrothermal Field in the Okinawa Trough Back-Arc Basin, *Resour. Geol.*, 58(3), 267-288.
- Takai, K., T. Nunoura, J.-i. Ishibashi, J. Lupton, R. Suzuki, H. Hamasaki, Y. Ueno, S. Kawagucci, T. Gamo, Y. Suzuki, H. Hirayama, and K. Horikoshi (2008), Variability in the microbial communities and hydrothermal fluid chemistry at the newly discovered Mariner hydrothermal field, southern Lau Basin, *J. Geophys. Res.*, 113(G2), G02031.
- Talley, L. D. (2007), *Hydrographic Atlas of the World Ocean Circulation Experiment (WOCE). Volume 2: Pacific Ocean*, International WOCE Project Office, Southampton, U.K.
- Tao, Y., S. Rosswog, and M. Brüggem (2013), A simulation modeling approach to hydrothermal plumes and its comparison to analytical models, *Ocean Modell.* 61, 68–80.
- Toki, T., M. Itoh., D. Iwata, S. Ohshima, R. Shinjo, J.-i. Ishibashi, U. Tsunogai, N. Takahata, Y. Sano, T. Yamanaka, A. Ijiri, N. Okabe, T. Gamo, Y. Muramatsu, Y. Ueno, S. Kawagucci, K. Takai (2016), Geochemical characteristics of hydrothermal fluids at Hatoma Knoll in the southern Okinawa Trough, *Geochem. J.*, 50(6), 493-525.
- Tummescheit, H., and J. Eborn (2002), Chemical reaction modeling with ThermoFluid/MF and MultiFlash, in *Proceedings of the 2th Modelica Conference*, pp. 31-39.
- Tunnicliffe, V., K. T. A. Davies, D. A. Butterfield, R. W. Embley, J. M. Rose, and W. W. Chadwick Jr (2009), Survival of mussels in extremely acidic waters on a submarine volcano, *Nat. Geosci.*, 2(5), 344-348.
- Vielstädte, L., J. Karstens, M. Haeckel, M. Schmidt, P. Linke, S. Reimann, V. Liebetrau, D. F. McGinnis, K. Wallmann (2015), Quantification of methane emissions at abandoned gas wells in the Central North Sea, *Mar. Pet. Geol.*, 68(Part B), 848-860.
- Visbeck, M. (2002), Deep velocity profiling using lowered acoustic Doppler profilers: Bottom track and inverse solutions, *J. Atmos. Oceanic Technol.*, 19(5), 794–807.
- Von Damm, K. L. (2000), Chemistry of hydrothermal vent fluids from 9°–10°N, East Pacific Rise: “Time zero,” the immediate post-eruptive period, *J. Geophys. Res.: Solid Earth*, 105(B5), 11203-11222.
- Von Damm, K. L., and J. L. Bischoff (1987), Chemistry of hydrothermal solutions from the southern Juan de Fuca Ridge, *J. Geophys. Res.: Sol Ea*, 92(B11), 11334-11346.
- Von Damm, K. L., L. G. Buttermore, S. E. Oosting, A. M. Bray, D. J. Fornari, M. D. Lilley, and W. C. Shanks III (1997), Direct observation of the evolution of a seafloor "black smoker" from vapor to brine, *Earth Planet. Sc. Lett.*, 149(1-4), 101-111.
- Von Damm, K. L., J. M. Edmond, C. I. Measures, and B. Grant (1985), Chemistry of submarine hydrothermal solutions at Guaymas Basin, Gulf of California, *Geochim. Cosmochim. Ac.*, 49(11), 2221-2237.
- Walter, M., C. Mertens, U. Stöber, C. R. German, D. R. Yoerger, J. Sültenfuß, M. Rhein, B. Melchert, and E. T. Baker (2010), Rapid dispersal of a hydrothermal plume by turbulent mixing, *Deep-Sea Res. I*, 57(8), 931-945.
- Watanabe, K. (2001), Mapping the hydrothermal activity area on the Hatoma Knoll in the southern Okinawa Trough, *JAMSTEC J. Deep Sea Res.*, 19, 87-94.

- Watanabe, M., K. Hoshino, R. Shiokawa, Y. Takaoka, H. Fukumoto, Y. Shibata, R. Shinjo, and T. Oomori (2006), Metallic mineralization associated with pillow basalts in the Yaeyama Central Graben, Southern Okinawa Trough, Japan, *JAMSTEC Rep. Res. Developm.*, 3, 1-8.
- Well, R., J. Lupton, and W. Roether (2001), Crustal helium in deep Pacific waters, *J. Geophys. Res.: Oceans*, 106(C7), 14165-14177.
- Whiticar, M. J. (1999), Carbon and hydrogen isotope systematics of bacterial formation and oxidation of methane, *Chem. Geol.*, 161(1-3), 291-314.
- Winckler, G., W. Aeschbach-Hertig, J. Holocher, R. Kipfer, I. Levin, C. Poss, G. Rehder, P. Schlosser, E. Suess (2002), Noble gases and radiocarbon in natural gas hydrates, *Geophys. Res. Lett.*, 29(10), 63-1-63-4.
- Yamamoto, H., T. Maruyama, L. G.-Tóth, K. Kato, Y. Furushima, N. Taira, Y. Maeda, and K. Shitashima (2015), In Situ Determination of Bacterial Growth in Mixing Zone of Hydrothermal Vent Field on the Hatoma Knoll, Southern Okinawa Trough, in *Subseafloor Biosphere Linked to Hydrothermal Systems*, edited by J. Ishibashi, K. Okino and M. Sunamura, pp. 437-448, Springer, Tokyo.
- Yanagawa, K., Y. Morono, D. de Beer, M. Haeckel, M. Sunamura, T. Futagami, T. Hoshino, T. Terada, K.-i. Nakamura, T. Urabe, G. Rehder, A. Boetius, and F. Inagaki (2012), Metabolically active microbial communities in marine sediment under high-CO₂ and low-pH extremes, *ISME J.*
- Zhang, X., L.-F. Li, Z.-F. Du, X.-L. Hao, L. Cao, Z.-D. Luan, B. Wang, S.-C. Xi, C. Lian, J. Yan, and Wei-Dong Sun (2020), Discovery of supercritical carbon dioxide in a hydrothermal system, *Sci. Bull.*, 65(11), 958-964.

Appendix

Appendix I: “Derivation of the relationship between ${}^3\text{He}^{\text{excess}} / {}^4\text{He}^{\text{tot}}$ and $\delta^3\text{He}$, used in Chapter 4.3, is shown [here]. The measured ratio of ${}^3\text{He}$ and ${}^4\text{He}$ (R_{meas}) is a mixture of the atmospheric ratio (R_{atm}) and the ratio that is emitted by the vent (R_{vent}). The relative contribution of both ratios on R_{meas} is given by x_{atm} and x_{vent} , respectively, which sum is 1 by definition.”⁵⁶

$$R_{\text{meas}} = x_{\text{atm}} \cdot R_{\text{atm}} + x_{\text{vent}} \cdot R_{\text{vent}} \quad (\text{A1})$$

$$\frac{R_{\text{meas}}}{R_{\text{atm}}} = x_{\text{atm}} + x_{\text{vent}} \cdot \frac{R_{\text{vent}}}{R_{\text{atm}}} = (1 - x_{\text{vent}}) + x_{\text{vent}} \cdot \frac{R_{\text{vent}}}{R_{\text{atm}}} \quad (\text{A2})$$

According to *Craig et al.* [1975] $\delta^3\text{He}$ is defined as

$$\delta^3\text{He} = \left(\frac{R_{\text{meas}}}{R_{\text{atm}}} - 1 \right) \cdot 100 \quad (\text{A3})$$

and yields to equations (A4) and (A5) after insertion in (A2)

$$\frac{\delta^3\text{He}}{100} = (1 - x_{\text{vent}}) + x_{\text{vent}} \cdot \frac{R_{\text{vent}}}{R_{\text{atm}}} - 1 \quad (\text{A4})$$

$$\frac{\delta^3\text{He}}{100} = x_{\text{vent}} \cdot \left(\frac{R_{\text{vent}}}{R_{\text{atm}}} - 1 \right) \quad (\text{A5})$$

x_{vent} can be expressed as the ratio of ${}^4\text{He}$ that is introduced into the water column by hydrothermal systems (${}^4\text{He}^{\text{excess}}$) and the total measured ${}^4\text{He}$ in the sample (${}^4\text{He}^{\text{tot}}$).

$$x_{\text{vent}} = \frac{{}^4\text{He}^{\text{excess}}}{{}^4\text{He}^{\text{tot}}} \quad (\text{A6})$$

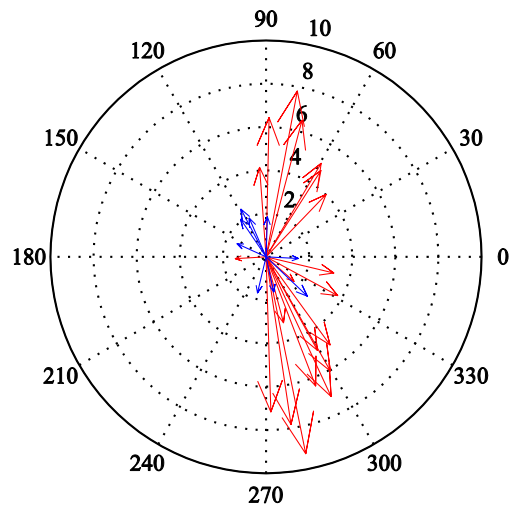
With R_{vent} as the ratio of ${}^3\text{He}^{\text{excess}}$ and ${}^4\text{He}^{\text{excess}}$

$$R_{\text{vent}} = \frac{{}^3\text{He}^{\text{excess}}}{{}^4\text{He}^{\text{excess}}} \quad (\text{A7})$$

Equation (A5) results in

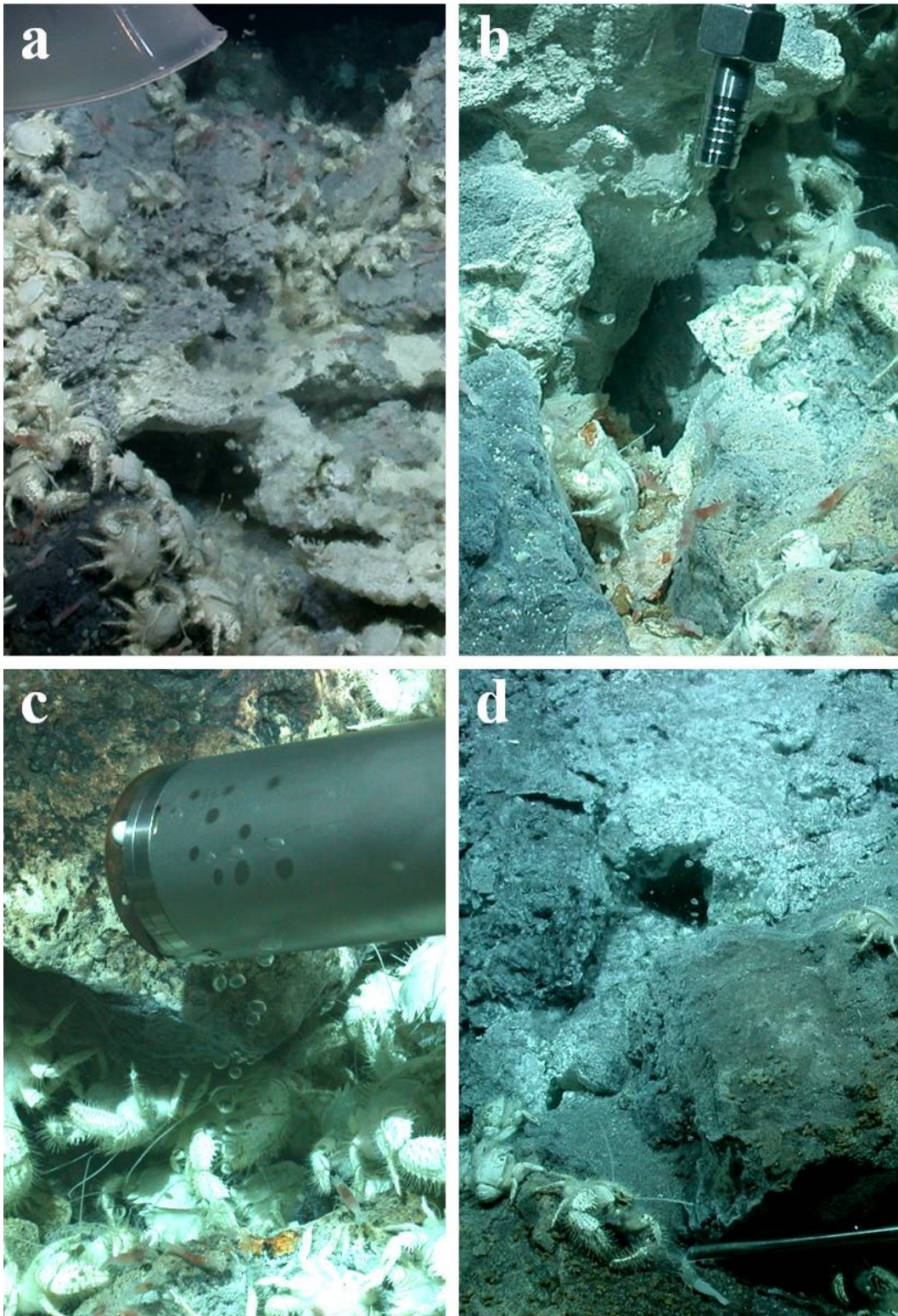
$$\frac{\delta^3\text{He}}{100} = \frac{{}^3\text{He}^{\text{excess}}}{{}^4\text{He}^{\text{tot}}} \cdot \left(\frac{1}{R_{\text{atm}}} - \frac{1}{R_{\text{vent}}} \right) \quad (\text{A8})$$

⁵⁶ These equations and caption are used in the article. Derivation was done by B. Schneider.



Appendix II: “Predicted tidal flow at HK (blue) and YK (red) during the time of observation, calculated by the TPXO7.1 model. Length of arrows in $\text{cm} \cdot \text{s}^{-1}$, direction: $90^\circ = \text{N}$ ”⁵⁷

⁵⁷ This figure and caption are used in the article. Data analysis, construction, and compilation of data in the figure was done by M. Walter.



Appendix III: Pictures from condensed phase emitting vents and immediate surrounding: (a) dive 200, GS 1, (b) dive 202, GS 4, (c) dive 202, GS 3, (d) dive 202, GS 2 copyright: MARUM University of Bremen

Appendix IV: Subsampling and measurement procedure onboard and in the laboratory

Dive-GS	Procedure onboard	Fraction	inner pressure [bar]		Measurement of		
			onboard	2014	Gas composition	Helium	$\delta^{13}\text{C}$
199-4	- subsampling of GS (no notes about procedure)	1	50	24.6	x		
	- GC measurement with syringe subsampler onboard	2					
	- subsampling of GS	3	?	28.7	x		
	- GC measurement with syringe subsampler onboard	4					
	- transfer of residual gas into GS	Rest				x	
200-1	- subsampling of GS under cooling of the subsampler	1	40	33.6	x	x	x
	- subsampling of GS	2	20	7.2	x		
	- GC measurement with syringe subsampler onboard	3+4					
200-3	- subsampling of GS under cooling of the subsampler	1	145	~140	x	x	x
	- GC measurement with syringe subsampler onboard	2	118				
	- subsampling of GS	3	105	~98	x	x	x?
	- release of gas out of the GS until 38 bar, GC measurement with syringe subsampler onboard	4	38				
202-4	- subsampling of GS	1	95	~78	x	x	x
	- subsampling of GS, GC measurement with syringe subsampler onboard, subsampler retarded	2	90				

	- p/T-expansion experiment						
	- subsampling of GS into 1 L-standard gas bottle		17				
	- subsampling of bottle	3	< 17	6.6	×		×
	- subsampling of bottle	4	< 17	5.8	×	×	
	- GC measurement with syringe subsampler onboard	5+6	< 17				
202-3	- subsampling of GS	1	65	5.4	×	×	×
	- p/T-expansion experiment						
	- subsampling of GS into 1 L-standard gas bottle		4				
	- subsampling of bottle	2	< 4	~1.7			×
	- GC measurement with syringe subsampler onboard	3	< 4				
	- subsampling of bottle	4	< 4	~1.7	×		
	- GC measurement with syringe subsampler onboard	5	< 4				
202-2	no notes, likely procedure:						
	- subsampling of GS	1	~124	~102	×	×	×
	- p/T-expansion experiment						
	- subsampling of GS into 1 L-standard gas bottle						
	- GC measurement with syringe subsampler onboard	2					
	- subsampling of bottle	3	?	4.9	×		×
	- GC measurement with syringe subsampler onboard	4					
	- storage of bottle	Rest	?	5.0	×		

Appendix V: Summary of the main components of gaseous and condensed phases at arc-related hydrothermal systems, as well as ridge systems, cold seeps at ocean margins and continental shelves, and natural hydrocarbon seepage sites.

	CO ₂	CH ₄	H ₂ S	N ₂	H ₂
Arc-related hydrothermal systems					
<u>Okinawa Trough</u>					
200-3	62.8	32.5	0.8	3.8	0.002
202-4	81.2	15.9	0.8	2.0	n.d.
202-3	88.8	8.7	1.3	1.2	0.02
202-2	43.3	50.3	n.d.	6.1	0.02
Hatoma Knoll ^a	95 - 98	present	2 - 3		
JADE ^b	86 ± 5 92 ± 1	11 (incl. H ₂) 4 (incl. H ₂)	3 4.4		11 (incl. CH ₄) 4 (incl. CH ₄)
Yonaguni Knoll IV ^c	83.6 - 86.6	12.5 - 15.4			< 0.001 - 0.01
<u>Mariana Arc</u>					
NW Rota-1 ^d	89.2 - 92.5	< 0.001		0.22 - 0.24	10.7 - 12.6
Daikoku ^d	94.0	0.004	~6 (incl. SO ₂)	0.55	0.001
Nikko ^d	96.5	0.003		1.1	8
NW Eifuku ^e	98.6 - 99.6*	< 0.001	0.5 - 0.8	0.1 - 0.2	< 0.001
<u>Tonga-Kermadec Arc</u>					
Giggenbach ^d	77.5 - 88.9**	0.007 - 0.01		4.8 - 12.9	0.02 - 0.03
Volcano-1 ^d	97.7 - 102	0.005 - 0.05		0.7 - 1.9	< 0.001 - 0.03

Ridge systems, cold seeps, and hydrocarbon seepage sites

Mid-Atlantic Ridge

Jan Mayen ^f	76.9	7.1	12.2***	0.3
------------------------	------	-----	---------	-----

Ocean margins and continental shelves

Svalbard ^g	< LOD - 1	98.98 - 99.99		
-----------------------	-----------	---------------	--	--

Makran continental margin ^h		99.94 - 99.98		
--	--	---------------	--	--

Santa Barbara Channel

Coal Oil Point ^{i,j}	3.1 - 25.5	64.0 - 89.7	1.2 - 5.1	
-------------------------------	------------	-------------	-----------	--

^a *Shitashima et al.* [2008], ^b *Sakai et al.* [1990a], ^c *Konno et al.* [2006], ^d *Lupton et al.* [2008], ^e *Lupton et al.* [2006], ^f *Pedersen and Baumberger* [2011]; <https://doi.pangaea.de/10.1594/PANGAEA.788169>, ^g *Sahling et al.* [2014], ^h *Römer et al.* [2012], ⁱ *Clark et al.* [2003], ^j *Clark et al.* [2010]

* elevated N₂ concentration was attributed to air contamination during sample handling, hence the CO₂ content was recalculated to 98 - 100 % on the basis of N₂ and Ar concentration

** elevated N₂ concentration was attributed to air contamination during sample handling, hence the CO₂ content was recalculated to 94 - 98 % on the basis of N₂ and Ar concentration

*** elevated N₂ concentration very likely due to air contamination during sample handling and measurement (O₂ concentration: 2.1 %)

Danksagung

Von der ersten Probenahme auf der FS Sonne bis zur letzten Kommasetzung im Manuskript hat sich in meinem Leben viel verändert. Dabei konnte ich mich in jeder Phase meiner Promotion stets auf die Unterstützung meiner Familie, Freunde, Betreuer, Vorgesetzten, Kollegen, Co-Autoren und vieler mehr in meinem näheren Umfeld verlassen, dass mir nur zu sagen bleibt:

DANKE

Wissenschaftlicher Lebenslauf

Beruflicher Werdegang

- seit März 2021 Teamleiterin Organik bei Kiwa GmbH
- Januar 2017 - Februar 2021 Chemikerin bei Eurofins Dr. Specht Laboratorien GmbH
- Februar - September 2016 Verwaltungsmitarbeiterin in der DRK Rostock gGmbH für Menschen in Not
- Januar - April 2016 Wissenschaftliche Hilfskraft am Leibniz-Institut für Ostseeforschung Warnemünde (IOW)
- September 2015 - Januar 2016 Betreuerin für Flüchtlinge beim DRK KV Rostock
- April - Oktober 2015 Chemielaborantin bei der NORDTEST Prüfgesellschaft mbH
- November 2011 - Dezember 2014 Wissenschaftliche Angestellte am IOW
- Dezember 2007 - November 2011 Studentische und wissenschaftliche Hilfskraft am IOW
- September 2007 Praktikum bei Dr. Krenzel GmbH Institut für Umweltschutz und Qualitätssicherung (IUQ)

Ausbildung

- seit November 2011 Promotionsstudium an der Universität Rostock und dem IOW
- Oktober 2005 - Juli 2011 Studium der Chemie an der Universität Rostock
- bis Juni 2005 Schulbildung

Mitgliedschaften

- seit März 2013 Mitglied in der Graduiertenakademie der Universität Rostock